Geo-modelling of an exhumed reservoir cap rock succession, Utah, USA

Master Thesis

Anette Harneshaug

Department of Earth Science

University of Bergen

June 2017

ABSTRACT

Carbon capture and storage (CCS) can potentially play an important role in mitigating global CO_2 emissions. The storage sites must be understood in detail to ensure safe storage on a millennial time scale. Outcrop analogues have been studied in order to enhance the understanding of the subsurface in regards of reservoir properties, sand body connectivity and vertical developments. An exhumed paleo-reservoir in Utah, Humbug Flats, is of special interest as it shows evidence for CO_2 accumulation and leakage through bleaching of the outcrop. This paleo-reservoir can therefore be used as an analogue to potential locations for CO_2 storage.

The main objective of this thesis is to compile and systemize data from previous studies in the area of the outcrop collected by the COPASS project. Issues related to acquisition and merging of multi-source collected outcrop data are identified and described. Facies associations have been mapped in 3D by the use of Lidar images and sedimentary logs. A modelling workflow is developed for RMS^{TM} (reservoir modelling program), implementing available data into one coherent geo-model. Problems related to merging of multi-source datasets, input data quality and model implementation are identified and addressed. The model set-up provided is considered robust for further work in the project.

ACKNOWLEDGEMENTS

Table of Contents

1. INTRODUCTION

1.1 Motivation

Carbon capture and storage (CCS) can potentially play an important role in mitigating the global CO_2 emissions. CCS involves capturing CO_2 from fossil fuel combustion for long-term sequestration, mainly in subsurface reservoirs. In order to ensure the safety of these storage sites, a detailed understanding of the reservoir and containing seal is required. Migration pathways should be considered and an impermeable layer must contain the CO_2 in the subsurface and hinder the CO_2 from leaking. The storage site should fulfil a given set of criteria regarding capacity, injectivity and containment of the CO_2 (Bachu, 2008; Raza et al.,2016). Long term storage safety and cost efficiency also needs to be considered. The geological formations that largely meet these requirements are mainly deep saline aquifers and depleted oil and gas reservoirs. These reservoirs have been extensively studied as part of oil and gas exploration and production. Experiences and characterizing methods developed by the hydrocarbon industry are easily transferrable to CO_2 storage.

There are, however, several issues specific to CO_2 storage, which should be kept in mind. Storage operates on a millennial time scale, so processes insignificant or rare on an exploration and production time scale, such as repeated seal breaches by major faulting, or chemical interaction between pore fluids and the reservoir, may turn out to be important. Another issue is spatial scale: CCS on industrial scale requires huge volumes to be stored and correspondingly large (and spatially extensive) reservoir volumes to receive this. Both issues increase the likelihood for seal breaches.

Outcrop analogues may enhance the understanding of the subsurface and provide an understanding of the sand body connectivity, vertical developments and reservoir properties measurements. This is especially useful when working with spatially limited or low-resolution subsurface data sets (Howell, Martinius, Good, 2014; Rotevatn, Buckley, Howell, & Fossen, 2009). Reservoir and simulation models are important decision-making tool as they provide an understanding of the geological, geophysical and engineering components (Caers, 2005). Modelling makes it possible to identify and quantify CO_2 migration, multiphase flow and

1. Introduction

potential leakage (Behzadi, Alvarado, & Lynds, 2012). Modelling of analogues thus can improve our understanding of subsurface reservoirs and seals.

This thesis is a part of the project "CO_2 seal bypass" (COPASS), funded by the Norwegian Research Council and led by the Department of Geoscience at the University of Oslo in collaboration with Uni Research, NGI, Utah State University, Colorado School of Mines and Western State Colorado University. The aim of the project is to study an exhumed paleo-reservoir that shows evidence of CO_2 accumulation and flow in order to increase our understanding of seal integrity and leakage processes. Outcrops in Utah are of special interest as there is ample evidence of ongoing and former CO_2 accumulation and leakage from the subsurface. Eolian deposits in the selected field area are coloured red by iron oxide, but bleaching is observed in the outcrop along faults, fracture corridors and some stratigraphic intervals. The discoloration is a result of circulating CO_2 and/or hydrocarbon-charged fluids dissolving and removing the iron-oxide. The bleached areas roughly outline ancient hydrocarbon/CO_2 reservoirs (Ogata, Senger, Braathen & Tveranger, 2014). The paleo-reservoir can be used as an analogue to potential CO_2 sites today.

One of the aims of the COPASS project is to generate a high-resolution geo- and simulation model based on field observations, digenesis and geomechanical properties and conduct systematic sensitivity studies on selected parameters and upscaling. This will serve to identify flow paths and analyse reservoir response to CO_2 pressure and migration. Ultimately this provides insight into how CO_2 flows along sediment layers and faults, and which geological features and properties play a role in where and how CO_2 can breach cap rocks and seals. The project consists of five work packages with sub-objectives (Figure 1.1.1). Each of the work packages targets critical features to better assess leakage prevention and mitigation. These include:

- WP 1. Rock properties: Sedimentary and structural properties, and petrophysical properties of the reservoir-caprock system.
- W*P 2.* Diagenetic effects*:* Comparison and analyse of pristine vs. CO_2 exposed mudstone and sandstone.
- WP 3. Geomechanics: Analyse critical loads on reservoir model scale. Collect shear and tensile strength of caprock and fault rocks.
- WP 4. Reservoir modelling and simulation: High-resolution geo- and simulation models based on the above information.

1. Introduction

- WP 5. Education and outreach: Presentation of results.

WP 1   WP 2   WP 3   WP 4   WP 5

| Rock Properties | Diagenetic effects | Geomechanics | Reservoir modelling and simulation | Education and outreach |
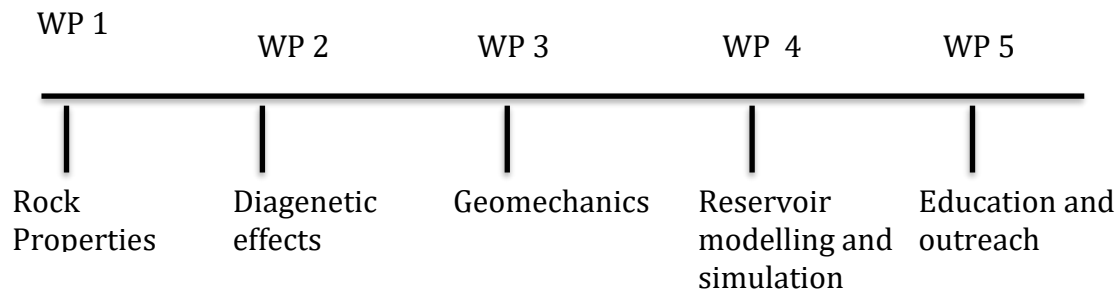
Figure 1.1.1: Five working packages related to the COPASS project.

1.2 Objectives

The purpose of this thesis is twofold. One objective is to compile and systemize data collected by the COPASS project in the study area as of May 2017. The second objective is to implement these data into a coherent geo-model and identify any problems related to the input data and model implementation.

The COPASS project will continue until the end of 2018. This implies that the compilation and processing of project datasets is still work-in-progress. The model presented here has been populated with the data available at the time of submission and should therefore not be considered a finalized product. What is emphasized here is identification and description of problems and issues related to acquisition and merging of multi-source collected outcrop data and their subsequent model implementation.

The database used in the present thesis has been compiled from a series of Master thesis attached to the COPASS project (Larsen, 2015; Hope, 2015; Rimkus, 2016; Gurrik, 2016; Sleveland, 2016 and Kristensen, in prep.), and supplemented by other published or publically available data from the study area.

1.3 Outline

The outline for this thesis is as follow:

Chapter 1 presents the motivation and objectives for this thesis

Chapter 2 presents the regional geology

Chapter 3 presents the methods used in this thesis

Chapter 4 presents the database and problems related to merging datasets

Chapter 5 gives an understanding of the virtual outcrop interpretation

Chapter 6 presents the modelling workflow compiled in this thesis

Chapter 7 discussion of the merging of datasets, modelling challenges and quality assessment of the different stages in the modelling workflow

Chapter 8 conclusion and discussion of future work

1. Introduction

1.4 Study area

The study area is located in central Utah, USA. The study area is located North-East of San Rafael Swell and covers the Humbug Flats, Stove Gulch and partly the Sulphur Canyon (Figure 1.4.1). The upper Entrada Formation, Curtis Formation is exposed and limited exposure of Summerville Formation.

A major E-W trending normal fault intersects the study area. The middle-upper part of the Curtis Formation is juxtaposition against the upper part of the Entrada sandstone (Ogata et al., 2014). In the hanging wall a larger part of Curtis Formation is present. The channel in Stove Gulch makes it possible to investigate the lower Curtis Formation and J-3 unconformity.
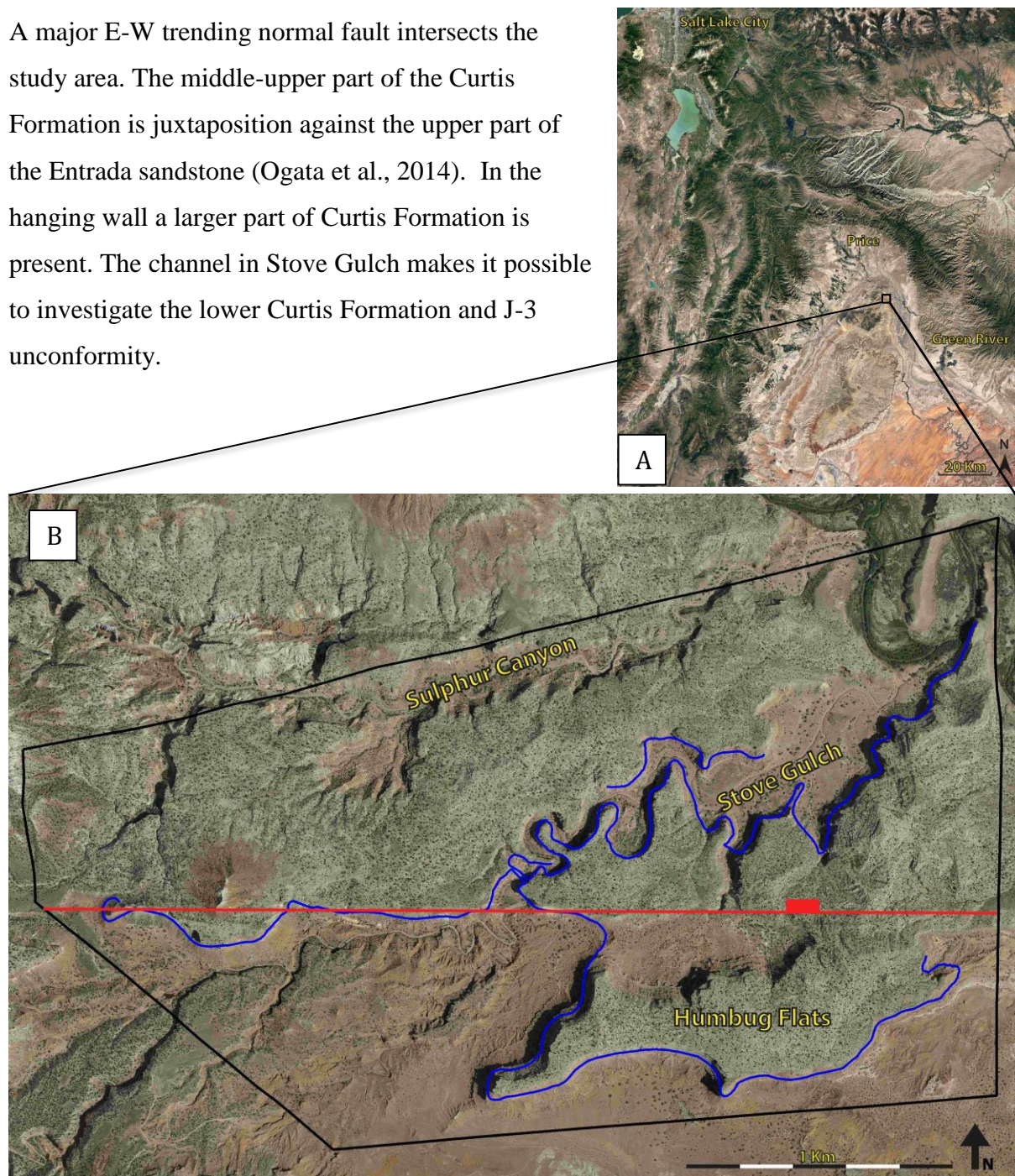
Figure 1.4.1: Location of the study area Fault intersecting the study area. The blue lines represent the Lidar coverage.

2. REGIONAL GEOLOGY

Reconstruction of depositional and erosional patterns is dependent on an understanding of past tectonic and climatic conditions (Hintze & Kowallis, 2009). A brief description of the sedimentary succession, tectonics and climate of Utah during the Mesozoic is supplied below. It provides the stratigraphic context and depositional setting of the Jurassic Entrada sandstone, Curtis and Summerville Formations, which are the focus of this study.

2.1 Mesozoic Tectonic setting

During the Mesozoic era a variety of events, including salt tectonics, the development of a mountain chain along the western side of America, the uplift of the Colorado Plateau and igneous intrusions have all left their mark on the stratigraphy of the area (Ogata et al., 2014). During Triassic the supercontinent Pangaea broke up and rifting between Laurasia and Gondwana commenced, leading to the formation of the Atlantic Ocean. The North American plate moved north-west and in the late Triassic North America separated from South America (Hintze & Kowallis, 2009). The North American plate moved over Farallon oceanic plate and developed a steeply dipping subduction zone that bordered the western margin of the North America (Hintze & Kowallis, 2009; Peterson, 1994). Tectonic activity along the western margin caused the interior of the plate to subside forming a depocenter for sediments deriving from the bordering highlands; the Entrada sandstone was deposited during this phase (Hintze & Kowallis, 2009).

The Cordilleran thrust belt and foreland system developed during Middle to Late Jurassic time (Peterson, 1994; DeCelles, 2004). The orogeny was driven by subduction of the Farallon plate beneath the North American continental plate (DeCelles, 2004) and collision of island arc system and micro continents (Peterson, 1994). Compressional forces lead to the development of the Nevadan, Laramide Rocky Mountains and Sevier mountain chains (DeCelles, 2004; Ogata et al., 2014). The Nevadan orogeny lasted through Late Jurassic and Early Cretaceous. North America grew as a response to the accretion of island arcs and several granitic intrusions are found along the border of Utah (Hintze & Kowallis, 2009).

2. Regional Geology

The Elko orogeny, stretching from central Utah to central Nevada, formed in the Middle Jurassic. The orogeny includes both extensional and contraction structures. Based on westward thickening of low gradient sedimentary successions of Middle Jurassic age, Thorman and Peterson (2003) proposed that the orogeny caused the creation of a foreland basin in central Utah.

The Sevier and Laramide orogenies partially overlap in space and time, but are considered two different events due to their different tectonic expressions. Compressional forces of the Sevier orogeny were transferred eastward along weak planes in the sedimentary succession. The Laramide orogeny, on the other hand, exhibits deeper deformation along pre-existing basement faults. In Utah during the Cretaceous, the Sevier orogeny (Jurassic to Eocene (Taylor et al., 2000)) formed an alpine upland consisting of folded and faulted deposits in the west (Hintze & Kowallis, 2009) and a subsiding foreland in the east (Peterson, 1994).

The Laramide orogeny started to form in late Cretaceous, and is believed to be a response to a change in subduction geometry from steep to flat subduction of the Farallon plate (Liu & Currie, 2016). Compressional forces generated from the collision of the North American plate with the Pacific plate lead to the development of the San Rafael Swell; a dome-shaped anticline (Ogata et al., 2014) .

2.2 Paleolatitude and paleoclimate

Paleomagnetic records reveal the variations in latitudes of Utah during geological time. From Cambrian time Utah was located 30° south and towards today 40° north passing different climatic zones. Figure 2.2.1 shows how the Colorado plateau drifted during Mesozoic from close to equator to 45° north (Hintze & Kowallis, 2009). The latitudes are consistent with the intertropical zone and trade wind belts. A warm, arid climate and southward wind transport is characteristic of this Era. Deposits are also affected by periods of fluctuations in global sea level which caused several unconformities to form (Peterson, 1994).

2. Regional Geology
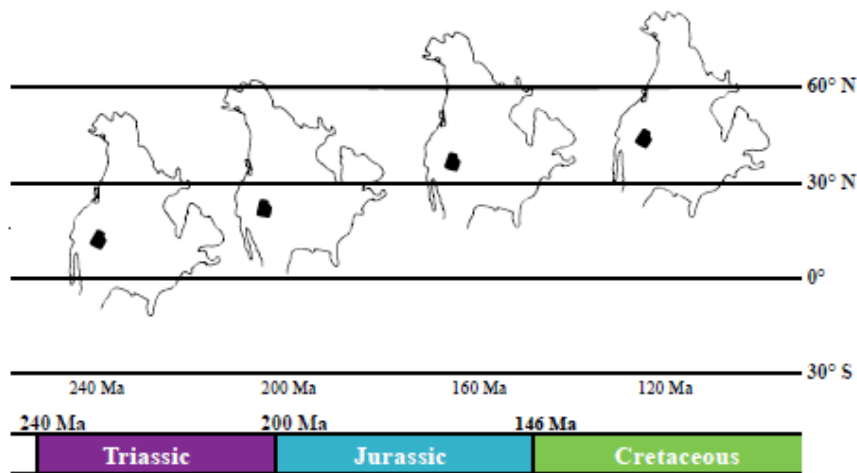
Figure 2.2.1: Reconstruction of paleogeography of Utah during the Mesozoic Era (modified from Sleveland (2016) after Hintze & Kowallis (2009)).

During the Early Mesozoic, the Colorado Plateau was located in the subtropical climate belt. This is confirmed by low paleomagnetic inclinations (Loope, Steiner, Rowe, & Lancaster, 2004). Paleowind studies from the Early Permian to Early Jurassic Navajo Sandstone (Loope et al., 2004) suggest prevalent tropical north – westerlies in the region. In the Early Jurassic, Utah was located approximately 10° north of the equator. The Colorado Plateau experienced a more rapid northward migration in the Middle Jurassic (Loope et al., 2004).

At the time of deposition of the Entrada sandstone, the area was situated between 15°N and 25°N; in a mainly arid and warm zone within the north-easterly trade wind belt. Seasonal typhoons may have formed storm-related beds (Kocurek, 1981; Peterson, 1994). Evidence of the general warm and arid climate is found with the presence of evaporites in the Carmel Formation and red bed deposits in the Entrada sandstone (Kocurek, 1981). Atmospheric circulation patterns also determine the deposition of eolian sand (Peterson, 1994).

2. Regional Geology

2.3 Geological history and stratigraphy of the Jurassic

In this chapter the focus is on the Middle Jurassic, Entrada sandstone and Curtis Formations as well as the J-3 unconformity between the formations. A structural description of the outcrop will also be explained with focus on bleaching.

Based on interpreted depositional environments, the Jurassic stratigraphy can be distinctly divided into a lower, middle and upper succession. The lower Jurassic succession consists of eolian deposits, the middle is characterized by marine incursions as a result of a seaway from Canada, whereas the upper part reflects a reversion to eolian depositions (Hintze & Kowallis, 2009).

2.3.1 Glen Canyon Group (Lower Jurassic)

Early Jurassic sandstone consists of the Wingate sandstone at the base, the Kayenta Formation in the middle and the Navajo sandstone at the top, which make up the Glen Canyon Group (Figure 2.3.1) (Peterson, 1994; Hintze & Kowallis, 2009). During lower Jurassic, Utah was located approximately 10° north of the equator and was moving northwards. The climate during this period was warm and arid (Loope et al., 2004). The Wingate Sandstone is of eolian origin and is characterized by its vertical cliffs and large-scale cross stratificated dunes (Loope et al., 2004). The Kayenta Formation reflects a fluvial environment and consists of conglomerate, sandstone and siltstone (Peterson, 1994). The Navajo sandstone exhibits large scale eolian cross-bedded sandstone, reflecting predominantly northwest winds (Hintze & Kowallis, 2009; Loope et al., 2004). The mineralogy of the Wingate and Navajo Sandstone indicate an original sediment source in the Appalachian Mountains (Loope et al., 2004). The sediments have been transported by marine currents and streams before being redeposited by eolian processes on what is now the Colorado Plateau (Dickinson & Gehrels, 2003). A regional erosional unconformity, J-1, separated the Navajo Sandstone from the overlying Page Sandstone (Figure 2.3.1) (Peterson, 1994).

2. Regional Geology
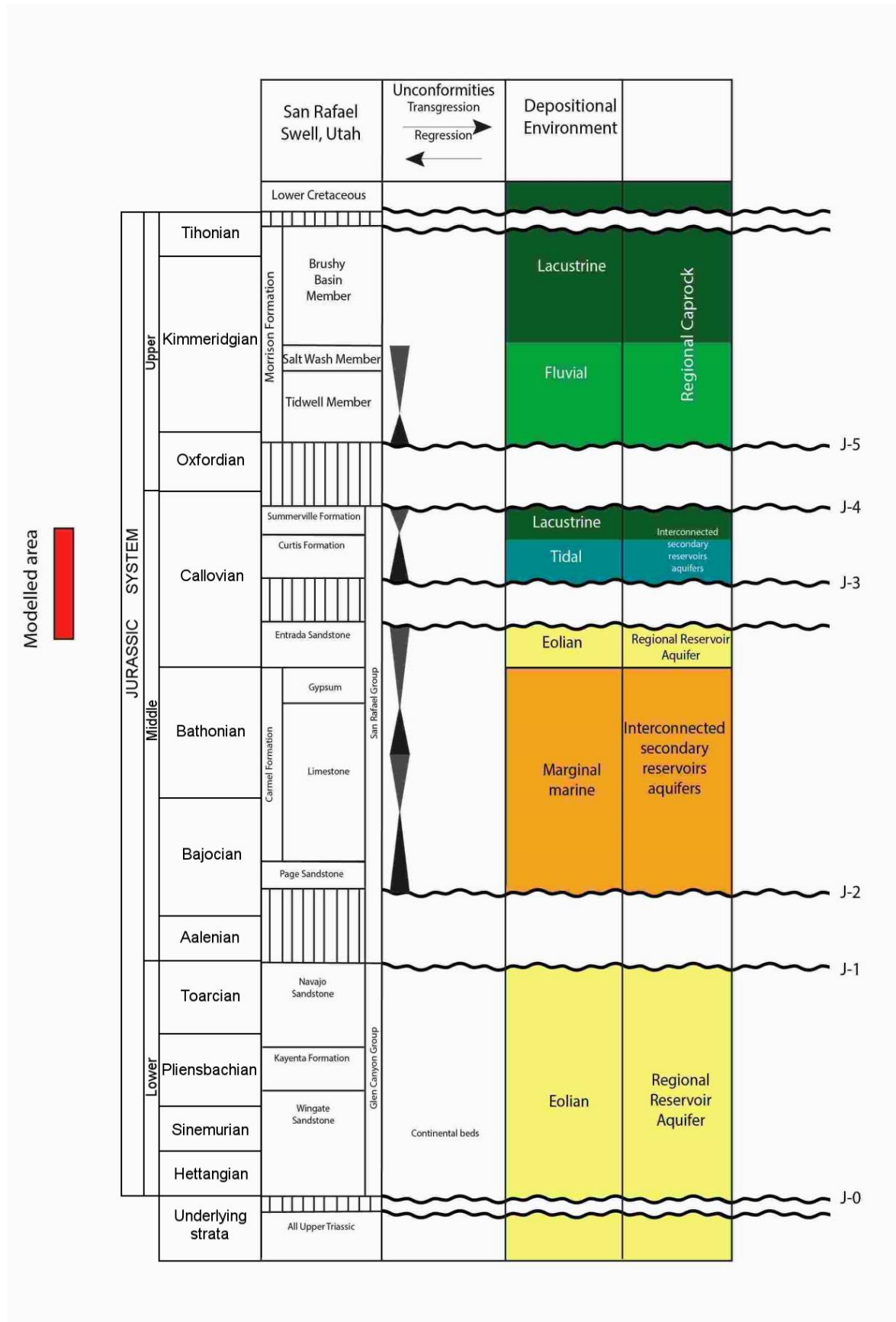
Figure 2.3.1: Jurassic stratigraphic units. On the right, transgressive-regressive cycles and unconformities are displayed. Depositional environments are displayed to the right (Modified from Peterson, (1994); Chan, Parry & Bowman, (2000) and Ogata et al., (2014)).

2. Regional Geology

2.3.2 San Rafael Group (Middle Jurassic)

Five marine transgressive – regressive cycles during the Middle Jurassic moved the shoreline in the northern part of the region back and forth. Figure 2.3.1 summarises the transgressive – regressive sequence and their associated erosional unconformities (Peterson, 1994). The Middle Jurassic succession comprises the non-marine Page sandstone, the marine Carmel Formation, the aeolian erg and wet dune field Entrada sandstone, the marginal marine Curtis Formation and the Summerville Formation deposited on a coastal plain (Hintze & Kowallis, 2009). The early phase of the Elko orogeny caused a rapid subsidence of the area by thrust loading (Peterson, 1994).

Page sandstone

The Page sandstone is the lowermost unit in the San Rafael Group and deposition was controlled by climate, tectonic events and fluctuations in sea level (Blakey, 2008). The formation consists of eolian sandstone with channel- and lens-shaped deposits. Jones and Blakey (1997) suggested that ephemeral stream processes have formed the scours and in-fill deposits.

Carmel Formation

The Carmel Formation was deposited during a marine transgression extending southwards from Canada (Hintze & Kowallis, 2009). It reflects marine and sabkha environments, with periodic flooding depositing sand, silts, and evaporites, such as gypsum, reflecting periodic constrained circulation and evaporation.

Entrada sandstone

The upper Jurassic (80 to 140 Ma) Entrada sandstone is characterized by eolian, sabkha and tidal flat deposits (Kocurek, 1981). The transition from the underlying Carmel Formation is gradational and conformable (Blakey, 2008). The formation covers the entire Colorado Plateau and can be found everywhere except where it has been eroded in the Cenozoic. The depositional system, subsidence rates and the height of the water table controls the stratigraphy and regional facies pattern of the Entrada sandstone (Peterson, 1994). The thickness of the Entrada sandstone is difficult to determine due to the upper part of the sandstone is commonly eroded. The sequence thickens westward due to subsidence of the Utah-Idaho Trough (Blakey, 2008).

2. Regional Geology

The Entrada sandstone consists of eolian sandstone and sabkha deposits such as sandstone and silty sandstone (Figure 2.3.2) (Peterson, 1994). The sandstone has a dark reddish colour mainly due to hematite coating of sand grains. Fine to medium sandstone was deposited as wet eolian dune fields and interdune deposits (Ogata et al, 2014). Kocurek (1981) described four facies in the Entrada sandstone: central erg, interdune deposits, coastal erge and inland-margin erg. Distribution, structure and types of interdune areas, dunes and other sub environments within eolian sand seas are controlled by climate, geographic location, availability and source of ground water table, grain size variations of sand, vegetation as well as topographic character (Kocurek, 1981). Bleached sandstone intervals can be observed in some parts of the lower-middle Entrada sandstone which are believed to represent an ancient reservoir and migration pathways for reducing fluids such as hydrocarbons (Ogata et al., 2014).
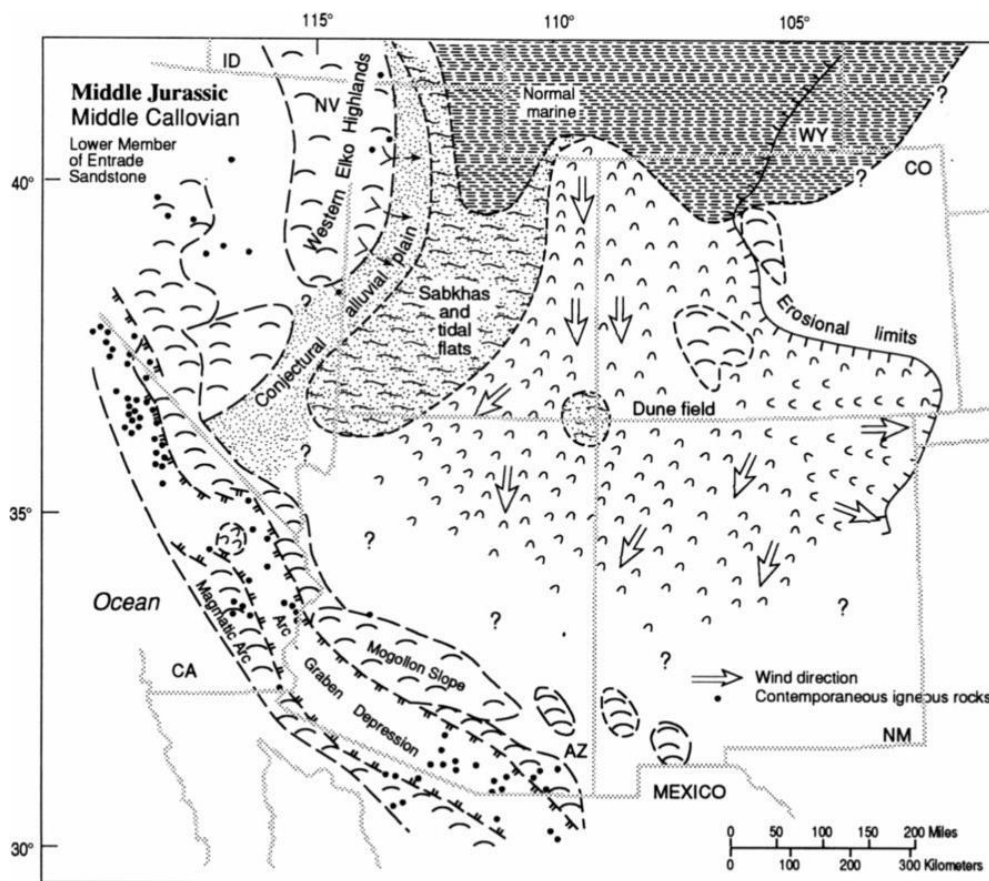
Figure 2.3.2: Paleogeography of the Western Interior basin during late Middle Jurassic (Peterson, 1994). The landscape is dominated by eolian sands of the Entrada sandstone.

2. Regional Geology

The Entrada sandstone in the Green River Basin is subdivided into three members (from older to younger): the Dewey Bridge Member, the Slick Rock Member and the Moab Tongue Member (Chan et al., 2000; Wright, Shawe, & Lohman, 1962).The different depositional facies of these units affect fluid flow in different ways.

The Dewey Bridge Member consists of reddish brown silty sandstone and mudstone, which have been deposited in a mixed sabkha/eolian environment. The lower stratigraphic sections have bed-scale breccia in the study area and therefore indicate deposition in sabkha environments. The upper part consists of dissolved evaporites which are replaced by chert pieces. Low permeability silt is dominant in the Dewey Bridge Member and fluid circulation can only circulate through sandier units (Chan et al., 2000).

The Slick Rock Member is typically red, silty sandstone interpreted as having been deposited under one or several brief marine transgressive – regressive cycles (Peterson, 1994). The Slick Rock Member is characteristic for a wet-eolian dune system (Chan et al., 2000). Soft sediment deposits have been observed within the sabkha deposits (Chan et al., 2000).

The Moab Tongue Member is the uppermost part of the Entrada sandstone. The member is mainly white and has bleaching as well as it is jointed (Chan et al., 2000). The member represents transitional beach to eolian dune deposits (Kocurek, 1981). The deposits are fine grained and cross-stratified eolian dune sets and horizontal stratification is present. Jointing has likely enhanced the permeability of the unit (Chan et al., 2000).

J-3 unconformity
The J-3 unconformity truncates the top of the Entrada sandstone and it is overlain by the Curtis Formation and reflects a regional transgression. The unconformity is largely a disconformity although it locally can be an angular conformity (Hicks, Morris, & Fairbanks, 2010). Peterson (1994) suggested that the unconformity could be a result of tectonic processes as it is difficult to correlate to global eustatic curves. The transition from the sandstone rich Entrada Formation to the mudstone dominated marine-influenced facies of the Curtis Formation across the J-3 unconformity presents a potential for stratigraphic and combination traps for hydrocarbon accumulation (Hicks et al., 2010).

2. Regional Geology

Curtis Formation

The Curtis Formation can be considered a regional cap rock (Ogata et al., 2014). The formation consists mainly of greenish-grey, pebbly sandstone and mudstone, and is interpreted as having been deposited in a marine and marginal marine tidal flat environment formed during a cycle of marine transgression and regression (Figure 2.3.3) (Peterson, 1994). At the base of the formation some conglomerate horizons are present in erosional depressions; likely representing a transgressive lag (O'Sullivan, 1981). The lower part of the Curtis Formation is characterized by fine-grained sandstone and a coarsening upward trend. The uppermost part of the formation represents a flooding event. The deposits show nearshore sedimentary structures such as low angled cross-stratified sand that reflects beach deposits and sigmoidal and tidal bundles that represents tidal deposits. The lower Curtis deposits are derived from a transgressive system in fine-grained facies. The middle and upper Curtis deposits are deposited under a high stand system from marine shelf to tidal channels to shore face environments. The upper sequence is a tidal flat with mudstone and evaporates (Blakey, 2008).
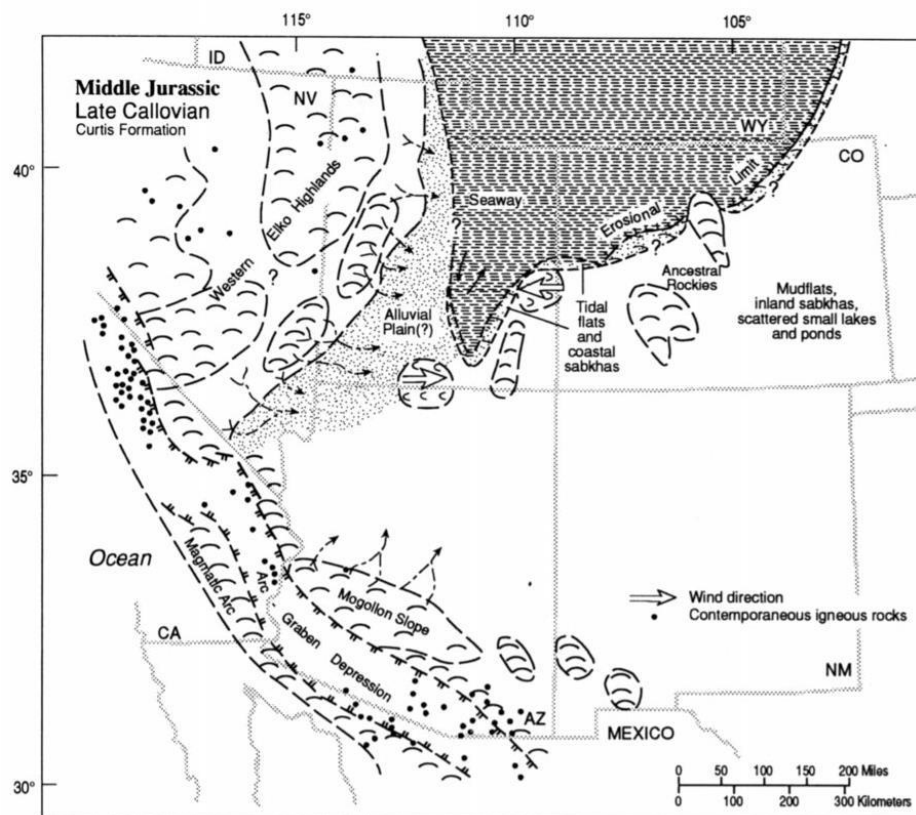
Figure 2.3.3: Paleogeography of the Western Interior during late Middle Jurassic (Peterson, 1994).

2. Regional Geology

Summerville Formation

The Summerville Formation consists of thin-bedded red siltstone and mudstone with thin limestone layers (Blakey, 2008), and is interpreted as having been deposited under coastal sabkha conditions. The presence of hypersaline shallow-marine waters caused precipitation of gypsum and anhydrite (Wilcox, 2007; Peterson, 1994). Wilcox (2007) and Peterson (1994) describe a regressive unconformity (J-5) truncation above the Summerville Formation. The Summerville Formation is thus overlain by the Upper Jurassic Morrison Formation.

2.3.3 Morrison Formation (Upper Jurassic)

The Upper Jurassic (155-148Ma) Morrison Formation consists of continental deposits including fluvial channel, floodplain and lacustrine deposits as well as paleosols. It is subdivided into three members: Tidwell, Salt Wash and Brushy Basin Member (Peterson, 1994). The Morrison Formation can be traced regionally from northern Mexico to southern Canada, and is famous for its well preserved dinosaur fauna (Hintze & Kowallis, 2009).

2.4 Structural description of the outcrop

Fluid flow in the subsurface is strongly influenced by the presence of faults and fractures, which can affect reservoir connectivity and seal integrity both positively and negatively. Mapping and modelling the structural features of a reservoir is therefore important.

An E-W trending normal fault intersects the study area and separates the upper Entrada sandstone against lower Curtis Formation (Figure 1.4.1). Gurrik (2016) estimated the displacement to be 37-42 m. A previous study by Ogata et al., (2014) has identified a parallel normal fault south of the study area with an opposite dip. This suggests that an E-W trending horst with several small and moderate displacements as a response to normal faults (Ogata et al., 2014).

The fracture networks display a bleaching that is concentrated within and around the fractures and are interpreted as evidence of reducing fluid circulation. Bleaching is a result of the removal of hematite by reducing fluids. The fractures may act as a barrier or a conduit to fluid flow. One therefore needs to understand how the fractures influence fluid flow. The

forming process and mechanical properties as well as the lithology determine the lateral extension and the width of the fractures (Ogata et al., 2014).

Apart from the fault, no structural details are included in the present model, as the data are still in process of being worked up by the project group.

3. METHOD

3.1 Lidar

Lidar (light detection and ranging) is a surveying technique that measures the distance between a topographic surface and the instrument. Lidar instruments are active scanners; it emits a signal in form of a laser pulse, which, deflects at the topographic surface and return to the measuring sensor (Bellian, Kerans, & Jannette, 2005). The distance is measured by calculating the time difference between the emitted signal and the reflected light (Buckley, Howell, Enge & Kurz, 2008). The travel time of the laser pulse is divided in half and multiplied by the speed of light to obtain a distance (Bellian et al., 2005). The instrument registers horizontal and vertical angular components by use of a monitored sensor head or a system of rotating mirrors. 3D coordinates (x,y,z) are obtained by combining angular measurements with the range measurements. The acquisition of point data represents a terrain surface (Buckley et al., 2008). Lidar systems often have a built-in or separately mounted digital camera, which is used to "obtain true-color information" or photo texturing of the model (Billian et al, 2005; Buckley et al, 2008). The camera has a high-accuracy registration and can be used directly with the data (Buckley et al., 2008).
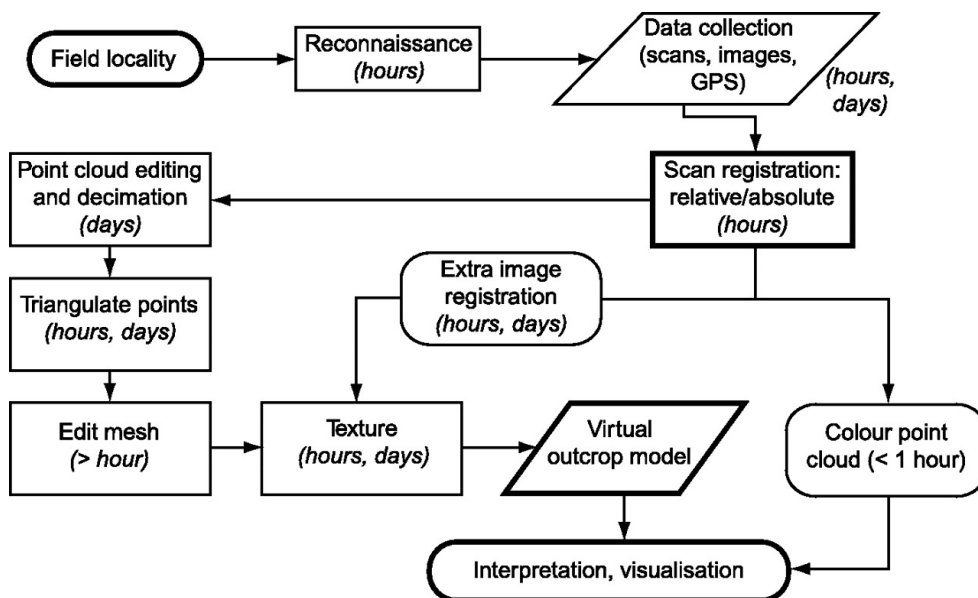
Figure 3.1.1: Workflow from field acquisition to creation of a virtual model for interpretation. The different field and processing tasks indicate timing (Buckley et al, 2008)

3. Method

Figure 3.1.1 displays the workflow from field acquisition to the virtual model (Buckley et al, 2008). During data collection large amounts of x,y,z- data positions are collected, and a point cloud is created. The points are connected by triangulation, which involves finding the best-fit surface through the points to obtain a high-resolution surface (Buckley, 2008). As the point cloud involves a large amount of points, it needs to be reduced with little loss of accuracy. Areas of low surface roughness are edited by larger triangles, and areas with more details are represented by smaller triangles. Texturing of the model involves filling the gaps between the points by images. The most suitable image is chosen based on direction of the camera and orientation of the triangle. This process leads to a higher resolution and a continuity of data (Buckley, 2008).

Conditions at the time of collection and during processing stages may influence the model accuracy (Buckley, 2008). Outcrop limitations are related to erosion/weathering, degradation, accessibility and limited spatial exposure, as well as atmospheric conditions. CPU limitation and memory availability lead to a need to reduce the raw point cloud. There are many advantages related to Lidar scanning. It is possible to map geological features with high precision, as well as vertical cliffs where it would be unsafe and difficult to conduct fieldwork (Buckley, 2008). Texturing of the outcrop determines the resolution and visual effect that depends on the lightning conditions (Buckley et al., 2008).

In this project a ground based Riegel VZ-1000 Lidar scanner was used with a point precision of 5 mm. The scanner is mounted on a tripod and held fixed under measurements (Buckley, 2008). The laser scanner has a built-in global Navigation Satellite System. A digital camera with a 4.9 μm pixel size is mounted on top of the scanner for later texturing of the outcrop. Benjamin Dolva performed the processing of the data.

3. Method

3.2 Software

3.2.1 Lime
Lime (Lidar Interpretation and Manipulation Environment) is a virtual model interpretation and visualization software. It is developed by Virtual Outcrop Geology Group (VOG), which is collaboration between the University of Aberdeen and the University of Bergen. The program contains interpretation tools to digitize and measure geological features through line interpretation. These lines are generated by clicks, where each click results in a point, forming a 3D point cloud, which was later exported from Lime and imported into RMS. Lime thereby provides a tool for mapping and representation of outcrops in 3D, making it possible to trace facies associations and faults in the outcrop.

In this thesis, the knowledge provided by interpretation of the sedimentary logs and prior information about the geology in the study area was combined with Lime to successfully trace facies associations along the outcrop.

3.2.2 RMS
The modelling software used in this thesis is RMS^{TM} 2013.1.2, developed by Roxar Software Solutions. The program is used for linking datasets of geology, petrophysics and reservoir engineering datasets. The aim of the reservoir modelling is to forecast reservoir properties, calculate volume and predict the dynamic behavior of the reservoir over time.

The available data, as well as Lime interpretation, was imported into RMS. This results in a high-resolution geo model. The full workflow for the modelling is given in Chapter 6.

The modelling process was optimized by creating an automated job and task sequence. This enables the parameters from the job list to be modified and manipulated without having to run each of them manually. When performing stochastically modelling, a loop can be placed within the workflow and multiple realizations can be produced. Nested workflow is an operation that allows a workflow to be integrated into a larger workflow as a separate job. This is used for the horizon modelling and fault modelling to have a better overview of the modelling process.

3. Method

3.3 Fieldwork

3.3.1 Permeability measurements

A portable handheld permeameter, TinyPerm 2, is used to measure permeability of the rock matrix in-situ. The measurements were taken from a surface that was not fractured, and the outer-most weathered surface was removed using a geological hammer and chisel. The permeameters tip is pressed firmly against the rock and air is pressed though. The permeameter measures the response function of the system to reach equilibrium (Filomena, Hornung, & Stollhofen, 2014). The response function (T) is shown on the display of the tool. Permeability is then calculated through a set relationship between the permeability (k) and (T) (equation 1)

[Equation 1]

$$T = -0.8206 \log_{10} k + 12.8737$$

Where k is given in millidarcy (mD).

To ensure permeability measurements of high quality, three or more measurements are sampled at each spot. The mean value at each spot is used in calculating the permeability of each bed. Both horizontal (kh) and vertical (kv) permeability measurements are collected.

A 5 minute limit for each measurement was used, and measurements over this limit are considered low permeable. The 5 minute limit is equivalent to the lower measuring threshold 10mD, according to the manufacturer (Filomena et al., 2014).

3.3.2 GPS tracing fault

GPS coordinates for the position of the fault trace were recorded while hiking. The fault trace was recognised in the field where it was exposed, and based on Google Earth images where the area was covered by scree. The area East of the meandering nature of Stove Gulch eroded the topography was too steep to hike (Figure 1.4.1). The use of Google Earth images made it possible to continue the tracing further East.

3.3.3 Altitude of log

Precision of log altitudes is preferable, especially in areas where there is a missing overlap between logs and Lidar. Log altitudes were obtained by using a Garmin Oregon [®]600 series

3. Method

handheld GPS receiver. Due to time constraints, not all of the log altitudes were recorded but log altitude was obtained from log 1, 5, and 8.

4. DATABASE

It should be pointed out that the database for the Humbug Flats area, compiled as part of the COPASS project, is a work in progress. Several datasets were still in the process of being collected and were in an incomplete state at the time of submission of the present thesis. The database presented here only includes data provided by the COPASS project group that was available as of May 2017. With respect to the project, the model generated from these data should therefore be considered a status report rather than a finalized product. The database used in the present project was compiled from a variety of sources, including publically available data and a series of Master theses attached to the COPASS project (Larsen, 2015; Hope, 2015; Rimkus, 2016; Gurrik, 2016; Sleveland, 2016 and Kristensen, in prep.). Some additional data (miniperm measurements, altitude checks, field tracing of the main fault and some geomechanical measurements) were collected during a short visit to the area in May 2017. The database comprises:

- Sedimentary logs of the Entrada sandstone and Curtis Formation, including descriptions of facies and facies associations.
- Porosity measurements; mainly based on thin section studies
- Permeability measurements; mainly field measurements using a TinyPerm II instrument
- Lidar images with interpreted surfaces and stratigraphic boundaries
- Google Earth images
- A digital elevation model

Supporting information for understanding the stratigraphy and depositional environment of the Entrada sandstone and the Curtis Formation was provided by Zuchuat et al. (in prep.). Sundal (pers. Comm.) and Skurtveit (pers. Comm.) provided additional geomechanical measurements.

.

4. Database

The multi-source database employed here presents several potential challenges which should be considered when employing it for modelling purposes:

- Resolution issues when trying to match altitude measurements from logs and altitudes derived from the DEM and Google Earth
- Precision of log altitudes
- Missing overlap between logs and Lidar images
- Lateral and vertical limitations of the Lidar images
- Some datasets only cover part of the stratigraphic succession
- Consistency of facies definitions and descriptions

These issues are partly addressed in the description of the individual datasets below, and partly in the modelling chapter, as they affect the quality and precision of the final model.

4. Database

4.1 Sedimentary logs and descriptions

A total of 16 outcrop logs have been compiled in the study area by Hope (2015), Larsen (2015), Gurrik (2016), Rimkus (2016) and Sleveland (2016) (Figures 4.1.1). The logs and detailed coordinates are listed in Appendix A. Thickness information about the facies associations are listed in Appendix B. As can be seen in Figure 4.1.1, only some of the logs are located in sections from which Lidar images are available. The outcrops display the Entrada sandstone (Earthy Mb.), truncated by the regional J-3 unconformity and overlain by the Curtis Formation. Seven facies associations are recognised in this succession; details are provided in Tables 4.1.1 to 4.1.4.

4.1.1 Entrada Sandstone
Gurrik (2016) focused on the damage zone characteristics of the main fault intersecting the area. Hope (2015) studied deformation bands in regards to how and why they form within the Fremont bed. Gurrik (2016) and Hope (2015) are not consistent in facies definitions and descriptions. The log by Hope (2015) in the Entrada sandstone was considered to have too low resolution to be able to extract and allow digitization for model implementation; however, the facies descriptions for the Fremont bed have been used. For further work, Gurriks facies descriptions are used. Gurrik (2016) collected two sedimentary logs in the upper part of the Entrada sandstone in the study area; one in the hanging wall and one in the footwall of the large East-West running fault. Three facies associations, e_FA1- e_FA3, were observed. These logs were digitized in RMS (Appendix A).
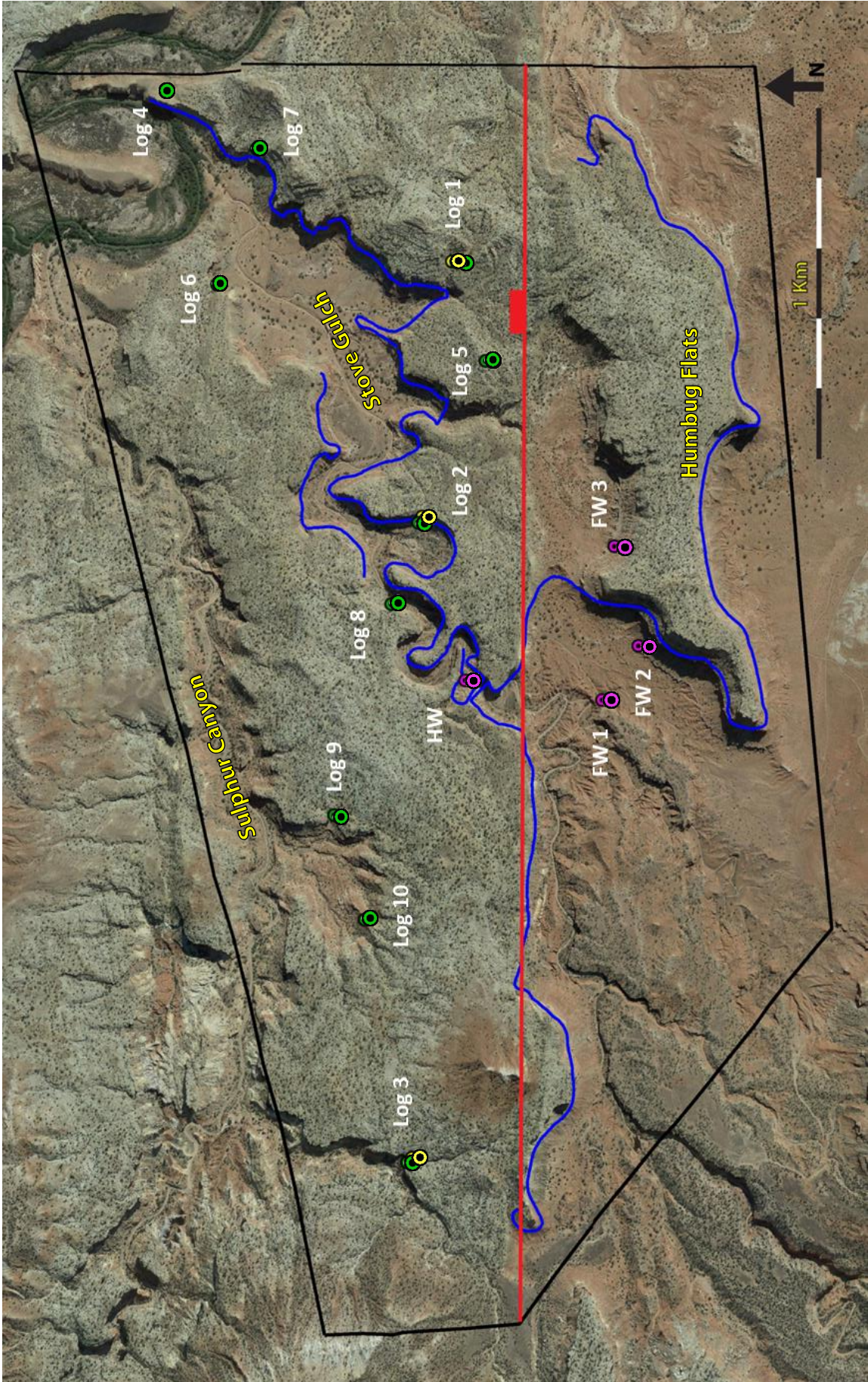
Figure 4.1.1: The logging localities represent the start point of the logs. Green corresponds to Rimkus (2016), yellow Sleveland (2016) and pink Gurrik (2016). The position of the fault is an approximation. Photo: Google Earth.

4. Database

Table 4.1.1: Facies descriptions from the Entrada sandstone (modified from Gurrik (2016)).

Facies:	Abbreviations:	Description	Structures:	Interpretation:
e_A		Very fine to medium grained sandstone interbedded with thinner more fine-grained layers	• Desiccation cracks • Root traces • Soft sediment deformation • Subhorizontal and wavy lamination • Ripples • Tangential cross-stratification	Wet eolian dune, Wet interdune, Floodplain deposit
e_B		Mudstone interbedded with clay-, silt- and sandstone layers	• Subhorizontal and wavy lamination • Small scaled ripples • Calcite-filled fractures	Wet eolian dune, Wet interdune, Floodplain deposits
e_C		Siltstone and very fine sandstone	• Laminated • Small-scale cross-stratification • Asymmetrical ripples • Root traces • Calcite-filled fractures • Bioturbation	Wet interdune
e_D		Siltstone	• Horizontal and wavy lamination • Root traces • Calcite filled fractures	Wet eolian dune, Wet interdune, Floodplain deposits
e_E		Pale coloured fine to medium grained sandstone	• Tangential cross-stratification • Horizontal lamination • Deformation bands in NW-SW direction	Wet interdune, (Fremont bedding)
e_F		Paleo coloured very fine to fine grained muddy sandstone	• Deformation bands in NW-SW direction • Weak subhorizontal lamination	Wet interdune
e_G		Claystone, interbedded with fine grained mud-, silt- and sandstone	• Subhorizonal and wavy laminated	Floodplain deposits

4. Database

Facies associations:

Gurrik (2016) suggested grouping the interpreted facies into three facies associations.. These
include wet interdune deposits, wet eolian dune and floodplain deposits (Table 4.1.2).

Table 4.1.2: Overview of facies association, depositional environment and involved facies for the Entrada sandstone
(modified from Gurrik (2016)).

Facies association:	Facies:	Structures:	Depositional environment:
e_FA1	e_A, e_B, e_C, e_D, e_F	- Weak subhorizontal lamination - Weathering and bioturbation have destroyed the primary structures - Root traces - Bioturbation with bleached patches - Desiccation cracks - Soft sediment deformation - Contain deformation bands	Wet interdune
e_FA2	e_A, e_B, e_D	- Massive - Stratified - Desiccation cracks - Soft sediment deformation - Root traces	Wet eolian dune
e_FA3	e_A,e_B,e_D,e_G	- Planar lamination - Ripple lamination - Root traces - Small-scale cross-stratification	Floodplain deposits
e_FA4	e_E (Fremont bed)	- Significant amount of deformation bands - Subhorizontal lamination - Cross-stratification	Wet eolian dune

Facies association 1 (e_FA1): Wet interdune deposit

Facies association 1 consists of thick siltstone beds (facies e_D), thinner sandstone (facies
e_A), mudstone (facies e_B), silt-/ very fine sandstone (facies e_C), and very fine to fine
grained pale-coloured muddy sandstone (facies e_F) beds. The presence of roots, desiccation
cracks, pervasive bioturbation and poorly developed paleosols suggests episodic deposition,

interrupted by quiescent periods allowing vegetation to form. The sediments are interpreted as deposited within an potentially ephemerally flooded interdune environment, strongly influenced by a near surface water table.

Facies association 2 (e_FA2): Wet eolian dune

Facies association 2 constitutes the middle and uppermost exposed part of the Entrada sandstone, and is composed of very fine to medium-grained sandstone (facies e_A) with thin mudstone (facies e_B) and siltstone (facies e_D) units. Hematite and other iron oxides lend the deposits a reddish- brown colour. Bleaching of individual beds or bleached haloes surrounding fractures are observed within these sediments. The depositional environment is interpreted to be a wet eolian dune system, where water table is near the deposition surface. The massive sandstone units indicate rapid, wind driven deposition, while the muddy facies suggest occasional flooding of the dune margins.

Facies association 3 (e_FA3): Floodplain deposits

Facies associations 3 consist of several upward fining sections of sandstones (Facies e_A), mudstones (Facies e_B), siltstones (Facies e_D) and claystones (Facies e_G). Planar and ripple lamination, as well as root traces are observed. Gurrik (2016) interpreted the depositional environment as being an ephemeral stream floodplain, where fine grained material was deposited during low energy phases following inundation. e_FA3 is observed separating eolian dunes (e_FA2) and wet interdune deposits (e_FA1).

Facies association 4 (e_FA4): Bleached eolian dune (Fremont bed)

Facies association 4 consists of a single facies, e_E. It consists of a 2.7 m thick, conspicuously bleached very well sorted fine sandstone bed, with iron stained, red sandstone and shale-mudstone below and above (Hope, 2015). Hope (2015) introduces the term Fremont bedding for the unit. In accordance with the rules in International Union of Geoscience (IUGS), the designation of the layer is Fremont bed and not bedding (Murphy & Salvador, 1999). Gurrik (2016) described the Fremont bed exhibiting trough cross-stratified beds and sub-horizontal lamination in her field area close to the East-West fault (Figure 4.1.1). Reconnaissance in a wider area shows low-angle cross beds and metre-sized dunes with low-angle re-activation surfaces. The absence of finer grain fractions, together with the sedimentary structures and sorting, suggest that the Fremont bed represents an eolian dune field, possibly deposited during a period with drier conditions than indicated by the sediments

over- and underlying the bed. Root growth can be observed in the upper part of the bed (Gurrik, 2016), indicating stabilization of the sediment surface, most likely linked to a rising ground water table. The Fremont bed exhibits high frequencies of deformation bands with preferred NE-SW orientation (Gurrik, 2016; Hope, 2015). The presence of a significant amount of deformation bands in this bed is interpreted as a consequence of a collapse of this bed or a folding event (Hope, 2015; Larsen, 2015). There are numerous observations of fluidization and movement of reducing fluids (bleaching) associated with the Fremont bed, which seem to support the idea of sudden pressure changes and collapses having caused the generation of the deformation bands.

Correlation of the Entrada log
Inconsistency in the description and the logging of the Entrada sandstone and lack of sedimentary description and logging from the study area the logging performed by Gurrik (2016) was correlated (Figure 4.1.2). For correlation and simplification purposes, it is assumed that the sedimentary succession contains the same facies association order on both sides of the fault. The sedimentary succession can be seen as being cyclic within the Entrada sandstone. Wet eolian dune deposits (e_FA2) are located between fine and coarse interval of wet interdune (e_FA1) and floodplain deposits (e_FA3).

4. Database
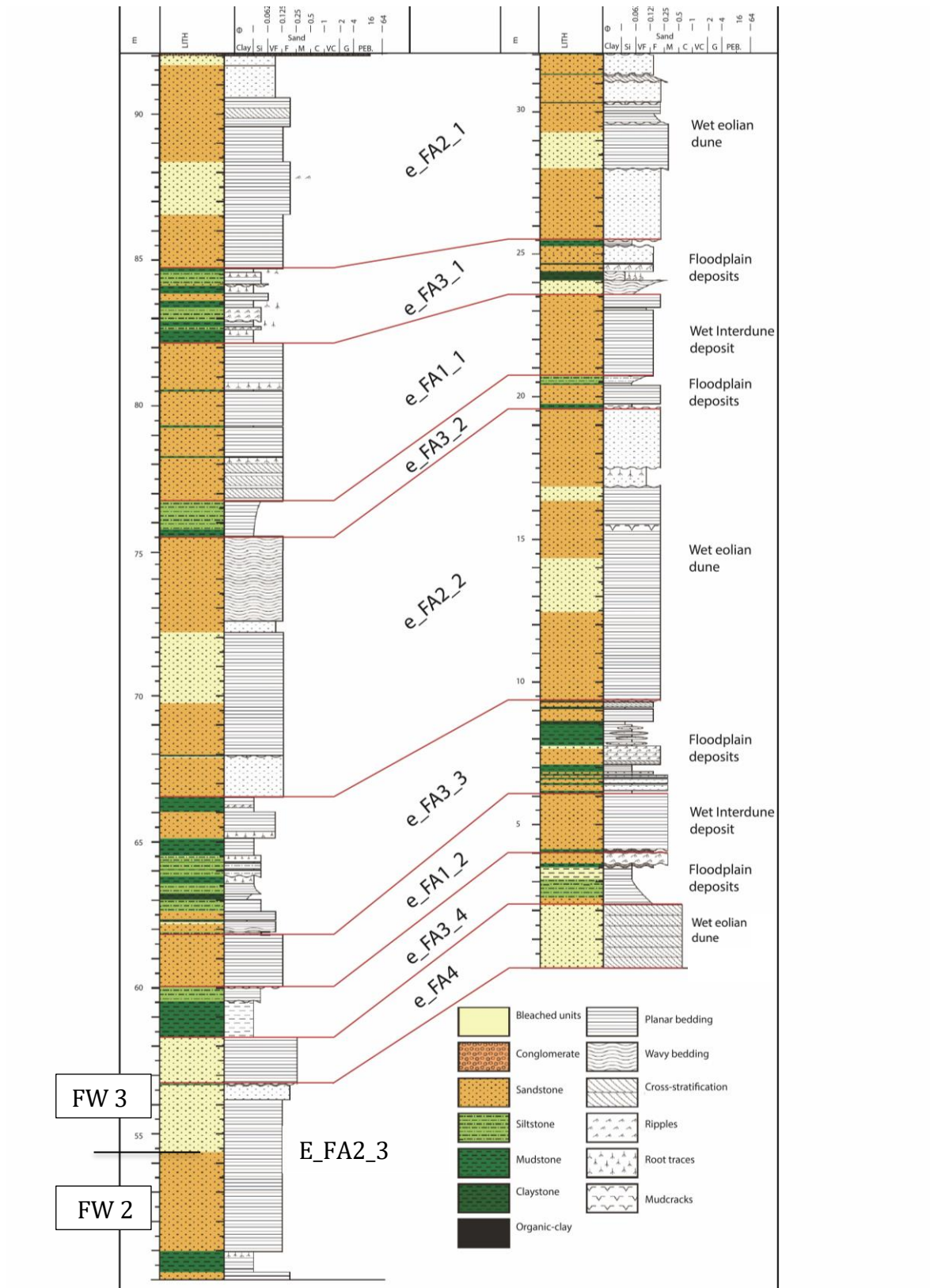
Figure 4.1.2: Correlation and modification of stratigraphic logs of the footwall (left column) and hanging wall (right column) (modified from Gurrik (2016)). Lowermost facies association is the Fremont bed on the hanging wall. E_Top_FA2_3 is included in the model and can be observed under the Fremont bed on the footwall See Appendix A.2 for digitalization of the logs.

4.1.2 Curtis Formation

The work of Rimkus (2016) and Sleveland (2016) focused on identifying the J-3 unconformity and logging the overlying unit, and provide a description of facies and facies associations in the Curtis Formation. Rimkus (2016) logged ten sections in the study area; four of these coincide with three of the sections in Sleveland (2016), which increases the reliability of these logs. The logs are shown in Appendix A. The description of facies and facies associations is summarized in Table 4.1.3 and 4.1.4.

Rimkus (2016) provides digitized cm-scale sedimentary logs in Petrel, which include facies, facies associations, start coordinates and stratigraphic thicknesses. These logs were imported into RMS and constitute the key input for modelling facies distributions in the Curtis Fm. and the position of the J-3 unconformity in the sections. Where the logs coincide with the Lidar image coverage, the former was used to identify and interpret key horizons in the latter.

4. Database

Table 4.1.3: Nine facies were identified in the Curtis Formation based on texture, structure and colour as well as other distinguishable features. Tidal mudflat deposits (A and B) are merged together and named TMF (Modified from Rimkus, 2016).

Facies:	Abbreviations:	Grain size:	Bedding:	Structures:	Interpretation:	Depositional environment:
c_A	TMF	Si-Vf		Plane parallel lamination, Asymmetrical ripples	Upper intertidal mud flats. Asymmetrical ripples indicate tidal influenced environment.	Tidal mud flat
c_B	TMF	Si-Vf		Asymmetrical ripples Horizontal laminations	Intermediate energy deposition in tidally influenced environment	Tidal mud flat
c_C	TSF_1	Vf-F		Horizontal and low-angle cross-bedding, Current ripples and wave ripples	Upper flow regime. Mud draping during slack water phase	Tidal sand flat
c_D	TCD	Vf-F		Trough cross-bedding, Mud drapes, Desiccation structures	Unidirectional tidally influenced migration of dunes in channels	Tidal channel deposit
c_E	SSB	Vf-F	Flaser - bedded	Asymmetrical ripples, herringbone cross-lamination, mud lenses and double mud drapes	Tidally influenced environment	Subtidal Sandbar
c_F	TSF_2	Vf-F	Wavy –bedded	Herringbone cross-stratification, 3D ripples, Horizontal bioturbation, wavy bedded mudstone and sandstone	Flood and ebb tides	Tidal sand flat of sub intertidal zone**
c_G	OLE	Si-F	Lenticular bedded	Herringbone cross-stratification, rippled sand lenses, current ripples Horizontal bioturbation	Subtidal low energy deposition. Minor tide influence.	Subtidal zone*

4. Database

c_H	MTCD	M-Gr		Tabular and trough cross-stratification, Ripples	Strong unidirectional component: migration of 3D dunes in a major tidal channel	Major tidal channel deposits
c_I	PBD	M-Gr Local mud clasts chert pebbles		Inclined heterolithic stratification Poorly sorted	Deposition in migration subtidal channels: erosion of channel banks	Tidal channel point bar

Interpreted as offshore low energy deposition by Rimkus (2016). This does not seen likely when compared to Sleveland (2016) (Zuchuat pers. Comm).

** Interpreted as estuarine passive infill this does not seem likely and interpreted as tidal sand flat (Zuchuat pers. Comm.).

Facies associations:

The Curtis Formation can be divided into five facies associations (Table 3). Facies association 4 can be subdivided into two, FA4a and FA4b.

Table 4.1.4: Facies associations, associated facies and depositional environment (Modified from Sleveland, 2016)

Formation Fm.	**Facies association:**	**Depositional environment:**	**Facies:**
Summerville Fm.		Marginal marine	
Curtis Fm.	c_FA5	Upper intertidal	c_A, c_B
	c_FA4b	Beach with tidal inlets	c_C, c_D
	c_FA4a	Sub-intertidal	c_E, c_F
	c_FA3	Subtidal	c_E, c_G
	c_FA2	Tidal transition	c_G, c_ H, c_ E
	c_FA1	Sub-tidal shelf	c_G, c_I
Entrada sandstone		Coastal eolian	

Facies association 1 (c_FA1): Subtidal shelf deposit

Facies association 1 is observed mainly in the lower part of the Curtis Formation, commonly directly overlying the Entrada sandstone and the J-3 unconformity, except in logs 6, 9 and 10, where J-3 is overlain by c_FA2 (see below). c_FA1 consists of mud-rich lenticular-bedded facies c_G, and inclined heterolithic bedding (facies c_I) is found in the lowermost strata of

log 8. Conglomerates are found along the bedding, reflecting erosion and incision associated with the deposition of c_FA1. Thickness of c_FA1 varies significantly both as a result of subsequent erosion at the base of the overlying c_FA2, and the local depth of erosional depressions associated with the J-3 unconformity. According to Rimkus (2016), the thickness of c_FA1 shows a general increase from North to South (from 1 to 4-5 m). Rimkus (2016) argues in favour of a sub-tidal depositional environment based on the greenish-grey coloration of the mud facies, indicating a reducing rather than oxidizing depositional environment which is what would be expected for a inter to supratidal environment.

Facies association 2 (c_FA2): Subtidal channel infill

This facies association differs from c_FA1 by generally exhibiting coarser, sediments and containing facies reflecting stronger currents. It encompasses facies c_H (Major tidal channel), c_G (lenticular mudstone) and facies c_E (subtidal sand bars). Dunes (facies c_H) and tidal bars (facies c_E) fill in the channels. In some parts of the outcrop, this facies association carves into the underlying Entrada sandstone and c_FA1 where it overlies the J-3 unconformity. Major tidal channels are frequent in the lower 20 meters of the Curtis Formation. Where the facies association directly overlies the J-3 Unconformity, dunes associated with major tidal channels (facies c_H) are observed. The mud-beds represent periods of lower energy conditions, suggesting local relocation or periodic de-activation of channels.

Facies association 3 (c_FA3): Passive infill of channels

Facies association 3 comprises lenticular (facies c_G) and flaser (facies c_E) bedded mud and sandstones. Rimkus (2016) interpreted c_FA3 as passive infill of channels in a constricted bay environment. c_FA3 is observed in all of the logs, and is observed throughout the study area, generally seen overlying c_FA1 or c_FA2 and are in most cases succeeded by c_FA4.

Facies association 4 (c_FA4): Sand flat deposits

Facies association 4 is observed in the middle to upper part of the Curtis Formation, almost invariably overlying c_FA3. It is laterally extensive and is expected to have covered the entire study area. Facies association 4 is subdivided in two sub facies associations: Sub- to intertidal deposits (c_FA4a and c_FA4b).

4. Database

c_FA4a is found in the lower part of the facies association, and comprises of subtidal sand bars (Facies c_E) and tidal sand flat (Facies c_F). The uppermost part of the facies association (c_FA4b) consists mainly of alternating tidal sand flats (Facies c_C) and tidal channel deposits (c_D). Paleocurrent measurements show a strong NW-SE oriented current in the tidal sand flats. This is at an angle to the interpreted N-W oriented shoreline. An upward thinning trend into overlying c_FA5 is observed.

Facies association 5 (c_FA5): Mixed and mud flats

The facies association is found in the uppermost part of the Curtis Formation and is always overlying c_FA4 in the sections logged by Rimkus (2016) (logs 1, 3, 4, 7, 9 and 10). The lateral extent is hard to trace, as it has been eroded in most places, and c_FA5 is only found as erosional remnants on local hilltops. Due to its topographic position, the facies is not captured in the Lidar scans. c_FA5 comprises tidal mud flat (facies c_A and c_B). Due to scree cover it is difficult to determine sand- mud ratio and the accurate thickness of c_FA5, but in log 6 it is overlain by the Summerville Formation, and exhibits a thickness of about 8 m.

4.2 Porosity and permeability

Porosity and permeability data was compiled from several sources (Table 4.2.1). A full list is provided in Appendix C. In general the petrophysical data is relatively scant and unevenly distributed.

Table 4.2.1: The tables show the available petrophysical properties for the facies within each of the facies associations for the Curtis Formation and Entrada sandstone.

Curtis Formation

	c_A: Tidal mud flat	c_B: Tidal mud flat	c_C: Tidal sand flat	c_D: Tidal channel deposits	c_E: Subtidal sand bars	c_F: Tidal sand flat (FA4a)	c_G: Lenticular mudstone	c_H: Major tidal channel deposits	c_I: Channel
c_FA5	▨(grey)	◯✕							
c_FA4			◯✕	◯✕	◯✕	▨(grey)			
c_FA3				▨(grey)			▨(grey)		
c_FA2				▨(grey)			▨(grey)	◯✕	
c_FA1							▨(grey)		◯✕

Legend:
- ◯ Porosity
- ✕ Permeability
- ▢ Geomechanical properties

Colour:
- ■ (black) Author
- ■ (yellow) Hope (2015)
- ■ (red) Larsen (2015)
- ■ (green) Rimkus (2016)
- ■ (blue) Kristensen (in prep.)
- ■ (orange) Sundal (pers. Comm.) and Skurtveit (pers. Comm.)

Entrada sandstone

	e_A: Sandstone	e_B: Mudstone	e_C: Siltstone-vf.sandstone	e_D: Siltstone	e_E: Pale sandstone	e_F: Pale muddy sandstone	e_G: Claystone
e_FA2_1	▨(grey) ✕(orange)	▨(grey)		▨(grey)			
e_FA3_1	▨(grey)	▨(grey)		▨(grey)			▨(grey)
e_FA1_1	▨(grey)	▨(grey)	▨(grey)	▨(grey)		▨(grey)	
e_FA3_2	▨(grey)	▨(grey)					
e_FA2_2	▨(red) ⊗(blue) ✕(orange)	▨(grey)		▨(grey)			
e_FA3_3	▨(red) ⊗(blue) ✕(orange)	▨(grey)		▨(grey)			▨(grey)
e_FA1_2	▨(red) ⊗(blue) ✕(orange)	▨(grey)	▨(grey)	▨(grey)		▨(grey)	
e_FA3_4	▨(grey)	▨(grey)		▨(grey)			▨(grey)
e_FA4 (Fremont)					✕(orange) ✕(black) ◯(yellow) ⊗(blue) ▨(red)		
e_FA2_3	▨(red) ⊗(blue) ✕(orange) ✕(black)	▨(grey)		▨(grey)			

4. Database

4.2.1 Entrada sandstone

The petrophysical data from the Entrada sandstone are clustered on the Fremont bed; there are no poro-perm measurements from the upper part of the Entrada sandstone. The data for the modelling was compiled from Hope (2015), Gurrik (2016), Rimkus (2016) and Kristensen (in prep.). Hope (2015), focused on identifying differences between different deformation bands within the Fremont bed. Hope (2015) produced porosity estimates on deformation bands and host rock, as well as a few permeability measurements in the field using a TinyPerm 2 instrument. Porosities were estimated from SEM backscatter images of thin sections. In order to implement host rock and deformation band porosity in the model, a fracture network is necessary. This is not included in this thesis, as the data is still in process of being collected. On the other hand, host rock porosity has been used. According to her comments, the porosity measurements have a high uncertainty.

Larsen (2015) and Kristensen (in prep.) address the geomechanical properties related to fractures, deformation bands and faults within the Entrada sandstone. They provide porosity and permeability values for some of the facies (Table 4.2.1). Challenges encountered when placing these values stratigraphic. They used other facies definitions and descriptions that made it difficult to relate to the two logs conducted by Gurrik (2016). This problem was solved in the field are May 2017 (Table 4.2.2).

Table 4.2.2: Corresponding facies definition and facies associations for Larsen (2015), Kristensen (in prep.) and Gurrik (2016).

Layer:	Facies association:
Layer 10	e_FA2_1
Layer 9	e_FA2_1
Layer 8	e_FA1_1
Layer 7	e_FA2_2
Layer 6	e_FA2_2
Layer 5	e_FA2_2, e_FA3_3
Layer 4	e_FA1_2
Layer 3	e_FA4 (Fremont)
Layer 2	e_FA2_3
Layer 1	e_FA2_3

Some supplementary TinyPerm measurements were carried out by the author during a short visit to the field area in May 2017. See Appendix D for details.

4. Database

4.2.2 Curtis Formation

Porosity and permeability measurements from the Curtis Fm. are relatively few in number and consist of a porosity dataset supplied by Rimkus (2016) and a set of TinyPerm measurements collected by the author.

Rimkus (2016) collected 10 samples from the middle Curtis for grain size measurements, mineralogical characterization, and estimation of the porosity of the facies. High friability of the rocks due to high mud content made it difficult to obtain samples from the lowermost and uppermost parts of the Curtis Formation, which therefore lack porosity measurements. Porosity estimates are not available for Facies c_F and Facies c_G within the Curtis Formation. Rimkus (2016) does not provide any permeability measurements from the Curtis Formation. Porosity and calcite cement values from his work are listed in Appendix C. The only permeability data from the Curtis Fm. in the modelled area consists of a limited series of TinyPerm measurements performed at the site of Rimkus Log 1 by the author (Appendix D).

The available porosity and permeability data for the Entrada sandstone and Curtis Formation are very limited. The Fremont bed and surrounding layers are relatively well covered, but the upper part of the Entrada sandstone lacks any data, and both porosity and permeability measurements for the Curtis Fm. are in many cases restricted to single samples or measurements which cannot unequivocally be claimed as representative. This lack of a comprehensive dataset allowing actual porosity and permeability variation to be assessed severely constrains any attempt at 3D petrophysical modelling.

4.3 Google Earth Pro

Google Earth was frequently used, mainly to be able to orient in space. The Lidar group provided positioning of scan positions and the scanned outcrop. The coordinates from the logs were digitized in Google Earth Pro for better visualization of the area. Based on visualization in Google Earth Pro, the main fault intersecting the study area was traced. A picture from Google Earth pro was also used to texture the digital elevation model.

4.4 Digital elevation model (DEM)

A digital elevation model (DEM) model with 9x9 m resolution of the study area was provided by the Bergen Lidar Group. The DEM was imported into RMS and a Google Earth image was draped onto the surface for a better visual effect. The DEM was mainly used for tracing the logging path for Rimkus logs, tracing the main fault, and to generally get an overview of the area together with the implemented data.

4. Database

4.5 Virtual outcrop

Benjamin Dolva, Adam Cawood and Luisa Zuluaga collected more than 9 km of outcrop Lidar images over a period of 3 days in spring 2015. 52 scans were acquired and segmented in 15 sections (Figure 4.5.1). Processing was performed by Benjamin Dolva, and the resulting 3D images were transferred to Lime for interpretation.

The picture resolution is 0.005 m at 100 m distance, captured with an 85 mm lens. This is the resolution of the image laid flat. The resolution varies as a result of the image being stretched out to fit the 3D-modell. Lightning conditions affect the resolution of the data as areas with too much lighting or areas with shadow effects are difficult to interpret. Areas, especially in scan 2 and 3 are covered with a lot of shredding material, making it impossible to interpret in this area. The area through Stove Gulch is not continuously scanned; this is most likely due to difficulties related to the angle of acquisition. Some of the blocks in area scan 2-3 have been rotated dislocated blocks that are observed on the Lidar image, but not that they were dislocated (Figure 4.5.1). This was observed in the field.

As can be observed from Figure 4.5.1, the outcrops at Humbug Flat provide a potentially very good 3D view of the stratigraphy. Although the Lidar scans cover a substantial part of the outcrops, a number of the logged sites are not in outcrops covered by the virtual outcrop images. Taken together with the fact that some of these logs have uncertain height references, it was in several instances difficult to trace stratigraphic contacts between outcrop image and logs outside the scanned areas.

The Lidar images do not cover the lower slopes and valley bottoms, nor the hill- crests. This shortcoming prevented attempts at interpreting structural features such as bleached fractures located on flat-lying area. It furthermore precluded tracing some stratigraphic contacts located near hill tops. In hindsight, and considering the topographic complexity of the model area, a photogrammetric survey using a drone would have probably has rendered a more suitable image to use to perform an interpretation.
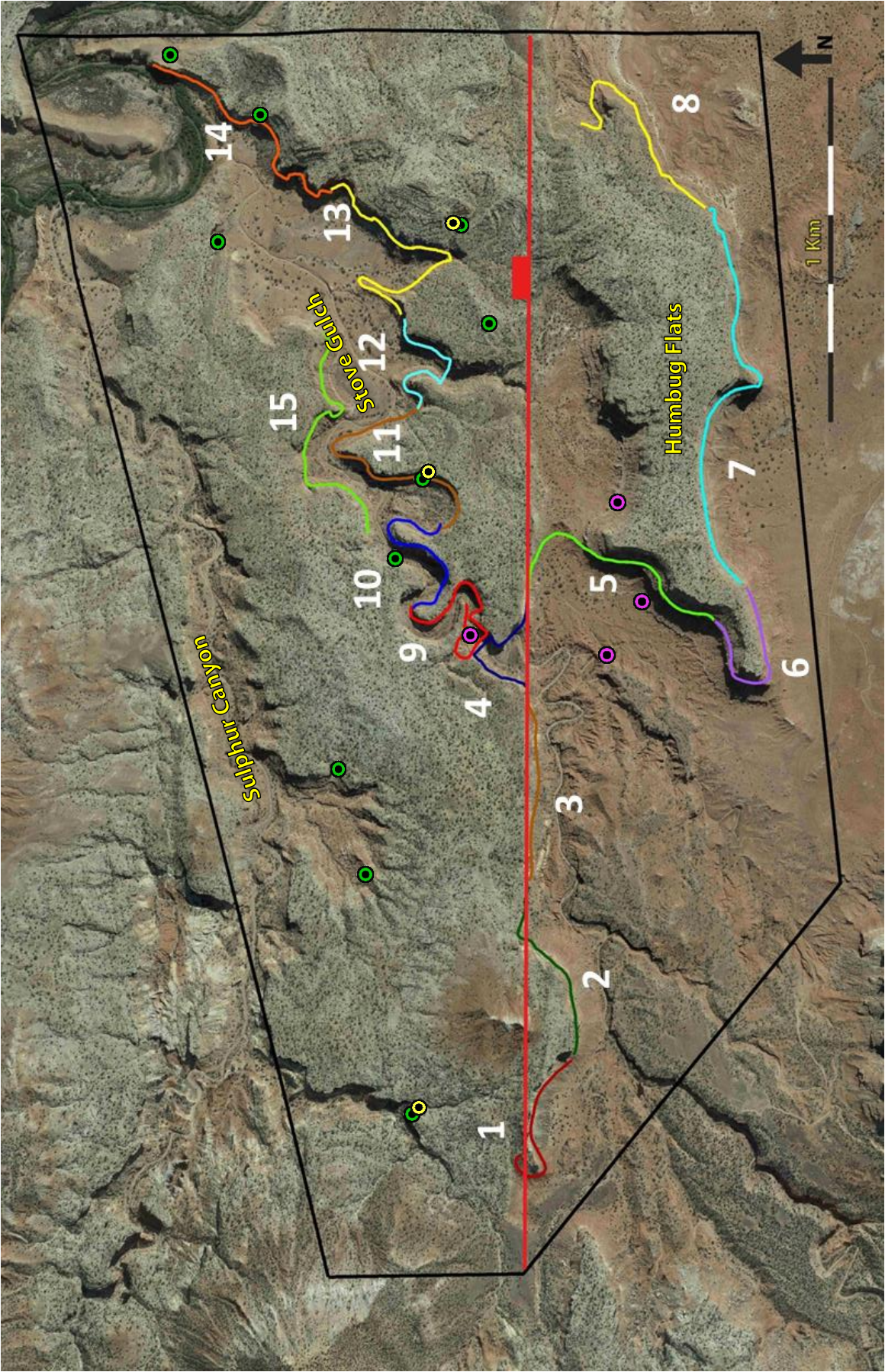
Figure 4.5.1: Location of Lidar scans. Placement of the fault is an approximation.

5. VIRTUAL OUTCROP INTERPRETATION

This chapter describes the interpretation of the Lidar scans. The lateral extent of the facies associations can be determined from the images. Thickness measurements are based on logs for the Curtis Formation, and for the Entrada sandstone the thickness is measured on the outcrop using Lime. Thickness measurements are found in Appendix B.1.

J-3 unconformity

J-3 unconformity was interpreted along all of the outcrops. The unconformity can be observed cutting down into the Entrada sandstone. In addition, it is possible to see an erosive contact where major tidal channels have eroded into the Entrada sandstone.

Entrada sandstone

Limited data from the lowermost part of the outcrop of the Entrada sandstone, led to a discontinuous interpretation of the lowermost units. Fremont bed is the lowermost unit interpreted of the Entrada sandstone. The meter thick floodplain deposit e_FA3_2 is not interpreted on the Lidar scan as it is difficult to detect (Figure 4.1.2). Interpretation is based on Gurrik (2016) log and the transition between to facies associations. Figure 5.1 shows the interpretation of the outcrop in Lidar segment 15.

Figure 5.1: Interpretation of Entrada sandstone from scan 15, see Figure 4.5.1 for location.

5. Virtual outcrop interpretation

e_FA1: Wet interdune deposits

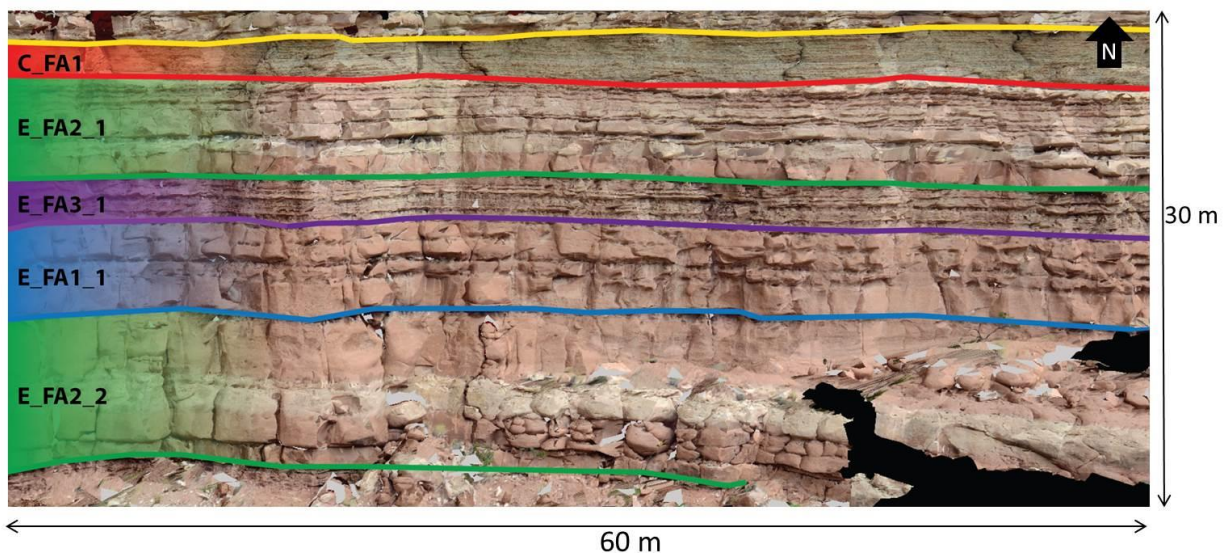Two units of wet interdune facies association can be traced throughout the study area on the Lidar segments. The first sandstone unit (e_FA1_1) is observed 8.5 meters under the J-3 unconformity in the hanging wall, and thickness measurement on Lidar data shows that it ranges between 2.47 and 5.6 meters. The facies comprises of two thick sections of siltstone and thinner units of sand-, mud- and claystone (Figure 5.1). The second wet interdune deposits (e_FA1_2) can be observed as a single fine sandstone bed with 2.2 m mean thickness.

e_FA2: Wet eolian dune

Two successions of wet eolian dunes are observed in the Lidar segments, e_FA2_1 and e_FA2_2. A pale-colour can be observed in the middle part of the sandstone units, and the succession can easily be traced over the study area, as the massive unit is different from the fine grained surrounding units (Figure 5.1). The facies association e_FA2_1 is observed directly below the J-3 unconformity. Measurements from the Lidar scan show that the mean thickness of the facies association is 7.38 m thick. The e_FA2_2 unit can be observe in the Lidar segments, exceptions are in segment 3, 5 and 14 where the image is covered by scree. Measurements show that the mean thickness is 9.5 m.

e_FA3: Floodplain deposits

This facies association differ from the others, as this is more layered and consists of finer sediments. Two floodplain deposit units can be interpreted on the footwall 5-8 Lidar segments (e_FA3_1 and e_FA3_3). On the hanging wall, Lidar segments 9-15, e_FA3_3 are not interpreted as the area is covered by scree. e_FA3_2 The mean thickness is measured to be 2.64 m of e_FA3_1, 3.85 m of e_FA3_2 and 1.79 m of e_FA3_3.

Curtis Formation

Only the lowermost of the Curtis Formation is displayed in the Lidar segments, up to c_top_FA3. In the footwall, Lidar segment 1-2 (Figure 4.5.1) the J-3 unconformity is interpreted and facies association c_FA2 is observed directly overlaying the unconformity. In the footwall, Lidar segments 5-8 c_FA1 can be interpreted in parts of the outcrop where there is available data, and where FA2 is not incising into the Entrada sandstone. Top_c_FA3 can only be observed in scan 6 and in parts of scan 7. It is expected that Top_c_FA2 is found

43

5. Virtual outcrop interpretation

between Top_c_FA1 and Top_c_FA3, but the transition is not interpreted as the area is covered with scree.
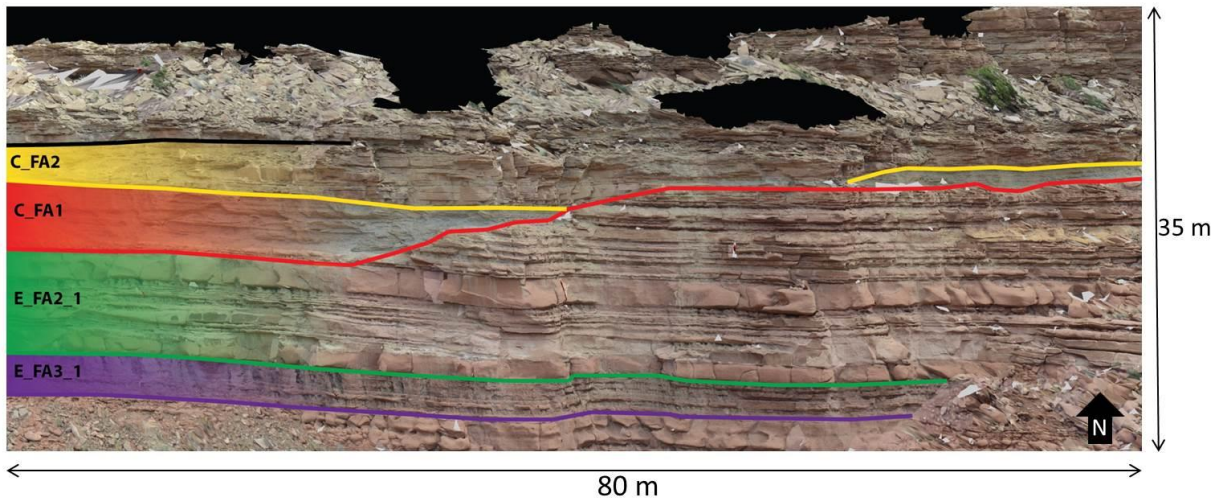
Figure 5.2: The red line represents the J-3 unconformity, the transition between top Entrada and base Curtis. Facies association two (C_FA2) has incised into the underlying facies and facies one (C_FA1) is eroded. The picture is from the footwall in scan 7, see Figure 4.5.1 for location.

c_FA1: Passive infill

The facies association can be traced continuously in the lowermost part of the Curtis Formation directly overlying the J-3 unconformity; exceptions are when c_FA2 have incised into the Entrada sandstone (Figure 5.2). This is the case South-East in the study area, scan 7 (Figure 5.2) and near log 6, 9 and 10, where the area lack Lidar coverage. The transition from the underlying Entrada sandstone can easily be traced in the Lidar images, as it is finer grained than the surrounding facies. The thickness of the lowermost facies association ranges from 0.25 to 4 meters, and mean thickness is found to be 2.4 meters.

c_FA2: Tidal transition

The facies association differs from the underlying facies (c_FA1) as it is more massive and consists of more outstanding facies. It encompasses facies H (Major tidal channel), I (Subtidal channel), G (Lenticular mudstone) and facies E (subtidal sand bars). The facies association makes a sharp erosive boundary to the underlying facies, due to incising of sub-tidal channel. In some parts of the outcrop, this facies is incised into the underlying Entrada sandstone, making c_FA1 absent (Figure 5.2), and the facies is directly overlaying the J-3 unconformity. A common relief of the erosional surface is 7 m over a 100 m lateral extent.

5. Virtual outcrop interpretation

The thickness range between 0.25 and 10.98 meters, the median is calculated to be 4.5 meters. The facies is observed pinching out. Correlation between the facies association on Lidar scan makes it possible to trace c_FA2 continuously along scan 11-14 from log 2 to 7. This correlation distance is measured to be 1504 m. In some areas, the facies association is not present or found as a single dune or two simple dunes. The dunes are separated by mud-rich intervals (Facies G).

c_FA3: Subtidal

The facies association consist of subtidal sand bars interbedded with lenticular bedded mudstone. The facies association is traced in scan 3, 6, and 7 in the footwall, and scan 9-11, 13 and 14, nearly as a horizontal surface. It distinguishes the mud and sandstone from the overlying coarser grained sandstone. The Lidar image is not covering the top of the outcrop, and therefore it is not detectable in all the scans, but it is observed in all of the logs. It is predicted that it is an extensive succession observed over the study area. Thickness measurements from facies association 3 show that the mean thickness is 2.47 meters.

c_FA4: Sub-intertidal to beach with tidal inlets

It is possible to detect the transition from FA3 to FA4 on the Lidar image, the exception are scan 1-5, 8, 12 and 15. The image cuts the facies and the resolution makes it difficult to determine the different facies. The facies association is laterally extensive and covers the study area. In the eastern towards the western part tidal channel deposits overlie subtidal sandbars and the transition from FA3 to FA4 is easily recognized in the outcrop. In the western part, subtidal sand bars are overlaid by wavy-bedded sandstone. The upper boundary to FA5 is therefore not observed in the Lidar scan, but is logged in some areas (log 1, 3, 4, 7, 9 and 10), and is therefore estimated from the ten logs conducted by Rimkus (2016). It is expected that the transition to FA5 is a gradual thinning.

6. GEOLOGICAL MODELLING

This chapter describes the modelling strategy and the modelling procedure from input data to a facies model.

6.1 Introduction to modelling strategy

The aim of this study is to build a 3D-model of the study area using available observations (Chapter 3 and 4). The areal extent of the model area is limited by the project boundary (Figure 6.4.1), circumscribing the logged field localities and scanned outcrops at Humbug Flats; an area of about 7.2 km^2. Lidar interpretations and logged sections were quality controlled and made consistent as described in section 4.2.1. The modelling procedure used here is illustrated schematically by the flow chart in Figure 6.1.1. Each step will be described thoroughly in the following sections.
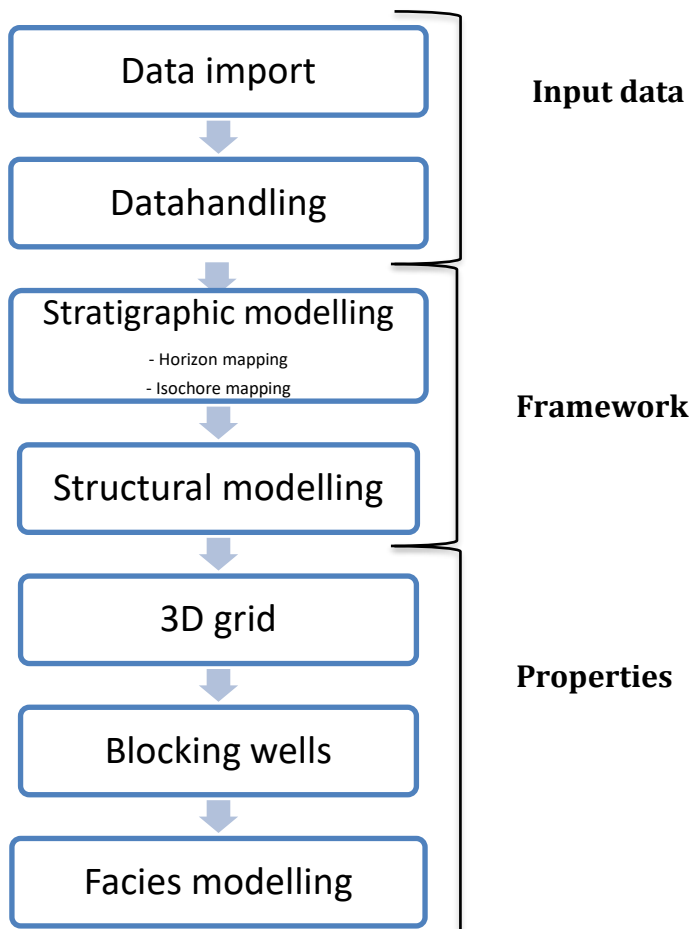
Figure 6.1.1: Schematic illustration of the reservoir modelling workflow. The modelling procedure can be subdivided into three main elements: Input data, involving import and processing of input data. Framework, generating a structural framework based on horizon, isochors and faults, and generation of a 3D modelling grid. Properties step involves blocking of wells and facies modelling (Modified from Howell, Martinius and Good (2014)).

6. Geological modelling

6.2 Project setup

The model uses a global WGS84 datum with UTM projection coordinates. Input data using other reference systems were transformed to UTM format prior to import. All measures are metric. It should be pointed out that the version of RMS used here employs a negative notation for altitude above sea level; this should be kept in mind when inspecting the digital model. In the text tables and figures we state these numbers as positive in order to avoid confusion.

6.3 Input data

Table 6.3.1 provides an overview of the data sets imported into RMS and used in modelling process, as well as their source, file type and import format.

Overview of input data and the zone divisions are illustrated in Figure 6.3.1. The zone division follows the facies association division.

Table 6.3.1: Input data used in the model

	Type of data:	From:	File type:	Imported as:
Project boundary	Points	Google Earth Pro	Txt file	Roxar text
Horizons	Points	Lime	Asc	Roxar text
Digital elevation model	Points	VOG	xyz file	Roxar text
Fault	Points	Google Earth Pro	xyz file	Roxar text
Well	MD, x,y,z, TVD	Petrel	Dev	Petrel well
Facies in log	MD and facies type	Petrel	Las file	Las

6. Geological modelling

Figure 6.3.1: Overview of the zonation of the model. The interpreted horizons from Lime correspond to the transition of the zones. Each zone represents a facies association, but is named zone number for simplification.

Label	Zone	Thickness Min	Thickness Max	Facies association labels	Grid type	Number of cell layers
c_Top_FA5	11	7.75	24.50	C_FA5	Proportional	62
c_Top_FA4	10	13	45.00	C_FA4	Proportional	225
c_Top_FA3	9	0.75	4.00	C_FA3	Proportional	40
c_Top_FA2	8	0.24	11.00	C_FA2	Proportional	100
c_Top_FA1	7	0.00	4.00	C_FA1	Proportional	17
Top_Entrada	6	5.91	8.46	e_FA2_1	Proportional	18
e_Top_FA3_1	5	2.54	2.96	e_FA3_1	Proportional	6
e_Top_FA2_1	4	3.08	5.62	e_FA1_1	Proportional	12
e_Top_FA2_2	3	9	10	e_FA2_2	Proportional	26
e_Top_FA3_3	2	2.76	9.64	e_FA3_3	Proportional	21
e_Top_FA4	1	5.92	3.34	e_FA4	Proportional	5
e_Top_FA2_3				e_FA2_3		

6. Geological modelling

6.4 RMS import

6.4.1 Key surfaces from Lime

The stratigraphic contacts mapped on the Lidar images in Lime (Chapter 5) are lines in a 3D space and serve as input to generate the horizons forming key part of the structural framework. Apart from the key J-3 unconformity, representing the boundary between the Entrada sandstone and Curtis Formation, the lines mainly represent mapped transitions between facies associations within these units. Figure 6.3.1 give an overview of the set up used in this project.

Table 6.4.1: Imported key surfaces

Interpreted lines from Lime:	Formation:
c_Top_FA3	Curtis Formation
c_Top_FA2	Curtis Formation
c_Top_FA1	Curtis Formation
Top_Entrada	J-3 unconformity
e_Top_FA3_1	Entrada sandstone
e_Top_FA1_1	Entrada sandstone
e_Top_FA2_2	Entrada sandstone
e_Top_FA3_3	Entrada sandstone
e_Top_FA_4	Entrada sandstone
e_Top_FA2_3	Entrada sandstone

Each stratigraphic contacts mapped on the Lidar images is stored as a collection of interpreted segments (separate files) in a dedicated folder. For example, the top Entrada folder in Lime contains 15 separate files. These are exported from Lime as ASC files, containing XY coordinates and altitude (z). The files are imported into the clipboard folder in RMS using roxar text format option (Table 6.4.1). Individual files (segments) belonging to the same stratigraphic contact are subsequently merged in RMS using the "append" functionality. This creates a point dataset for each stratigraphic contact. The points are represented by positive values. In order to match the data to the RMS model format employing a negative notation above sea level, the point values are transformed to negative values using a scalar function ($Z = -Z$). The spatial distribution of the point dataset is illustrated in map view in Figure 6.4.1, showing the points linked to the J-3 unconformity.
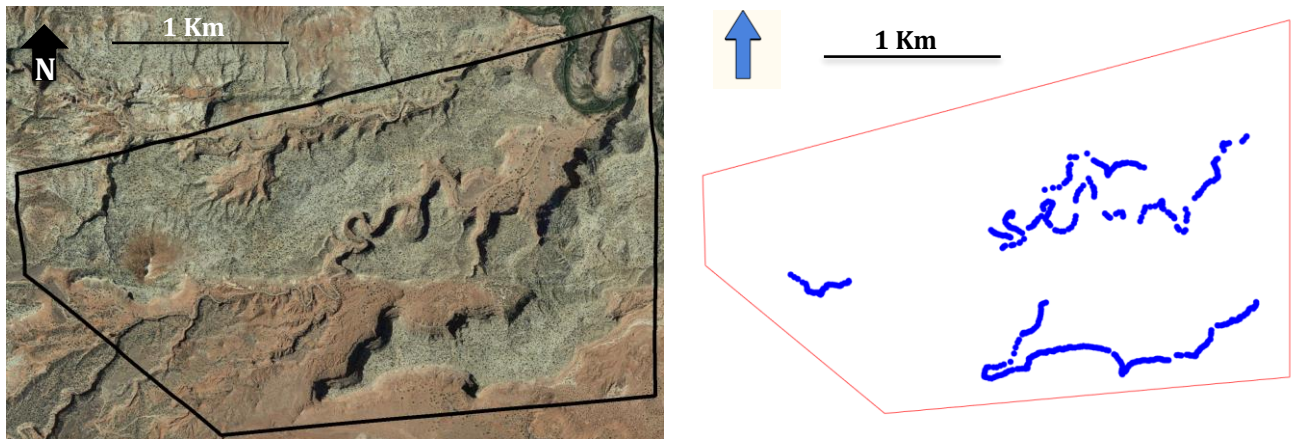
6. Geological modelling

Figure 6.4.1: Blue points represent the imported points from J-3 unconformity separating the Entrada sandstone and the Curtis Formation. The red polygon represents the project boundary**.**

6.4.2 Digital elevation model (DEM)

A DEM with a 9x9 m resolution over the study area was downloaded from USGS site (https://viewer.nationalmap.gov/viewer/). The dataset, consisting of xyz points in UTM coordinates was imported as a roxar text-format file into RMS. The horizon mapping tool was used to create a topographic surface from the points. In order to perform horizon mapping, the DEM is incorporated into the stratigraphic framework and later transferred to clipboard, as this is not a part of the stratigraphic framework.

In order to enhance resolution of the DEM locally along the scanned outcrops, the DEM point dataset was merged with the points imported from Lime prior to creating the DEM surface. The horizon mapping of the DEM is laterally constrained by the project boundary. After testing several options, the xy resolution was set to 5 m. A smoothing factor is applied to remove artefacts. Iterations and filter width was set to 2 and filter weight was set to 0.36.

The DEM surface was textured using a downloaded image from Google Earth (Figure 6.4.2) and served as a spatial reference map of the model area when performing quality and consistency checks of the input data. The picture was downloaded with a 4800 x 3352 pixel resolution. Fitting the image to the topography required some manual adjustments in xy. The "visual" settings for the texturing can be found in Appendix C.
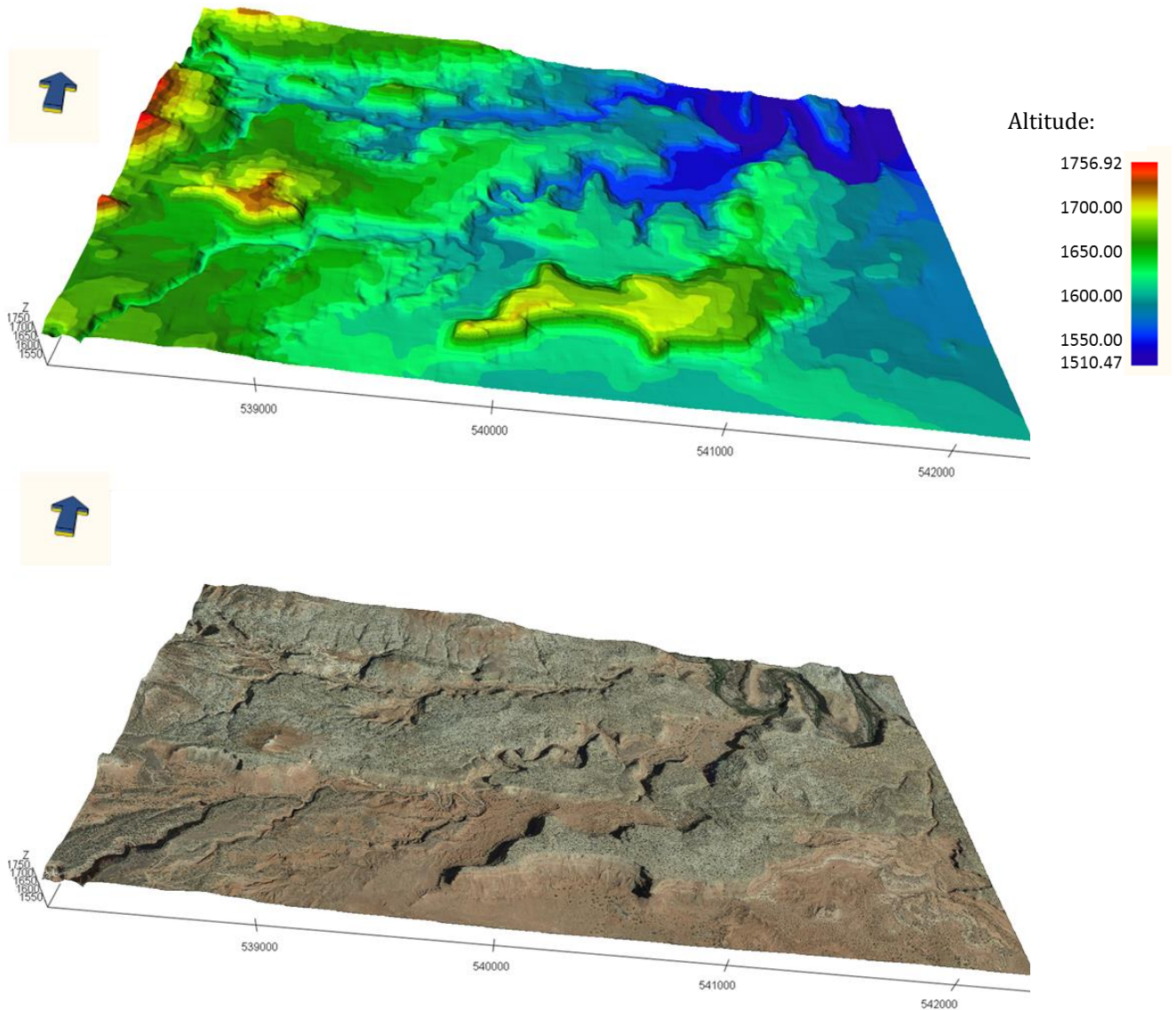
Figure 6.4.2: Illustration of the workflow in DEM modelling. A) DEM with 9x9 m resolution. B) DEM with texturing of Google Earth picture.

6.4.3 Log import

Conventional reservoir models normally employ log data from drilled wells, therefore the outcrop logs needed some adaption of datum and reference points in order to fit into the model. Rimkus (2016) digitized his logs as vertical tracks in Petrel. The logs contain information about the start position of the logs as well as facies distribution and thickness. First, the "wellhead" position and the trajectory of each log was imported as Petrel wells into RMS using the following set-up: MD reference was set to RKB, TVD reference was set to vertical datum (MSL) and "position is referenced from" is set to cartographic (UTM). For each outcrop log ("well"), the RKB elevation was set equal to the elevation at the top of the

log. The imported logs are given in MD where 0 MD represents the top of the log. The outcrop facies logs were imported as Las files, using the same reference setup as used for importing Petrel wells. In the log data tab, the facies log were linked to their respective well paths and set as discrete logs.

Importing horizon picks

Horizon picks ("Well picks") are xyz points were well-paths intersect specific horizons (see Table 6.4.1) used in the model. If the log is from a scanned section, the well picks are used to quality check the interpretation of the Lidar images. Well picks from logs outside the outcrops covered by Lidar images provides supplementary point data for horizon mapping. The well picks are exported from Petrel as a text file, containing information about the facies association transition in each log. The file was imported using Petrel well tops import under well picks. The well picks do not include the complete set of horizon picks found in the log and need to be altered. This was done based on the logs in Rimkus (2016) master thesis (see section 6.4.4).

6.4.4 Data handling

Project boundary

The project boundary was drawn as a polygon in Google Earth based on the extent of the available data. The point coordinates of the polygon was transferred manually to an empty clipboard point folder in RMS as xy coordinates and elevations (z). The folder was dragged to Cultural data > project boundary, and form the lateral outline of the model.

Terrain correction of Well/log trajectories in the Curtis Formation

In Rimkus (2016), the outcrop logs are rendered as vertical tracks positioned at the start of the log. In reality, the log follows a path along the slope of the outcrop, and the xy coordinates at the endpoint of the logged trace may differ significantly (>150m) from the starting point. In order to correct the logs (and the xy positions of the observations along them), lidar images and Google Earth were used to trace the most likely logging path. These corrected "well paths" were digitized in RMS and snapped to the DEM as illustrated in Figure 6.4.3. The logging path was reconstructed in RMS using the digital elevation model as a reference for altitude. First, a random point folder was made in clipboard and start and end point and the log trajectory were digitized on the DEM using point tool. The content of the point folder was

6. Geological modelling

then dragged into a line folder which automatically links the points to a continuous line. Finally, the "Transfer tool" was used to snap the lines to the digital elevation model.
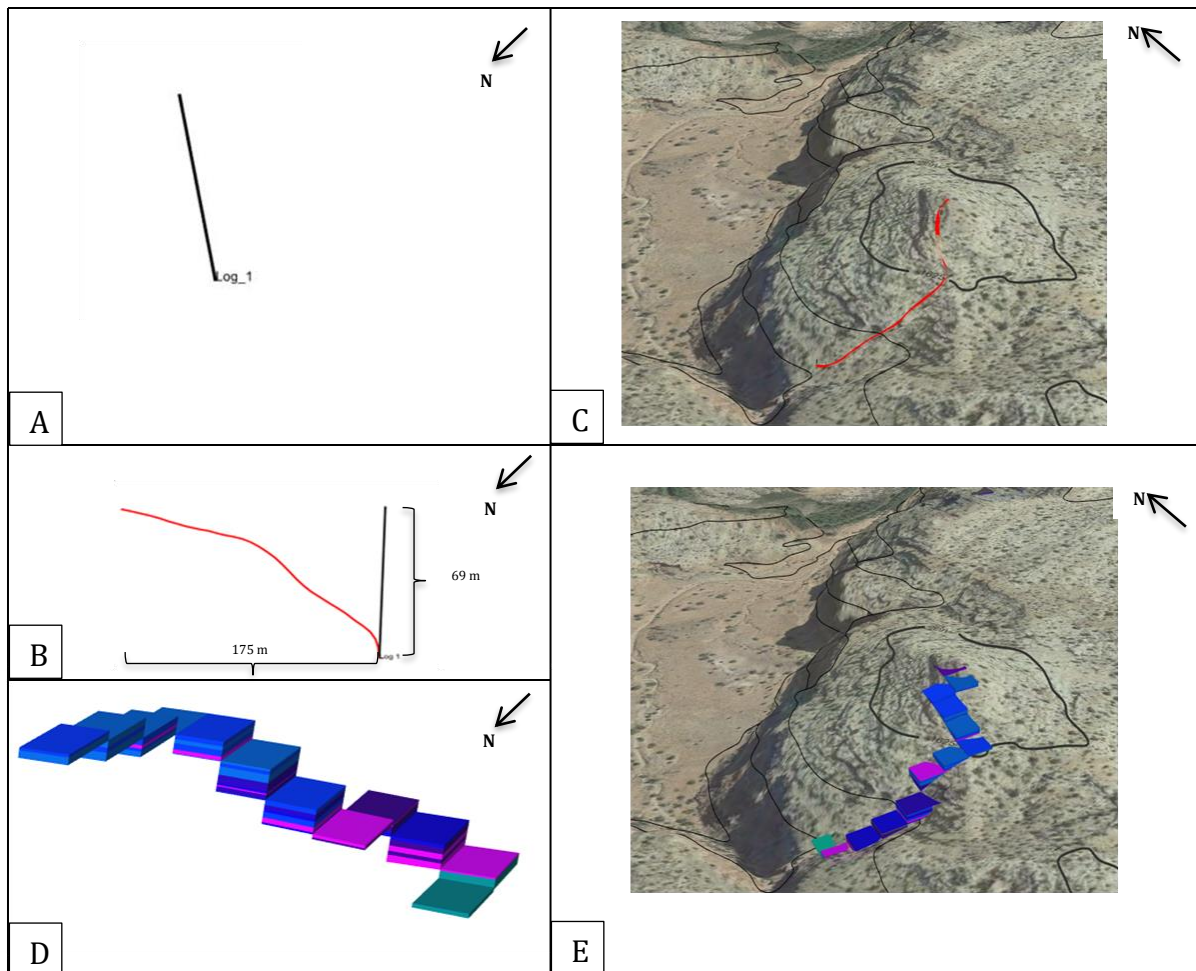
Figure 6.4.3: Workflow for creating a well trajectory. A) Vertical well with at the start point of the logging. B) Creating log trajectory (red line). C) Representing the log trajectory on the DEM. D) Blocking wells. E) The distribution of the blocking wells represented on the DEM.

The well trajectory from each locality was then copied to the associated initial log trajectory. Under the "survey instruments" tab, MD was set to 0. This automatically changes the start TVD to the start point of the log and this make the points to be represented in MD. The reason for this is that the logs were digitized as the logs end first, and then as MD downwards to the start of the logging.

For the logs to be represented correctly, their MD values had to be recalculated from their original values (MD measured from top and downwards) to MD values measured from top and down fitting the well trajectory. Each depth value for facies transitions in the discrete facies log was copied to a "well picks"- table to obtain the correct MD for each log. By

copying these depth values and cross checking that the elevation values are correct, ensures that the discrete facies are positioned correctly along the corrected well path. The well picks for this purpose is deleted and not used further.

Well picks

The horizon well picks (essentially representing the facies associations boundaries (Table 8) imported from Petrel did not match with the logs. An explanation for this is that the elevations of the logs are corrected, facies associations transitions modified and for some no logical explanation could be found for this. In order to make the input data consistent, some of the horizon picks were therefore adjusted manually after import, using the description of facies associations given by Rimkus (2016) to adjust the picks. The initial and adjusted picks are shown in Appendix A.4.

Digitizing the Entrada log

The log data from the Entrada sandstone were only available in paper format, and positional data was ambiguous (Gurrik, 2016). Digitalization for modelling had to be carried out from scratch. Logs and well picks were digitized manually based on the printed logs and information in Gurrik (2016). Precise coordinates of the logged sections were obtained by the author (Appendix A.1).

The Entrada logs are digitized as a vertical "wells". No adjustment to actual logging track along the outcrop was carried out as for the Curtis Formation. This is mainly due to the fact that the Entrada sandstone appeared to exhibit good lateral continuity of facies on a decimetre scale at the logged localities and that the outcrops are very steep. The coordinates of the logs and altitude for top and bottom of the log were specified. In "log properties", RKB elevation is set to equal the top of the log. Under the tab "Survey Interpolation", "Start MD, Ref. RKB" is set to 0 and TVD is set to the altitude at the top of the logs.

6. Geological modelling

6.5 Input to framework model

The stratigraphical framework describes the reservoir zonation in the model, as defined by the key horizons (6.4.1). It is generated based on the geological interpretation of the logs (well picks) and interpretation of Lidar outcrop images. Figure 6.3.1 displays the stratigraphical framework for this thesis. It includes the J-3 unconformity, separating the Curtis Formation from the underlying Entrada sandstone, and a number of stratigraphic contacts defined by transitions between facies associations that can be traced in the outcrops.

6.5.1 Horizon mapping

3D surfaces (horizons) are generated using the point sets imported from Lime and well picks as input. The lateral extent of the surfaces is constrained by the project boundary. The xy- grid increment of the surface is set to 25. A global B-spline algorithm is employed for the mapping, as it is well suited to handle unevenly distributed data. It is important that the algorithm chosen represents the reality of the distribution. The resulting stratigraphic surfaces are stored under the label "DepthSurface" in their respective horizon maps.

The input data is unevenly distributed in the model domain. Points extracted from the interpretation of Lidar images, provide very high resolution locally, whereas other parts of the model domain have few or no data points. Altitudes are interpolated, some with long distances between points, which can create severe errors. Although this issue is partly handled by the chosen surface gridding algorithm, the horizons, when displayed together, commonly intersect each other in areas where input data is lacking. This is an artefact, which can cause severe trouble during later stages of modelling and requires some corrective steps.

Note that the mapped horizons largely follow the subdivisions of the stratigraphy into facies associations, as the latter can be mapped throughout the area where outcrops are available and are believed to be largely continuous. However, it should be kept in mind that the thickness of the facies associations varies, and that some of the mapped contacts are erosional. Facies association two (c_FA2) in the Curtis Formation (representing zone number 9) is observed at all logged sites, but appears to pinch out towards log 7 (Rimkus, 2016). The base is an erosional contact cutting into the underlying zone, locally removing it entirely. As mentioned above, the "unguided" mapped horizon bounding these units crosses each other. This artefact

6. Geological modelling

is partly removed by manually editing away from the imported interpreted points. Points were digitized into the point folder of the associated horizon based on points from Top_Entrada and the thickness information from the facies associations (Appendix A.4).The horizon mapping was performed with the additional points representing the "DepthSurface". This ensures that the horizons always are stacked in the correct succession. A more detailed correction of stratigraphic thickness requires the use of isochores, see section 6.5.2.

Outside of the Lidar coverage, the altitudes of individual horizons are based on "well picks" from the outcrop logs and estimated isochores. The top of the Curtis Formation is truncated by the present topographic surface at Humbug Flats. In order to include the pre-erosion thickness of the Curtis Formation in the model, a horizon representing the transition between Curtis Formation and overlying Summerville Formation had to be included. The approximate pre-erosion position of this surface is estimated by copying the surface representing the base of the Curtis and transposing it upward. The transposition is controlled by the estimated average thickness of the Curtis Formation. Gilluly and Reeside (1928) state that the Curtis formation is 252 ft (76.8 m) thick at the northern end of the San Rafael Swell. This can be used as a minimum thickness estimate, as the northern edge of their map ends 16 km south of the study area. We here employ a thickness of 76.8 meter on the Curtis Formation in order to represent the Summerville Formation.

Surfaces representing Top Summerville and Top Carmel are preferred in later stages when modelling fault. Gilluly & Reeside (1928) state that the Entrada sandstone is 375 ft (114.3 m) thick. This thickness is used in generating the Top Carmel surface, using the same procedure as above. Summerville is estimated to be 128ft (39 m) thick the northern part of the swell. This thickness is used in generating the top Summerville surface. The same strategy is used to create the surfaces as for the top Curtis.

6.5.2 Isochore mapping

In areas with limited data coverage, the horizon extrapolation is uncertain and closely stacked stratigraphic surfaces commonly cross each other. Addition to supplying with extra point sets, (see section 6.5.1) which ensures consistent succession of stratigraphic surfaces in the model, the estimated vertical position of the surfaces can be further improved by using isochores. Isochores show the vertical thickness of stratigraphic intervals and can, if used together with anchoring points (such as altitude measurements from one or more contacts) provide a means

to generate a 3D stratigraphic framework. The generation of isochores here is a two-step process:

1. Thickness surfaces were created using the function "create isochore", which employs the consistent DepthSurface from the horizon mapping. The resulting isochores are written to the clipboard and subsequently, dragged into their respective places in the horizons folder as "isochore_Surface". The result from step 1 are used as input for the actual "isochore mapping" in step 2.
2. The mapping uses a global B spline algorithm. Minimum and maximum thickness values for each horizon are specified. Thickness input for the model set-up derived from thickness measurements in the logs together with thickness measurements in Lidar data, is listed in Appendix A.4. Mapping grid increment of 50 m was used. These isochores are used as input for structural horizon modelling.

The stratigraphical framework describes the reservoir zonation, between key surfaces (Figure 6.3.1) and boundary surfaces. It is generated based on the geological interpretation of the logs and Lidar data. Figure 6.3.1 displays the stratigraphical framework for this thesis.

6. Geological modelling
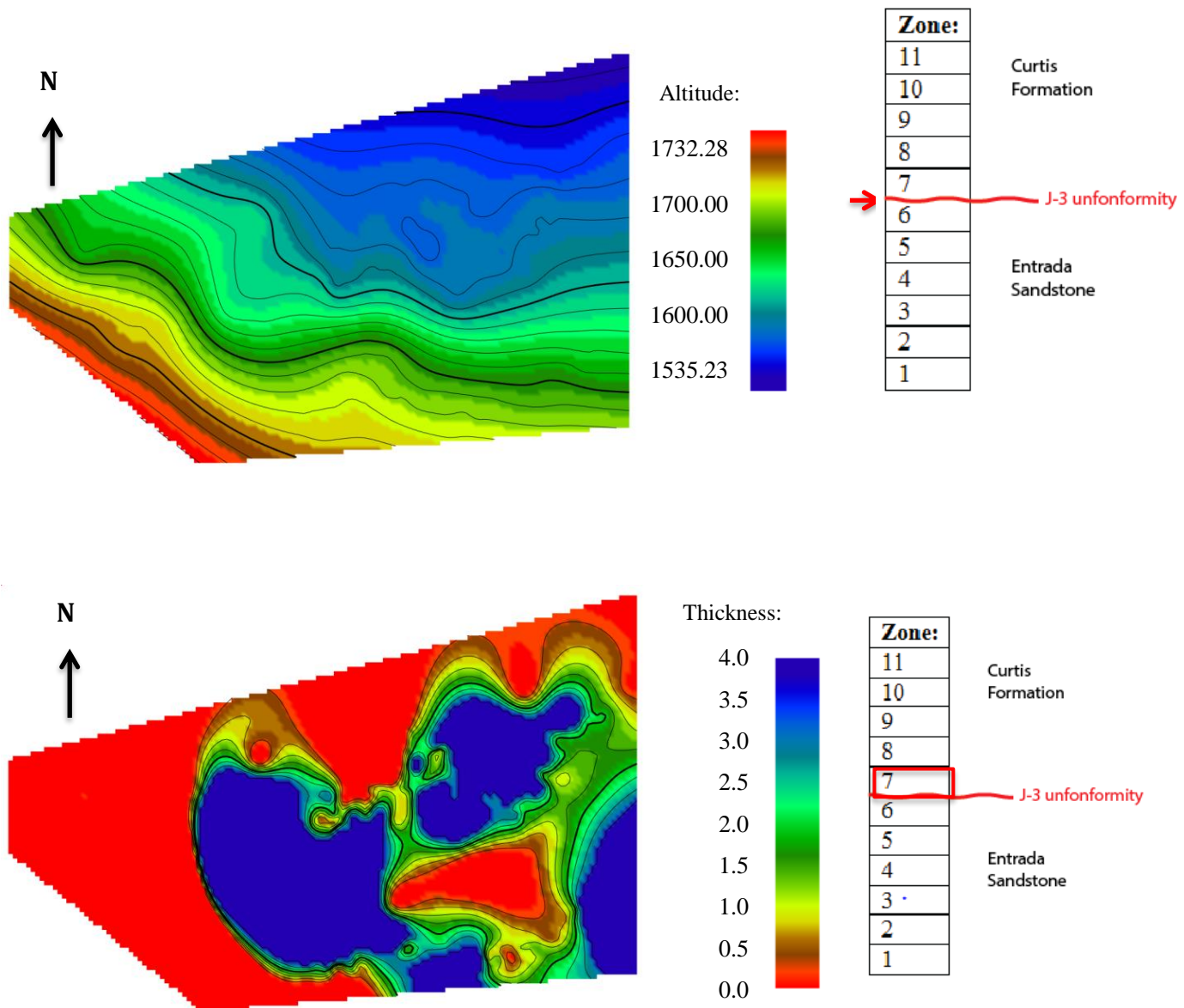
Figure 6.5.1: Illustrating the workflow for generating a isochore, describing the vertical thickness between two horizons. a) Horizon surface representing the J-3 unconfromity, B) Isochore with minimum and maximum values of zone 8 between the J-3 unconformity and c_Top_FA1. Where the red area is zero (red) there will be a communication between top Entrada and c_FA2 that might have reservoir quality. This will be further discussed in Chapter 7.3.Note that the pictures are represented with positive values, as in the field, for a better visualization.

6. Geological modelling

6.5.3 Fault
The model area is intersected by an east-west oriented normal fault which is clearly visible in the field and in Google Earth. The northern half of the model area is down-thrown by up to 50 m (Gurrik, 2016). The fault is shown on USGS maps of the area, but the fault line exhibits a mismatch with the actual fault trace seen in Google Earth and in the outcrops, and can therefore not be used. Instead the fault line was traced using the DEM with a Google Earth image texture (see chapter 6.4.2). The interpreted fault trace points were copied to "faults input" data main fault under DepthPoints. Additional points were traced in field May 2017 and these coordinates were added to the DepthPoints (Figure 6.5.2).
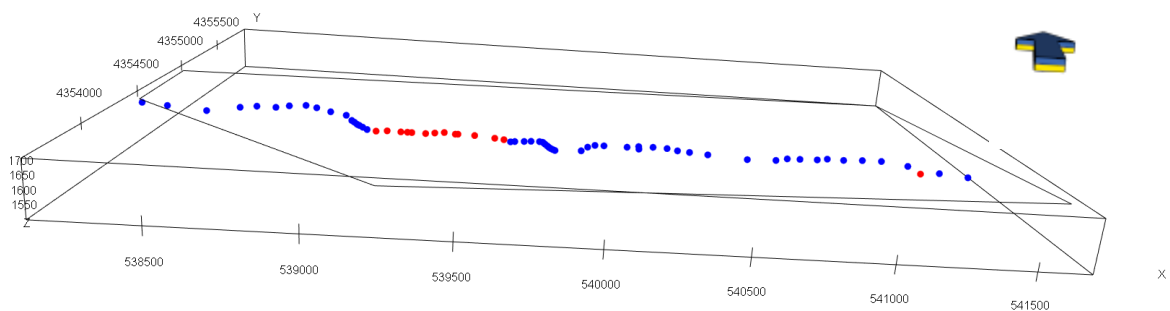
Figure 6.5.2: Red points represent the points collected in field May 2017 and blue points estimated from Google Earth Pro.

The modelling procedure is listed below:
1. Auto generated network under fault model. A network representing an area and a line intersecting the fault is generated based on DepthPoints.
   o The network is projected onto the DEM horizon.
   o The area is modified manually to represent the study area by aligning the fault network to the study area boundary.
2. Use Fault modelling tool under "fault model".
   o This creates a fault surface and fault lines. Fault lines are created for the horizons representing the intersection of horizons with the fault surface
   o The fault is defined a normal fault.
   o Under fault surface tab the top and base surfaces are estimated from horizon data, Top Summerville and Top Carmel respectively, with a 200m offset. This defines the vertical extent of the fault surface.
   o The dip is set to range between 58 and 63. Values have been estimated by Gurrik (2016).

6. Geological modelling

- o Surface grid increment is 5 and smoothness is set to low. The extent of the fault is set to top and base that is Top Summerville and Top Carmel.
- o For estimating fault lines, extrapolation distance is set 50 and influence distance 100.
- o Displacement is set to 37-42 (Gurrik 2016) and extrapolation surface is made for each horizon. The created fault surface is copied to fault input data. Output fault surface is located in the Fault_model bin and then copied to fault input data.

6. Geological modelling

6.6 Framework of the model

The model box boundary is first defined. This is performed by edit box and use project boundary to get the range from the object. Z-centre needs to be changed; based on max and min values from top Summerville and top Carmel.

- o Z-center: -1626.90
- o Z-length: 445.89

6.6.1 Fault modelling

Fault modelling under "integrated structural framework" is performed to include the fault in the framework model. The setup is described under:

- o Input data: DepthSurface (Soft data), DepthFaultSticks (soft data) and DepthPoints (Hard data). Correction range is set to 50 m.
- o Grid increment: 50 m
- o The dipAz is set to 260 and the dip (deg) is set to 71.
- o Shape of tip line is set as Convex hull and extension horizontally and vertical is set 100.
- o Output is a fault across the study area.

6.6.2 Creating the horizon model

Creating a horizon model is a one-step process, which generates a consistent stratigraphic framework and subdivision into zones using the horizons, isochors and the fault model as input. Each pair of horizon surfaces creates a zone between them and is labelled using the name of the upper horizon. Figure6.6.1 shows the selected horizons in the model, including data types as Well picks, DepthPoints defined as hard data for each input data type. Hard data is considered as accurate observations in a modelling context, while soft data are handled as approximation. Stratigraphic contacts are defined as conformities (depositional) or inconformities. An unconformity will truncate underlying horizons it intersects, whereas depositional (conform) contacts will truncate against any underlying horizon it intersects. Isochores are used as input in the horizon model to separate the horizons with the defined minimum and maximum value. The spacing between grid nodes (x, y increment) for each facies association is set to 50 m. The correction range that determines the influence distance of the hard data is set to 10 m. The fault (see section 6.6.1) is selected under the fault tab. "Constrain throw" is set to "force normal" (no constraint because the displacement is implicit

6. Geological modelling

from the data located on either side of the fault). The fault is expected to cut through the study area from Top Summerville to Top Carmel.
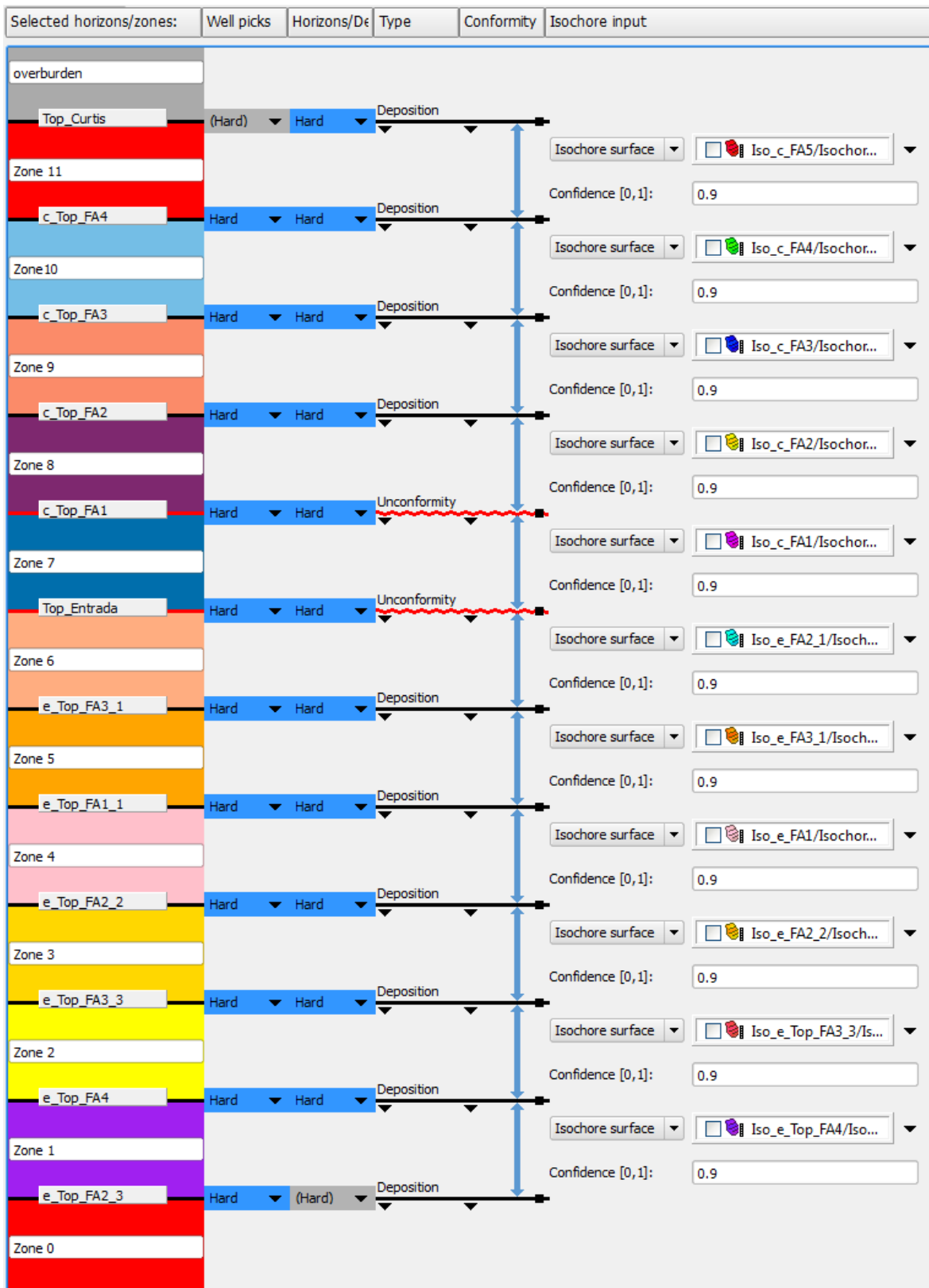

Figure 6.6.1: Display the horizons and the available input data used for each horizon as well as the conformity between the facies associations. Interpreted data and well picks are defined as hard data, as these data is not dependent on an extrapolation algorithm. Surfaces made from algorithm extrapolation are soft as these not definite represent the area.

6.7 Gridding

3D gridding involves subdividing the rock volume, into discrete volumetric units. The cells are populated with key properties such as facies type and petrophysical properties. The discretization simplifies the modelling process and fluid flow simulation, as the number of calculations required for running the model can be controlled by the number of cells in the model (i.e. fewer cells – lower CPU cost). Gridding has significant impact on the modelling and simulation. It should, be kept in mind that this need for speed should be balance by an understanding of what level of detail is required for the purpose of the model in order not to "average out" details that could influence the outcomes. The cell dimensions (x,y,z) define the resolution of the model, which should be adapted to the purpose of the model/ level of lithological heterogeneity. As a rule, the vertical resolution is determined based on the thickness of the smallest object one wants to capture in the model. The cell should be half of the mean thickness to the smallest object you want to model (Ringrose & Bentley, 2015).

Grid type, dimensions and truncations need to be specified. Since there is only one fault in the model, and it is fairly straight, an XY-regular grid is chosen for this model, which implies that all the cells have the same width and length. The fault pillars can be moved from their exact position for the cell to obtain as orthogonal cell angles as possible (ROXAR, 2017a). The grid should align along stratigraphic surfaces and define stratigraphic continuity (Deutsch, 2002). In this model the grid is also aligned with the fault to minimize distortions.

Figure 6.7.1 shows the options for vertical ordering of grids; proportional, top- and base conform grid. For the top conform and base conform grid type the cell thickness is constant and a reference surface is applied on the base or top of the structure and cell layers are built downwards or upwards from this surface. Proportional grid is a grid with a constant number of cell layers and varying cell thickness (ROXAR, 2017a). The choice of vertical structure of the grid can vary between different stratigraphic units in a model and is largely dependent on the interpreted depositional architecture of any given unit. In the present model, the link between depositional architecture and grid set up is made simple since the zonation in the model follows the stratigraphic architecture defined by the facies associations. Figure 6.7.3. provides an overview of grid resolution and vertical grid structuring used for each zone in the model.
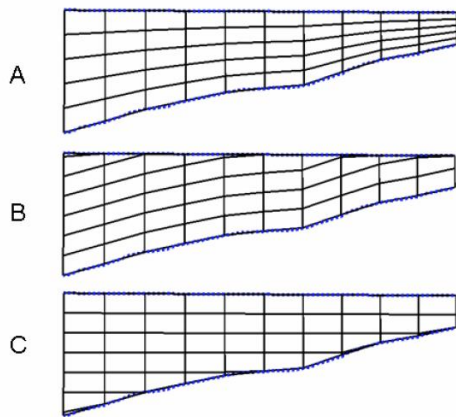
Figure 6.7.1: Type of gridding layers. A. Top Conform, B. Base conform. C. Proportional grid (ROXAR, 2017a).

6.7.1 Gridding – Entrada sandstone

Choice of vertical grid structure for the Entrada sandstone is mainly governed by depositional architecture. The deposits are massive to stratified and consist of sandstone and thinner centimetre-scaled mudstone and siltstone units. Based on the logs, a vertical resolution of 0.5 m is chosen for the Entrada sandstone.

The base of the Entrada (Top Carmel) is not exposed in the outcrop and this horizon is by transposing the top Entrada downwards (see section 6.5.1). The top of the Entrada is the J-3 unconformity which cuts into the underlying Entrada and creates a relief of a few metres filled in by the overlying Curtis Formation. Since the incision relief appears to be minor, this contact can either be captured by choosing a base conform grid or a proportional grid for the Entrada. Here a proportional grid structure is used in modelling the Entrada sandstone.

6.7.2 Gridding type – Curtis Formation

Facies association 1 (c_FA1) includes lenticular-bedded mudstone (facies G). As described in Chapter 5 the facies can be observed as a continuous stratum in the outcrop, except where locally eroded along the erosional base of the overlying c_FA2. For later flow simulation purposes facies association c_FA1 is crucial as it is likely to behave as a vertical flow barrier, except where punctured by erosion. Since the underlying J-3 unconformity is sub-horizontal and it is desired that the mudstone (c_FA1) is captured as horizontal beds a base conform grid can be chosen. Since the facies association (c_FA1) consist of low permeability and that the erosion in the unit is detected by zero thickness in the zone a proportional grid is applied.

6. Geological modelling

Facies association 2 (c_FA2) constitutes the heterolithic lower part of the Curtis Formation, observed incising into the Entrada sandstone and the overlying c_FA1. When gridding the facies it is important to keep in mind the heterogeneity and connectivity of the reservoir. The base of c_FA2 is cut into the underlying facies, but the sediments overlying it reflect infilling postdating incision. For all zones in Curtis Formation a proportional grid was chosen, mainly because contacts appear conform and show no clear evidence of localized incisions.

6.7.3 Creating the grid

A regularized grid is made by using the fault model (section 6.6.1) and horizon model (section 6.6.2) as input. The project boundary is used as a polygon for the gridding. Note that the reservoir zonation follows the stratigraphy defined by the facies associations and the units between them named zone numbers (Figure 6.3.1).

In determining the number of layers the information about the facies thickness within each facies associations were considered for the Curtis Formation (see Appendix B.2). For the Entrada sandstone it was used a 0.5 m resolution.

Grid resolution is dependent on heterogeneity dimensions one wants to capture in the model. It is important to implement thin continuous heterogeneities in the model. The grid dimensions are set to 20 m increment in xy direction. Figure 6.7.2 displays the different grids for each zone of the facies associations together with the grid type and dimensions. To align the grid with the fault the rotation is set to 357.50 degrees. The total amount of cells is 13 991 068. And the total number of cell layers is 532.

6. Geological modelling
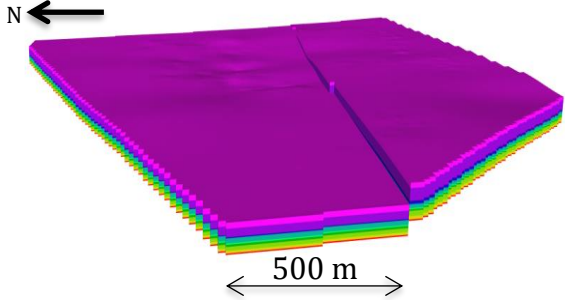
	Zone: 11
	FACIES ASSOCIATION: **c_FA5**
	Gridding type: Proportional
	Thickness:
	  • Min: 7.75 m
	  • Max: 24.50 m
	  • Mean: 11.94
	Number of cell layers: 62

	Zone: 10
	FACIES ASSOCIATION: c_FA4
	Gridding type: Proportional
	Thickness:
	  • Min: 23 m
	  • Max: 45 m
	  • Mean: 30.88
	Number of cell layers: 225

	Zone: 9
	FACIES ASSOCIATION: c_FA3
	Gridding type: Proportional
	Thickness:
	  • Min: 0.38 m
	  • Max: 4 m
	  • Mean: 2.47 m
	Number of cell layers: 40

	Zone: 8
	FACIES ASSOCIATION: c_FA2
	Gridding type: Proportional
	Thickness:
	  • Min: 0.20 m
	  • Max: 10.98 m
	  • Mean: 4.25 m
	Number of cell layers: 100

	Zone: 7
	FACIES ASSOCIATION:c_FA1
	Gridding type: Proportional
	Thickness:
	  • Min: 0 m
	  • Max: 4.00 m
	  • Mean: 1.81
	Number of cell layers: 17

Figure 6.7.2a: Illustrate the different grids used for each zone of the facies associations for the Curtis Formation.

6. Geological modelling

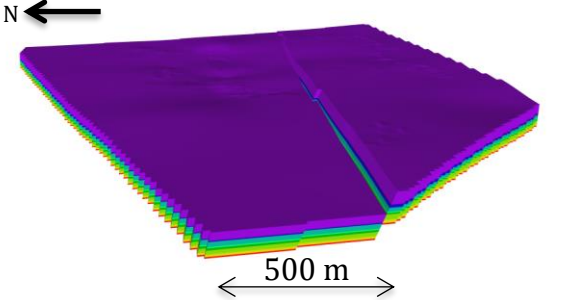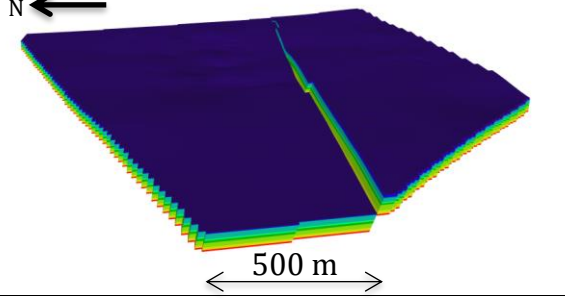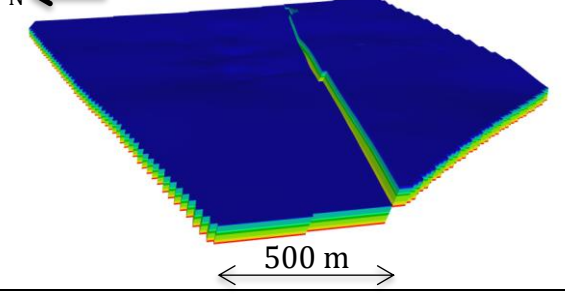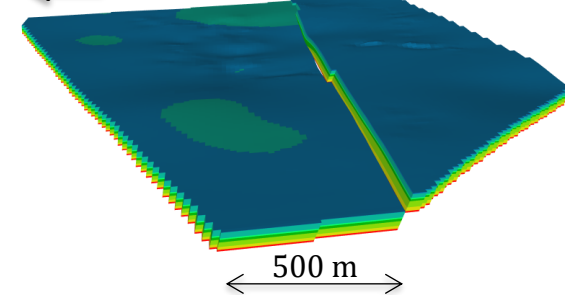|	
N ← 500 m	**Zone: 6** **FACIES ASSOCIATION:** c_FA2_1 Gridding type: Proportional Thickness: • Min: 5.91 m • Max: 8.73 m • Mean: 7.38 m Number of cell layers: 18
N ← 500 m	**Zone: 5** **FACIES ASSOCIATION:** c_FA3_1 Gridding type: Proportional Thickness: • Min: 2.46 m • Max: 2.98 m • Mean: 2.64 m Number of cell layers: 6
N ← 500 m	**Zone: 4** **FACIES ASSOCIATION** : c_FA1_1 Gridding type: Proportional Thickness: • Min: 3.08 m • Max: 5.61 m • Mean: 5.11 m Grid Number of cell layers: 12
N ← 500 m	**Zone: 3** **FACIES ASSOCIATION:** c_FA2_2 Gridding type: Proportional Thickness: • Min: 8.5 m • Max: 13 m • Mean:10.75 m Number of cell layers: 26
N ← 500 m	**Zone: 2** **FACIES ASSOCIATION:**c_FA3_3 Gridding type: Proportional Thickness: • Min: 12 m • Max: 10.5 m • Mean: 8.5 m Number of cell layers: 21
N ← 500 m	**Zone: 1** **FACIES ASSOCIATION:**e_FA4 Gridding type: Proportional Thickness: • Min: 2 m • Max: 2.5 m • Mean: 2.25 m Number of cell layers: 5

Figure 6.7.2b: Illustrate the different grids used for each zone of the facies associations for the Curtis Formation.

6. Geological modelling

Grid control:

Quality control on the gridding was performed to detect any flaws in the grid, such as collapsed and twisted cells that could influence later flow simulation. This procedure is handled automatically by the software and results are rendered both as 3D visualization and statistics. The QC also works as a consistency check for the entire geometric structure of the model. Ideally the number of irregularities, such as abnormal cells, should be zero, but sometimes the geometry of either fault or stratigraphic architecture make the occurrence of such features unavoidable, in which case efforts should be made to keep them at a minimum by modulating the input to the gridding.

Collapsed cells are cells that contain cells where two or more corners in the same cell are identical (0-thickness).

Gridding control revealed that there are collapsed cells in zone 8 (c_FA2) and zone 7 (c_FA1); this is related to the incising nature of the overlaying c_FA2. The deformed cells are concentrated around the incisions where c_FA1 pinch out to zero thickness.

These cells are concentrated towards the incision. Collapsed cells are cells that contain cells where two or more corners in the same cell are identical. Optimal it is preferred a minimum of collapsed cells.

6.8 Blocking wells

Blocking of wells involves assigning a value to each cell along the well/log path. Blocking entails upscaling the log to the resolution of the modelling grid (see section 6.7). Quality control of the blocking shows that the blocked wells match the original data well. This is performed by using well log editor/calculator in order to compare original (left display) and blocked log profiles (right display) Figure 6.8.1.
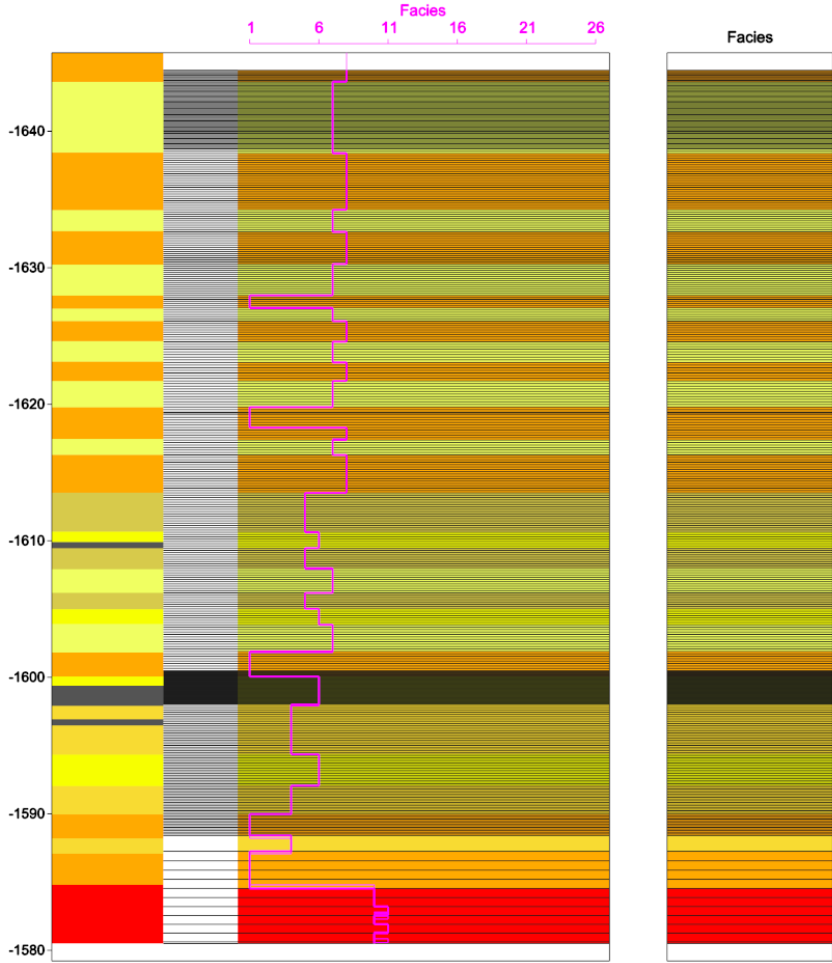

Figure 6.8.1: Method for quality controlling the blocked wells in well log editor. This shows log 1.

6. Geological modelling

6.9 Facies modelling

The facies model is based on the interpreted sedimentary logs by Rimkus (2016) and Gurrik (2016) and their spatial reconstruction of the depositional environment. Facies modelling require discretization of the log data (blocking of wells) in order to adapt the log data to the chosen grid scale. Rendering the facies observed along the logs as 3D architectures furthermore requires quantification of geometry, dimensions and orientations of individual facies as well as information about how they interact with other facies. Some information supplied by Rimkus (2016) and Gurrik (2016), providing conceptual models of the facies architecture of the Curtis Formation and the Entrada sandstone. These provide key guidelines for the modelling conducted here, but do not provide a comprehensive set of input information for the modelling; consequently a number of choices regarding the model set-up had to be made by the modeller; these choices are documented here as far as possible to enable the modelling process to be tracked and facilitate quality check. It should be kept in mind that the model set-up, including the subjectively made choices, can substantially influence the geo-statistics of the resulting 3D model (Caers, 2005).

Both pixel- and object based methods have here been applied to construct the facies model. Pixel based facies modelling is based on the use of variograms (Caers, 2005). It is well suited for capturing gradual transitions and interfingering between facies, and where it is hard to define a specific geometry or body shape of a given facies, such as in shallow marine and tidal settings. Variograms describe the relationship between a pair of data points x and y, and the geological distance between the pairs (Ringrose & Bentley, 2015). Spatial distribution, size, shape data, directional trends and net-to-gross are used as input for facies modelling. The range, correlation length, of the variogram can vary in different directions, reflecting how a given facies interacts with adjacent facies laterally and vertically.

Object based facies modelling allows for geological geometries and relative spatial distribution to be reproduced by dropping objects directly onto the reservoir grid such as they fit the outcrop. This modelling type is used in the cases where facies geometry can be described by a set object shapes and dimensions, and where knowledge and sufficient data about the spatial distribution of the facies and properties is available (Caers, 2005). This method works well provided shape, and dimensions of the facies are known (Roxar, 2017b). The facies model is conditioned to the information regarding facies type and position

6. Geological modelling

provided by the logs, but will produce multiple outcomes (realizations) based on the constraints defined in the model set-up. The spread of outcomes will reflect the uncertainty of the model. If more precise information is fed in as input, the spread of outcome will narrow, capturing the reduction in uncertainty.

The Entrada sandstone and Curtis Formation have been handled in different ways, as will be outlined below.

6.9.1 Facies modelling: Entrada sandstone

Facies modelling of the Entrada sandstone is based on the two logs (Figure 4.1.1) collected by Gurrik (2016). The log and facies were digitized in RMS, (see Appendix A.2 for the digitized log). The input data is scarce and localized.

The facies architecture of the wet eolian depositional setting of the Entrada sandstone is governed by groundwater fluctuation in the area, these fluctuations are likely controlled by changes in base level, but could also be caused by periodic flooding of the interdune areas (Figure 6.9.1). The wet eolian dune setting implies that the interdune flats are within the capillary fringe, due to high groundwater table. Current ripples and wavy bedding in the interdune sediments may possibly reflect local shallow water bodies. In the study area, the Entrada exhibits vertical repetition of co-sets of medium to large-scale sets of cross-strata and thinner, essentially horizontal deposits. In the field and on the Lidar images, the Entrada sandstone exhibits laterally extensive and continuous beds with only minor variations in thickness.
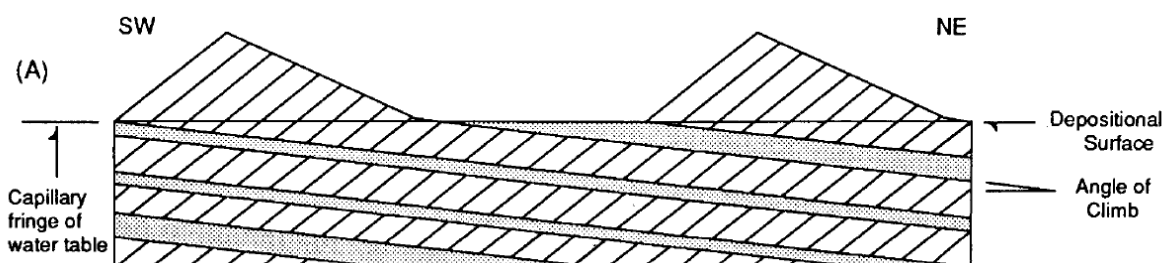

Figure 6.9.1: Wet eolian dune architecture (Kocurek, 1981).

6. Geological modelling

The eolian dunes in the Entrada sandstone reflect depositional directions from the north east (45°). According to Kocurek (1981) the Entrada erg propagated north-westward while the Sundance Sea retreated towards the North-East.

The lateral continuity of the strata observed in the Entrada sandstone, in combination with scarce log data advocate the use of a simple model concept framed around a general understanding of the depositional setting. The model concept for the Entrada sandstone involves the use of facies indicator simulation, using with varying set ups for the individual facies associations as shown in Table 6.9.1. This is a pixel based modelling technique that uses variograms to fill in the space between and outside of the data points. Variogram settings for the individual facies associations were subjectively defined based on the overall description of the Entrada depositional environment.

Input values for the variograms are listed in table 6.9.1. A more detailed description of the modelling and variogram settings of the individual facies associations; wet interdune deposits (FA1), wet eolian dune (FA2) and floodplain deposits (FA3) is given below. The massive to stratified sandstone, facies e_A is modelled as "background" throughout the Entrada sandstone.

The variogram is based on information from the literature. The logged thickness of the dunes can to some extent indicate the lateral extension and width of the dunes. Thickness information from the logs and Lidar scans (Appendix B.1) is used to determine the dune thickness of dune beds "after erosion/burial/compaction". Kocurek (1981) reconstructed ancient ergs of the Entrada sandstone based upon observations from modern environments, fieldwork and hypothesis.

Entrada facies association 1 (e_FA1): Wet interdune deposits:
Thick siltstone units interbedded with thinner beds of clay-, mud-, and sandstone. The beds of the interdune deposits are approximately 1 m thick (Appendix B.1). The "downwind" length of the interdune area is approximately 400 m and width is estimated to about 1500 m. This geometry of the intedune sediments conforms to a dune pattern with length axes at approximately right angles to the prevailing wind direction (Kocurek, 1981).

6. Geological modelling

Entrada facies association 2 (e_FA2): Wet eolian dune

Wet eolian dunes consist of fine to medium sandstone interbedded with thin cm-scaled mudstone and siltstone. The dunes can be traced continuously over the study area and display large, up to 5 m thick, cross-stratificated beds (Appendix B.1). Kocurek (1981) estimated the dimensions of the dunes to be approximately 1200 m long downwind, and about 2000 m perpendicular to the wind direction. The estimated height of the dunes during deposition is estimated to be 100 m, based on comparison with dune dimensions as stated by Romain and Mountney (2014). Two wet eolian dune deposits have been modelled (e_FA2_1 and e_FA2_2). They are modelled with the same variogram settings and will therefore almost get the same result. Figure 6.9.2 display modelled floodplain deposits of e_FA2_1.

Entrada facies association 3 (e_FA3): Floodplain deposits:

Floodplain deposits consist of sand-, mud-, silt and claystone. The deposits can be traced continuously throughout the outcrop and are believed to represent complete inundation of the study area by flooding.

Wet interdune deposit:
Modelling algorithm: Indicators
Grid resolution: 20 x 20
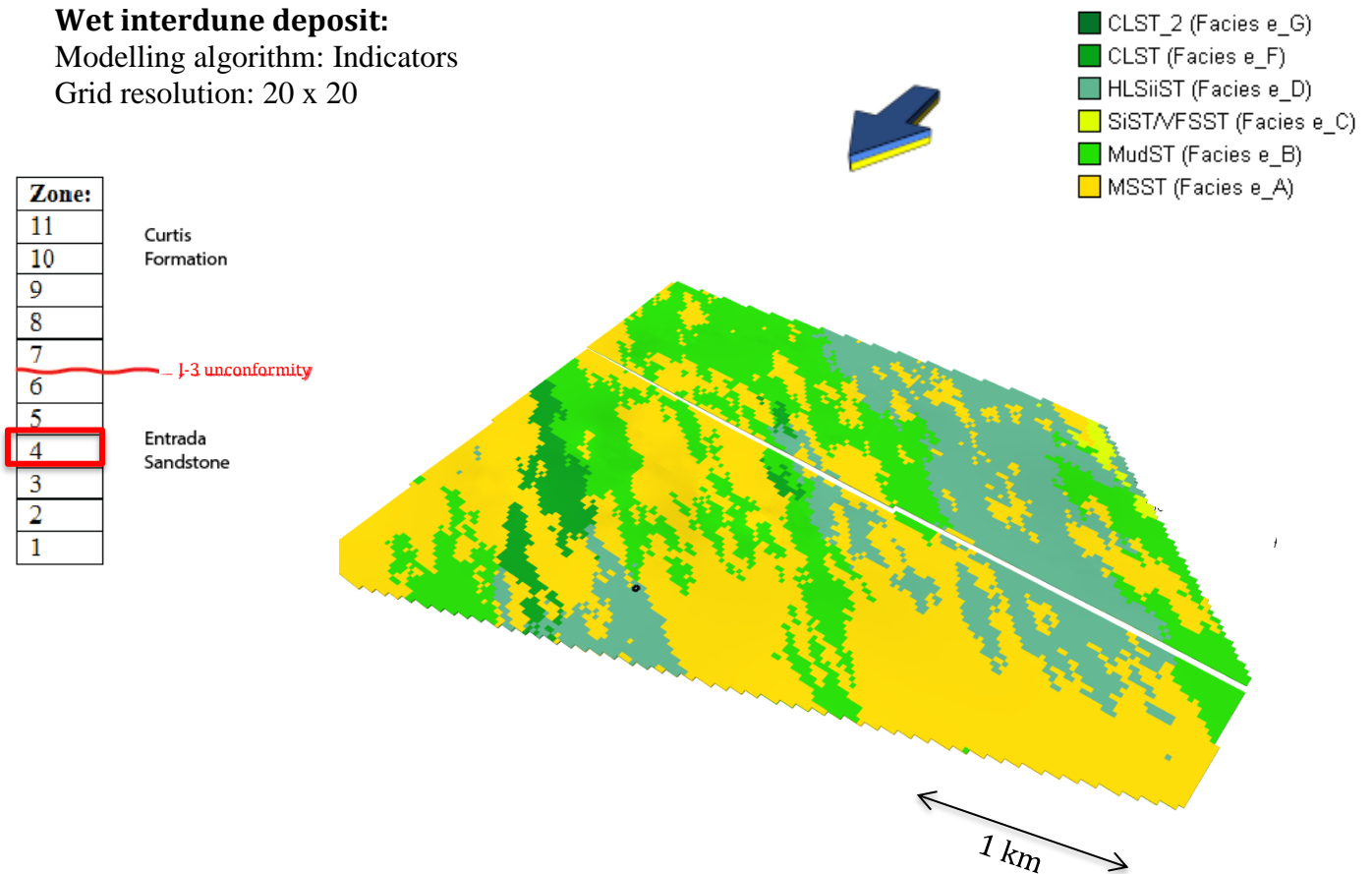
Figure 6.9.2: Modelled interdune deposits of e_FA1_1. Input data is found in table 6.9.1.

6. Geological modelling

Wet eolian dune:
Modelling algorithm: Indicators
Grid resolution: 20 x 20 m
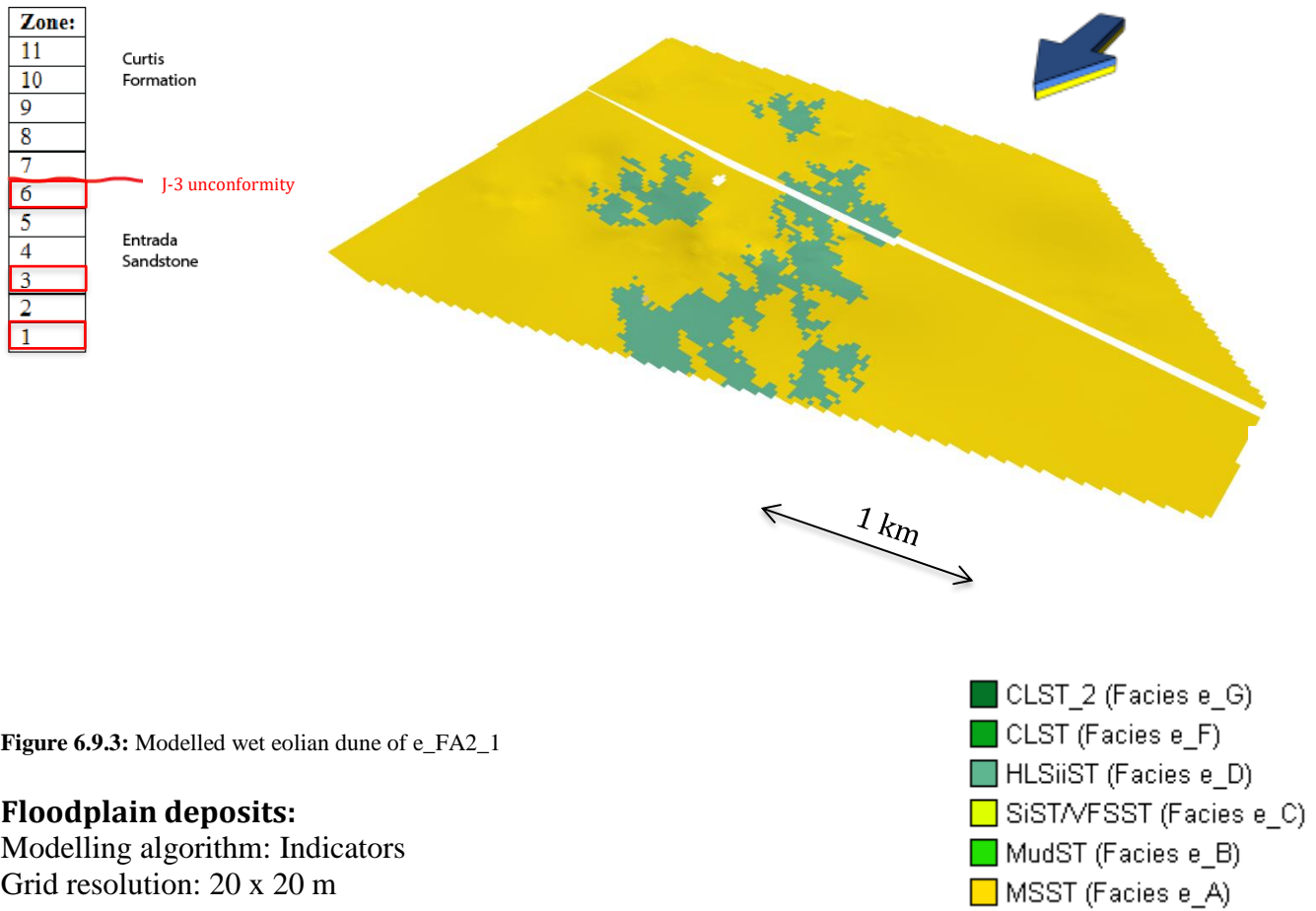
Figure 6.9.3: Modelled wet eolian dune of e_FA2_1

Floodplain deposits:
Modelling algorithm: Indicators
Grid resolution: 20 x 20 m
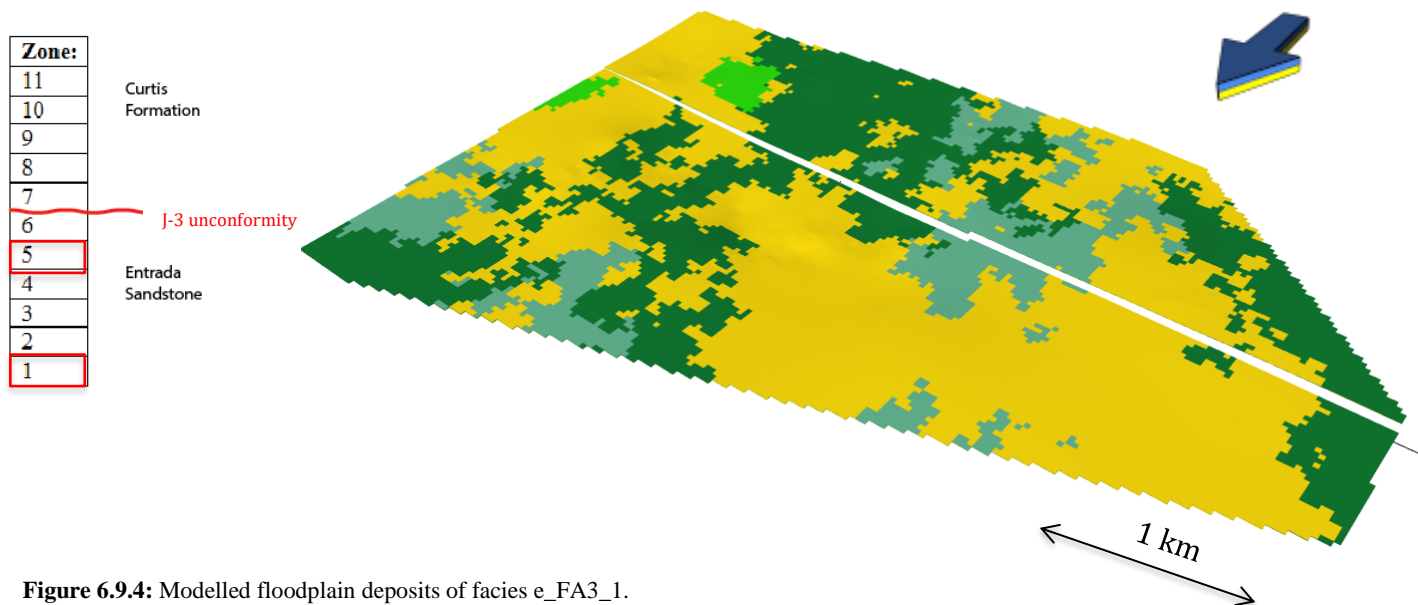
Figure 6.9.4: Modelled floodplain deposits of facies e_FA3_1.

6. Geological modelling

Table 6.9.1: Input values for modelling facies of the Entrada Sandstone. The anisotropy within the facies is indicated by the different values in parallel, normal and vertical direction. The Earth is more continuous parallel and normal than in vertical direction.

	Involved facies:	Conceptual description:	Variogram settings:		
			Parallel to azimuth:	Normal to azimuth:	Vertical:
e_Top_FA2_1					
	e_A	Background			
	e_D	Simulate facies	1200	2000	10
e_Top_FA3_1					
	e_A	Background			
	e_B	Simulate facies	1000	1000	10
	e_D	Simulate facies	1000	1000	10
	e_G	Simulate facies	1000	1000	10
e_Top_FA1_1					
	e_A	Background			
	e_B	Simulate facies	400	1500	10
	e_C	Simulate facies	400	1500	10
	e_D	Simulate facies	400	1500	10
	e_F	Simulate facies	400	1500	10
e_Top_FA2_2					
	e_A	Background			
	e_B	Simulate facies	1200	2000	10
	e_D	Simulate facies	1200	2000	10
e_Top_FA3_3					
	e_A	Background			
	e_B	Simulate facies	1000	1000	10
	e_C	Simulate facies	1000	1000	10
	e_G	Simulate facies	1000	1000	10
e_Top_FA4 (Fremont bed)					
	e_A	Background			
	e_F	Simulate facies	1000	1000	10

6. Geological modelling

6.9.2 Facies modelling: Curtis Formation
The facies model of the Curtis Formation is largely based on the interpretation and paleo-depositional reconstruction provided by Rimkus (2016). A total of seven facies were identified in the Curtis Formation; lenticular-bedded mudstone (c_G), major tidal channel deposits (c_H), subtidal sand bars (c_E), tidal channel deposits (c_D), estuary passive infill (e_F), tidal sand flat (c_C) and tidal mud flat deposits (c_A and c_B). In the model, the subdivision into zones follows the facies associations. Thus each zone (and facies association) can be set up separately. Both pixel and object based modelling have both been used.

Depositional, the Curtis Formation can be subdivided into a lower, middle and upper part. The facies are deposited in a tide-dominated estuary. The lower part (c_FA1-c_FA3) was deposited in a tidally influenced, shelf to subtidal environment; the middle part (c_FA4) in a subtidal to lowermost intertidal setting and the upper part (c_FA5) in an upper intertidal environment. Overall, the Curtis exhibits an upward shallowing succession reflecting a coastal progradation.

The general setting of the area during deposition is interpreted as a wide, tidally estuary (Rimkus, 2016). Figure 6.9.2 shows an idealized diagram of how tidal energy varies in a system of this kind. The energy increases into the estuary and towards the tidal limit, where the energy decreases (Dalrymple, Mackay, Ichaso, & Choi, 2012). Grain size decreases as the tidal energy increases, but the suspended-sediment concentration increases (Figure 6.9.2c).

The lowermost part of the Curtis Formation consists of lenticular mudstone, deposited in tidally influenced shelf environment (c_FA1). The top of c_FA1 is truncated by an erosional unconformity and incision of channels, reflecting a higher energy environment, possibly caused by a drop in base level. The channels are filled with conglomeratic dunes (facies c_D) and tidal bars (facies c_F). Mudstone layers are observed between the dunes and represent episodes of lower energy. The facies are deposited below the mean low-tide level, in subtidal environment. Tidal bars develop in the outer parts of estuaries (Desjardins, Buatois, & Mangano, 2012). Lateral accretion of tidal bars over channels interbedded with lenticular mudstone (FA3) is observed lateral in the study area.

The middle part of the Curtis Formation (FA4) represents subtidal to lowermost intertidal deposits. The facies shows a cleaning upward trend that can be explained by a higher wave

6. Geological modelling

and tidal energy environment (Figure 6.9.5), which tends to winnow out fines. Dunes and sand bars are found where tide and wave energy are strongest.

Progradation of tidal flats indicate a decrease in energy in intermediate intertidal environment and an overall shallowing driven by deposition. Tidal flats generally exhibit heterolithic deposits reflecting varying current strengths as tides inundate the flats. The flats are commonly cut by tidal channels representing localized erosion during high tide.
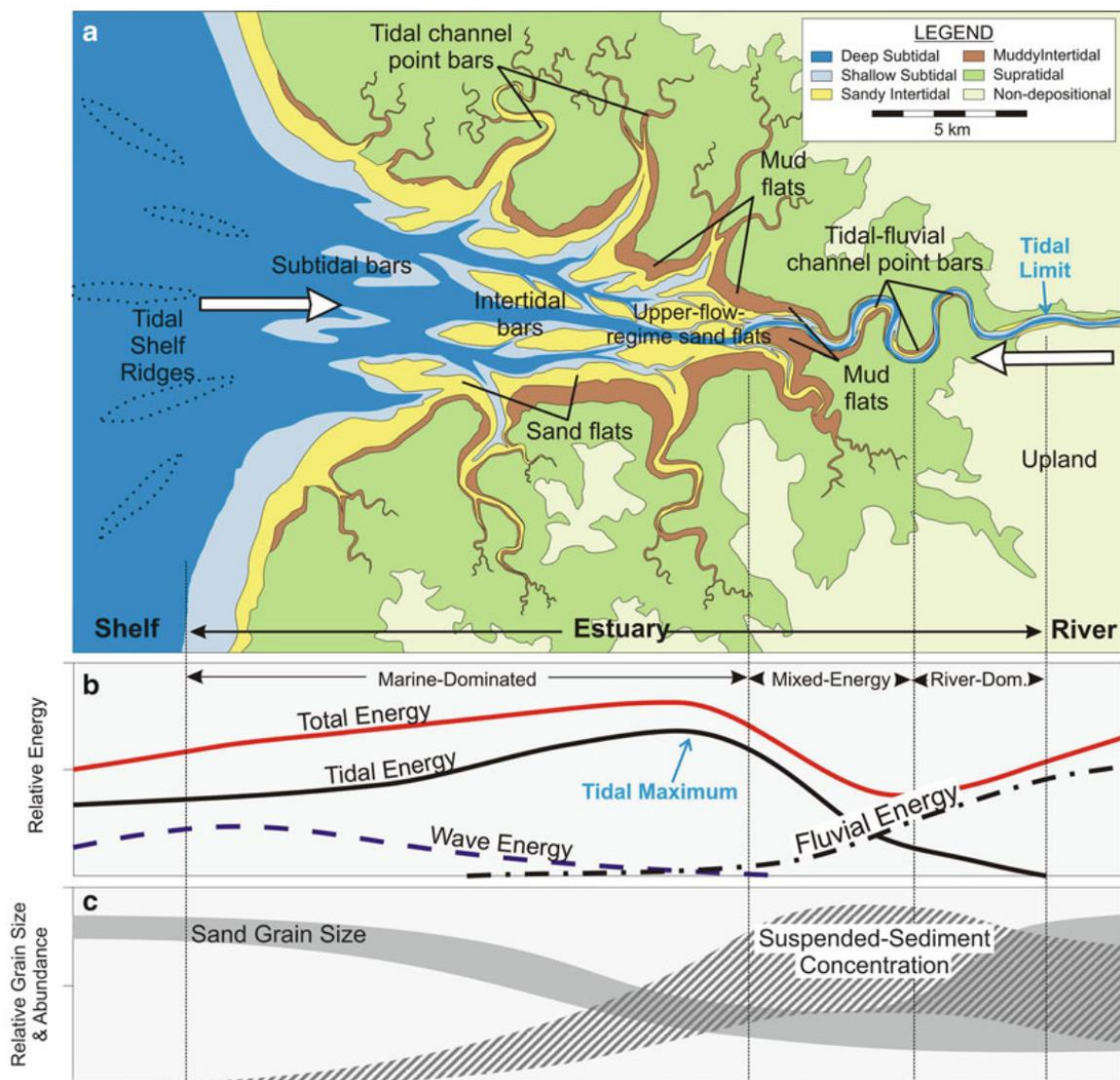

Figure 6.9.5: (a) Map shows distribution of channel and sub environments in a tide-dominated estuary. (b) Wave, tidal and river energy distribution in the system. (c) Distribution of grain size (Dalrymple et al., 2012).

6. Geological modelling

Paleocurrent measurements of the lower (c_FA1-c-FA3) and middle part (c_FA4) show a range in directions and strongest in NE-SW of the tidal channel deposits. It is sometimes difficult to establish depositional directions for tidal deposits, as current direction can vary a lot in the system. Here we take the position of the Sundance Sea to the NE as a general guideline for orienting the model of the Curtis Formation.

Below, the geometry of the different facies that were modelled using object modelling is presented first, before specifying the different modelling techniques used for the facies associations. Table 6.9.3 shows the input data used in RMS. Volume fractions and thickness values are from Rimkus (2016) logs, statistics are found in Appendix B.

6.9.2.1 (Major) tidal channel deposits

Major tidal channel deposits (facies H) and tidal channel deposits (facies D) are modelled as sinuous fluvial channels. The channel facies as observed in the logs, range in thickness from 25 cm to 4.31 m (Appendix B.1). Paleocurrent measurements show a range of directions, but with a predominance of NE-SW orientations (Rimkus, 2016). Tidal channel sand bodies are lens-shaped in cross-section with a flat upper surface and concave lower surface. The channels are conceived as crossing over the entire modelled area. This may be a simplification, as some channels could well terminate in out model area, but this could not be verified. Furthermore there is no dedicated tool in the software to capture the geometry of channels on tidal flats (i.e. tapering meandering geometries with frequent branching at right angles to the main channel), so the use of a model algorithm designed to capture fluvial geometries should in any case be regarded as an approximation.

Width: The conglomeratic dunes are seen to pinch out in the order of 10s to 100s of meters. The smallest beds are thought to pinch out over a smaller distance than larger beds. The facies association can consist of either a single bed or stacked beds of dunes. Reynolds (2016) states that the thickness – width ratio is found to be within a 1:100 and 1:1000 ratio for channels. Thickness measurements (ranging from 25 cm to 4.31 m) in c_FA2 correspond to a width ranging between 400 and 1500 m. This width measurement is similar to the correlation in Lime (Chapter 4).

Sinuosity and amplitude: There is little research on tidal channel sinuosity, and therefore modern examples by using Google Earth, has used to estimate the sinuosity of some

representative modern tidal channel systems of comparable dimensions as those that were observed in our study area. The area Barnstable, USA exhibit tidal channels that are measured using Google Earth. For the major tidal channel deposits of c_FA2 a sinuosity of 1.39 and an amplitude of 2500± 500 m was employed. For the smaller tidal channels (width about 500 m) associated with c_FA4b a higher sinosity (1.42) and smaller amplitude (1000 m) was chosen.

6.9.2.2 Subtidal sand bars

Facies c_E is observed within facies associations c_FA3 and FA4. The subtidal sand bars are elongated, laterally extensive bodies inside the channels. They are observed in log 1 and 2 within FA2. Subtidal sand bars can be traced in c_FA3 throughout the study area. It is difficult to establish the distribution of facies c_E in c_FA4, as it was not possible to constrain the lateral extent of the facies from the Lidar images. Width and lateral extent of the sand bars are determined by using analogues. Sand bars in estuaries are more elongated, but have similar length-width ratio as river bars (Leuven, Kleinhans, Weisscher, & van der Vegt, 2016). Bar length is dependent on flow velocity and tidal excursion length. The subtidal sand bar dimensions depends on the location in the succession. The subtidal sand bar dimensions are calculated for each of the facies associations based on thickness information from the logs (Appendix B.3).

Leuven et al., (2016) stated a width-to depth ratio: [Equation 2]

$$H = 2.27W^{0.2}$$

And width to length ratio: [Equation 3]

$$L = 6.9W$$

H = Height, W = Width, L = Length

6. Geological modelling

c_FA1:Channel modelling

A 1.75 m point bar succession (c_I) is observed in log 8. A composite modelling approach is used. Input parameters are given in Table 6.9.3. Volume fraction of the channel is set to 0.1 ± 0.005 based on thickness measurement of log 8.

FA1:
Modelling algorithm: Channel modelling
Grid resolution: 20 x 20 m
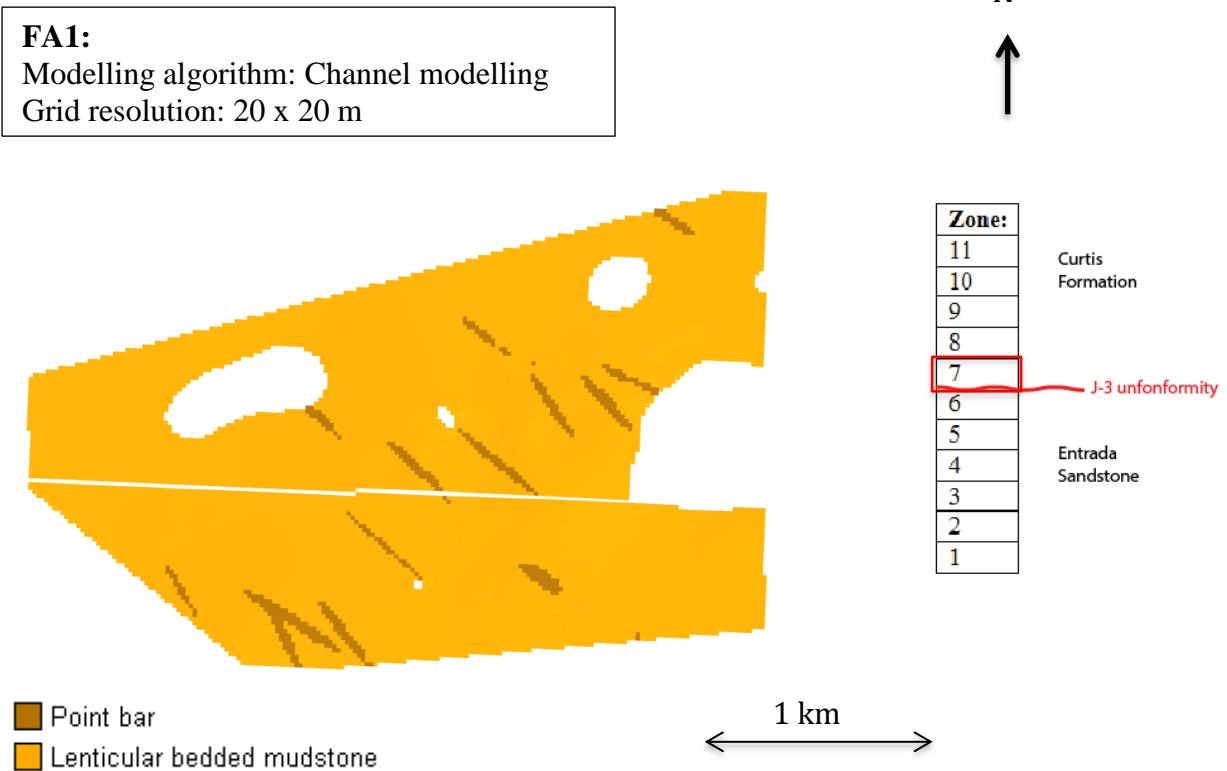
Figure 6.9.6: Modelling of facies (C_I) as point bar and heterolithic mud-rich facies c_G as background.

c_FA2: Channel modelling

Channel modelling of c_FA2 includes major tidal channel deposits (facies c_H), lenticular bedded mudstone (c_G) and subtidal sand bars (c_E). Lenticular bedded mudstone is modelled as background, while major tidal channel deposits and subtidal sand bars are modelled as objects, with geometry inputs (Table 6.9.3).

6. Geological modelling
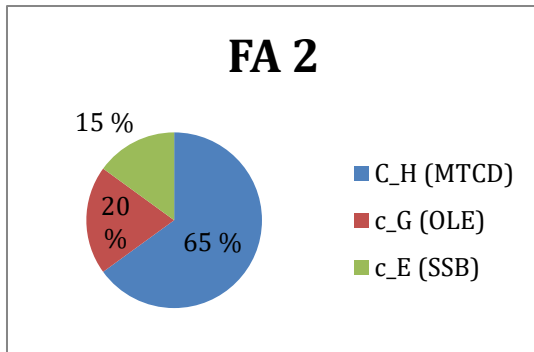
Figure 6.9.7: Volume fraction of major tidal channel (MTCD), lenticular bedded mudstone (OLE) and subtidal sandbars (SSB) within Curtis facies association 2 (FA2). The percentages are based on the facies thickness from the measured logs.

"Sand body" mode is chosen to represent the channel system and subtidal sand bar are modelled as channels crevasses. Volume fraction of the channels, crevasse and background is specified (Figure 6.9.7). The channel system volume fraction is set to 0.65 with a 0.005 tolerance. The crevasse volume fraction is set to 0.15 with a 0.02 tolerance. These values correspond to the volume fractions given in Figure 6.9.3. Under the geometry tab, thickness and width values is specified for the channel. Amplitude is set to 2500 ± 400 m and sinuosity is set to 1.46, based on the above description of tidal channels (section 6.9.2.1). Geometry of crevasse is specified under the "Crevasse/barrier" tab. Crevasse are modelled as "isolated". Minimum number of crevasse-belts per channel is subjectively set to 4.

Figure 6.9.8 illustrate the model with the input data. The channel shapes are recognized in the model, but lack 90 degrees channels. Subtidal sand bars are interpreted as elongated extensive bodies inside of channels (Rimkus, 2016). There is not a module for modelling this in RMS, but as we observed for the model it is possible to use crevasses as these are tied to the channels and they fill areas where the channel meanders.

FA2:
Modelling algorithm: Channel modelling
Grid resolution: 20 x 20 m
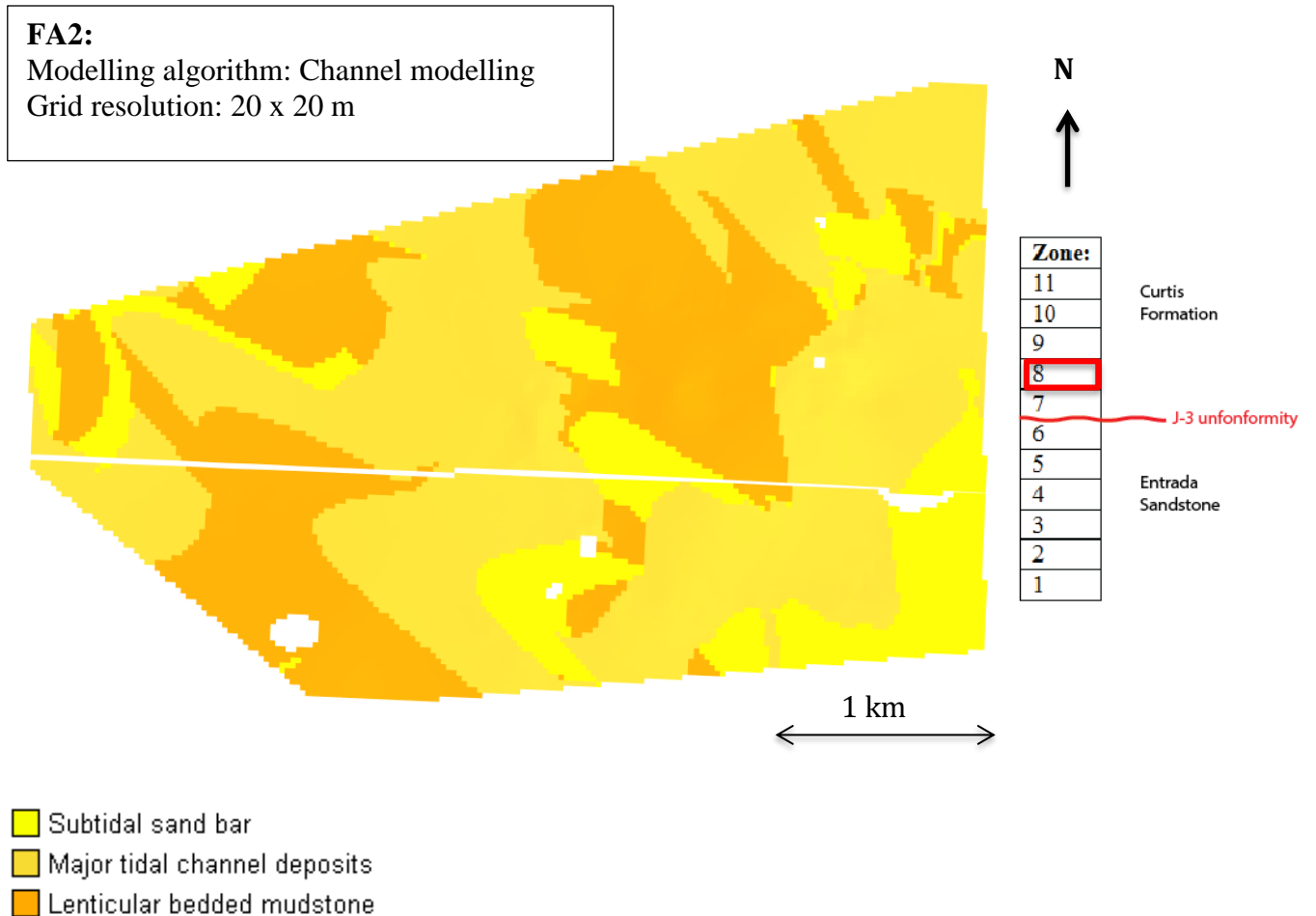
Figure 6.9.8: Facies H consisting of conglomeratic dunes interfinger with subtidal bars (Facies E).

c_FA3: Facies composite

Subtidal sand bars can be traced in c_FA3 throughout the study area. Lenticular bedded mudstone (facies G) is used as background facies in the modelling. The volume fraction is based on thickness measurements and the value for subtidal sand bar is set to 68% with a 0.01 tolerance. The subtidal sandbar is ellipsoid shaped. Dimensions are listed in Table 6.9.3. The height of the subtidal sand bar is given in Table 6.9.3 and the truncation distribution is set to the min and max thickness values (Appendix B.3). Based on Wood (2004) the width value is set to 850 ± 100 m and the length is set to 5865 ± 100 m (see section 6.9.2.2).

Figure 6.9.9 shows the modelling of subtidal sand bars embedded in lenticular mudstone. The subtidal sand bars are observed elongated downstream as would be expected in such reservoirs.

6. Geological modelling

FA3:
Modelling algorithm: Facies composite
Grid resolution: 20 x 20 m
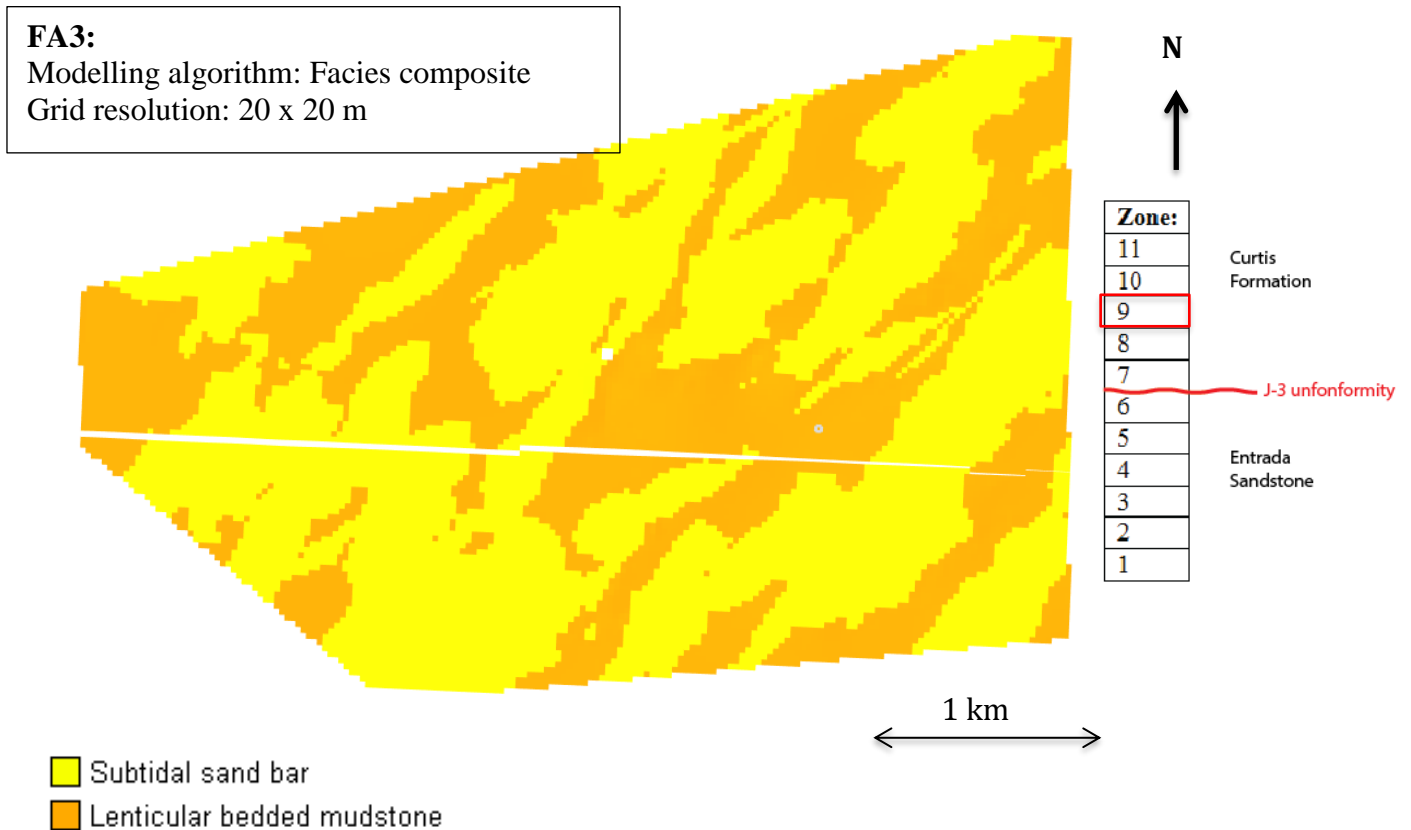
Figure 6.9.9: Subtidal sand bars modelled interbedded with lenticular bedded mudstone as background. The elongated subtidal sandbars are elongated downstream.

c_FA4: Belts, channel and composite

Lack of coverage makes it difficult to trace and map the facies of c_FA4 on the Lidar images, but it is observed in all of the logs in the Curtis Formation. c_FA4 consist of a network of sandy tidal channels and subtidal sand bars deposits embedded in heterolithic rich sediments. The heterolithic deposits consist of both sub-tidal deposits and intertidal deposits, and the channels are mainly linked to intertidal and subtidal sand bars to sub-intertidal. The modelling is therefore divided into two: FA4a and FA4b (Table 6.9.2.1)

Table 6.9.2.1: Facies association 4 (c_FA4) can be divided into two models, based on interpreted depositional environment

FA4a: Sub-intertidal		
	c_F	Tidal sand flat (TSF_2)
	c_E	Subtidal sand bar (SSB)
FA4b: Intertidal		
	c_C	Tidal sand flat (TSF_1)
	c_D	Tidal channel deposits (TCD)

6. Geological modelling

Belts modelling (truncated Gaussian simulation) was employed to model the transition from tidal sand flat of sub-intertidal (facies c_F) background to tidal sand flat of intertidal (facies c_C) background. Belts modelling approach was used to separate facies c_F (Facies 5) from facies c_C (Facies 8) as these facies appear at different levels of the facies associations (Table 6.9.2.2).

Table 6.9.2.2:

Facies:	Facies abbreviations:	Facies number in RMS	Interpretation	Facies association
c_F	TSF_2	5	Sub- intertidal	c_FA4a
c_C	TSF_1	8	Beach with tidal inlets	c_FA4b

The belt algorithm gives a trend output report. Calculator is used in order to get the values:

FA4_Belts_Report_Parameter_1=FA4_Belts

IF FA4_Belts_Report_Parameter_1 = 5 THEN FA4_Belts_Report_Parameter_1 =0.1 ENDIF

IF FA4_Belts_Report_Parameter_1 = 8 THEN FA4_Belts_Report_Parameter_1 =0.9 ENDIF

The resulting report parameter is subsequently used as a 3D conditioning parameter (placed under "seismic") to model the distribution of channels in the system.

FA4a consist of sand bars interbedded with tidal sand flat. A composite modelling approach is used and tidal sand flat (facies c_F) is used as background for the modelled object, subtidal sand bar (c_E). Volume fraction of tidal bar is set to 0.25 with a 0.01 tolerance, this is calculated from the available facies distributions in the logs. The bars are modelled as ellipsoid. Length and width values based on description in 6.9.2.2, and are stated in Table 6.9.3.

The FA4 belt model is merged with FA4a sand bar model. This is performed in order to represent the tidal sand bars in the model where only c_F (tidal sand flat in sub-intertidal environment).

N

FA4a:
Modelling algorithm: Composite modelling
Grid resolution: 20 x 20 m

Zone:	
11	Curtis
10	Formation
9	
8	
7	— J-3 unfonformity
6	
5	Entrada
4	Sandstone
3	
2	
1	

1 km

- Tidal sand flat (Very fine to fine sandstone)
- Subtidal sand bar
- Tidal sand flat (Wavy bedding)

Figure 6.9.10: Subtidal sand bar modelled in areas where TSF_2 (Tidal sand flat 2 (c_F)) is present. The remaining is modelled as tidal sand flat 1. Subtidal sand bars are mainly located in the lowermost part of the facies association 4 (zone 11).

The upper part of the facies association, FA4b, is modelled using facies channel. Tidal sand flat (facies c_C) is used as background of the tidal channel (facies c_D). Channel volume fraction is set as 0.28 with 0.2 tolerances. Thickness and width values are found in table 6.9.3. Amplitude is set to 1000 ± 400 m and sinuosity to 1.42. The report parameter from belt modelling is used as input under seismic. It is expected that the facies cover the study area, but lack of Lidar data and correlation between the logs makes it difficult to determine the length of the facies.
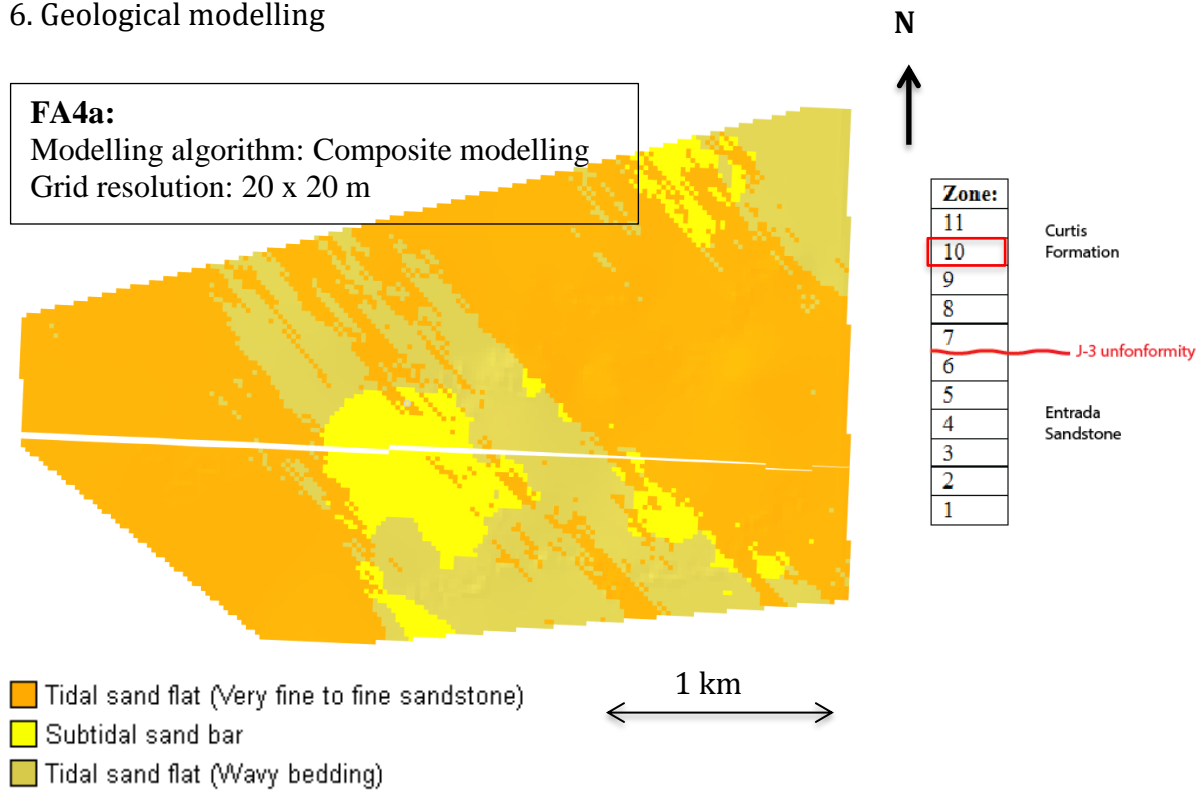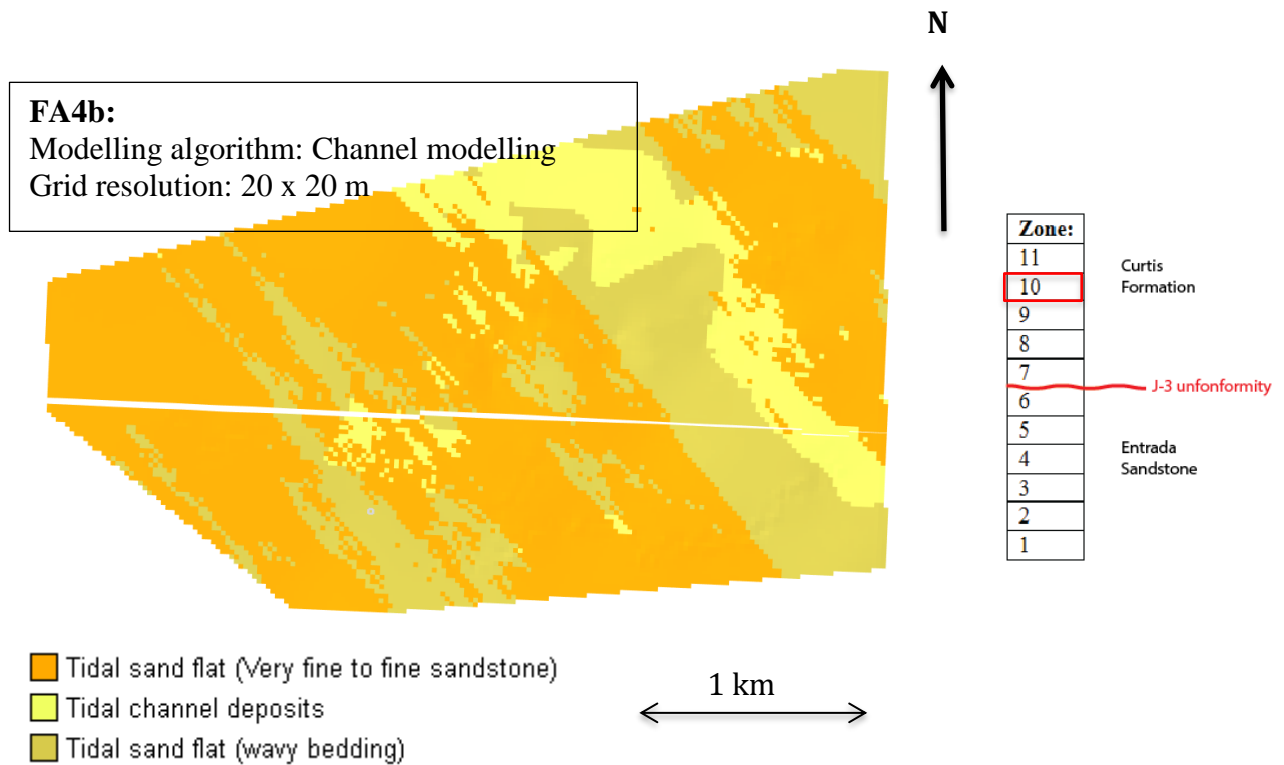
Figure 6.9.10: Tidal channel deposits modelled in areas where TSF_1 (Tidal sand flat 2 (c_C)) is present. The remaining is modelled as tidal sand flat 2. Subtidal sand bars are mainly located in the uppermost part of the facies association 4 (zone 11).

c_FA5: Indicator simulation

The Lidar scan does not cover outcrops with this facies association, but it is observed in log 1, 3, 4 7, 9 and 10 located above the scanned part of the outcrops. The facies association displays alternating lenticular-bedded mudstone and coarser grained tidal flat deposits. The deposits are interpreted to extend over the entire study area. No distinct facies bodies are identified, and facies indicator modelling approach is therefore used. The dominant facies is facies c_A and c_B is used as input for simulated facies and facies c_G is set to the background facies. The volume fraction under the "trend" tab is set to calculate from the well data. The deposits are envisaged to roughly line up with the shoreline believed to be located to the NE, and the azimuth is set to 45 degrees. Variograms are set to define the facies distribution as a function of distance in lateral and vertical direction.

6. Geological modelling
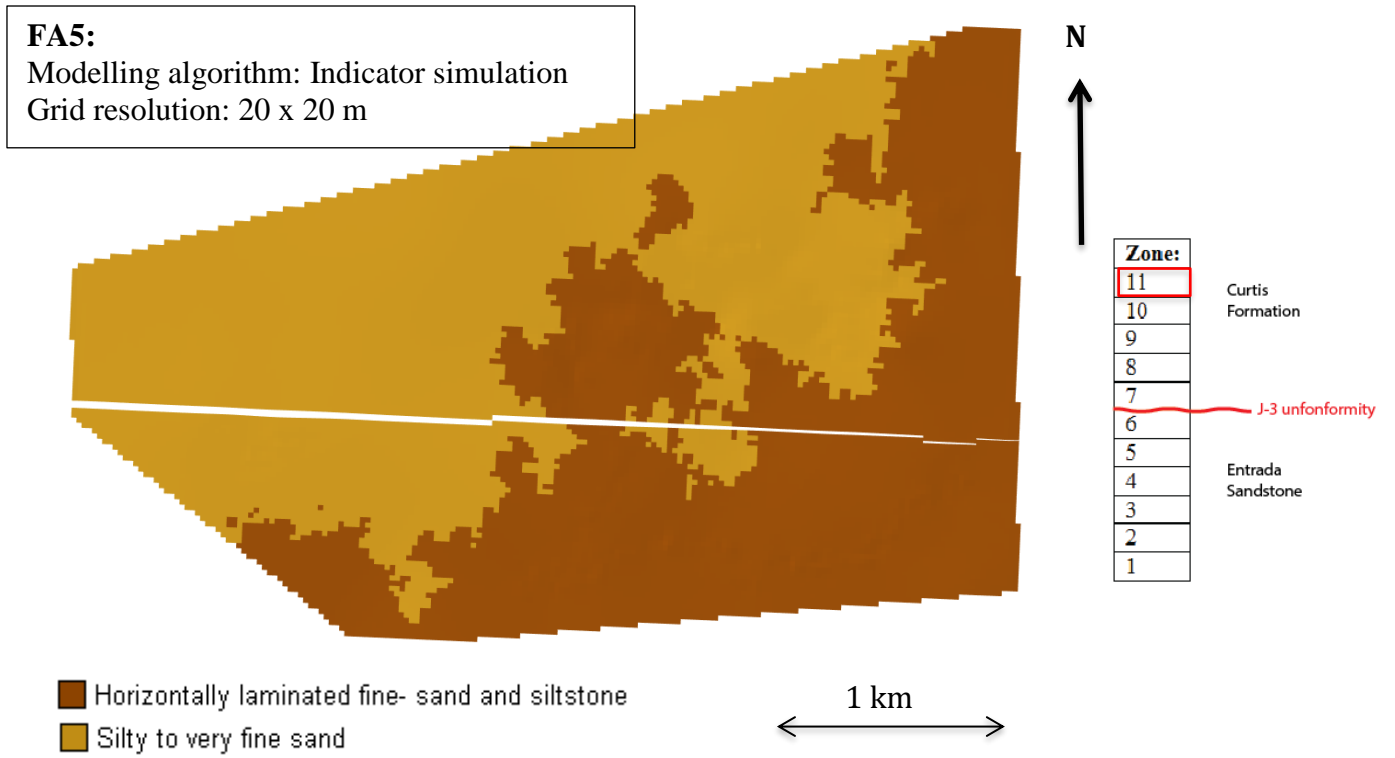
Figure 6.9.11: Model of facies association FA5, tidal mud flats.

6. Geological modelling

Table 6.9.3: Input data for facies modelling of the Curtis Formation.

Table	Facies:	Thickness:	Conceptual Description:	Length:	Width:	Amplitude Sinuosity
c_FA1: Channel modelling						
OLE	c_G	Background				
SER	c_I	Mean: 0.55 m Std. dev.: 0.1	Channel	-	Mean: 100 m Std. dev.: 10 m	Amplitude: 2000 Std. dev.: 400 Sinuosity: 1,46
c_FA2: Channel modelling						
OLE	c_G	Background				
MTCD	c_H	Mean: 3 m Std. dev.: 1.19	Channels	-	Mean:750 m Std. dev.: 300 m	Amplitude: 2500 Std. dev.: 400 Sinuosity: 1,46
SSB	c_E	Relative thickness: 0.7 Std. dev.:0.2	Crevasse as Elongated ellipses	Absolute lobe length: 5175 m	Relative lobe width: 1.5	-
c_FA3: Composite modelling						
OLE	c_G	Background				

6. Geological modelling

SSB	c_E	Mean: 1.65 m Std. dev.: 153	Object modelled: Elongated ellipses	Mean: 5865 m Std. dev.: 100 m	Mean: 850 m Std. dev.: 100 m	-
C_FA4: Belts				**Variogram:**		
Cross sectional geometry: Parallel Stacking pattern: Progradation Depositional type: linear				Parallel to azimuth: 1000 Normal to azimuth: 5000		
c_FA4 a: Composite modelling						
TSF_2	c_F	Background				
SSB	c_E	Mean: 1.63 m Std. dev.: 1.53	Barriers -Elongated ellipses	Mean: 5175m Std. dev.: 100 m	Mean: 750 m Std. dev.: 100 m	-
c_FA4 b: Channel modelling						
TSF_1	c_C	Background				
TCD	c_D	Mean: 1.3 m Std. dev.: 1.2	Channels- Sandbody mode	-	Mean: 400 m Std. dev.: 300 m	Amplitude: 1000 Std. dev.: 400 Sinuosity: 1.42
c_FA5: Indicator simulator		**Conceptual Description:**	**Variogram:**			
OLE	c_G	Background	Parallel to azimuth: 2000 Normal to azimuth: 2000			
TMF	c_A and c_B	Simulate facies				

7. DISCUSSION

According to Zakrevsky (2011), there are two main stages of an assessment of a geological model:

- Evaluation of the quantity and quality of input data
- Examination of the actual process of the model building in each stage

As the results obtained in this thesis must be evaluated in terms of model confidence, these two steps will be elaborated in this chapter. Evaluation of uncertainties related to input data are considered in section 7.1. Section 7.2 examines the steps of the modelling procedure, and discusses problems related to each step. Petrophysical properties are described in section 7.3.

7.1 Database and implementation

Uncertainty attached to the input dataset is important. These uncertainties are according to Martinius and Næss (2005) related to two main problems:

- Inadequate number of observations. In statistical terms this means that the number of measurements/observations described by the sample population is too small to reflect the properties of the global distribution.
- Insufficient data accuracy or representativeness of variables. In practice this relates to the accuracy of the measurements performed, and accuracy and/or suitability of the description/classification employed to characterize the dataset.

A brief explanation of the uncertainty of the dataset is provided for the sedimentary logs and Lidar images, as these are clearly important issues to consider.

Two logs from the Entrada sandstone, one on the hanging wall and one on the footwall, (Gurrik, 2016) have been incorporated into RMS. The hanging wall log consists of three separate segments.

The footwall log is much longer than the hanging wall log, where Fremont bed is the lowermost logged facies. The footwall log includes 56.75 m more of the Entrada sandstone than what is logged in the hanging wall. The facies associations observed on the hanging wall

7. Discussion

and footwall log can be linked to the Lidar images and correlated. The correlation using the Lidar image revealed a mismatch requiring a correction of the facies association logs. The corrected log is found in section 4.1.1 and original log in Appendix A.4. The corrected logs are implemented in RMS, but since there is no geomechanical- or petrophysical data located under e_FA2_3 and that there is only one log in the study area (outside the range of Lidar coverage), no zones have been made based on these facies association intervals. The precise position and altitude of the uppermost footwall log segment (FW3) was quality checked in the field.

Although Hope (2015) and Larsen (2015) present a log from the Entrada succession, this could not be implemented. The log by Hope (2015) has no coordinates attached to it, and the graphical quality of the log as presented was poor, and lacking information about facies and facies association made it difficult to correlate it to the data from Gurrik (2016). Consequently, this log could not be reliable implemented in RMS.

The sedimentary units located close to the Fremont bed were given layer numbers by some of the project workers who focused on geomechanical properties of this bed. This subdivision, which does not conform with the sedimentary based subdivision used by other workers caused some problems when trying to fit the measurements performed in this part of the stratigraphy. Consequently petrophysical and mechanical datasets obtained in the field could initially not be incorporated, as they could not reliably be placed in a facies context. This was partially corrected in the field in May 2017, but some work still remains in order to position all the described layers correctly in the database provided in this project.

For a correct model, it is required that the logs are correctly placed in terms of coordinates and altitudes. The altitude placement of the logs affects the model zonation, and wrong locations can cause large errors related to the facies distribution within the zone, and thereby affect the fluid flow simulation. In this project there is some uncertainty related to the accuracy of positioning and altitude of the logs. The coordinates of the logs collected by Rimkus (2016) was estimated by him in Google Earth, and the start coordinates, when quality checked, did not fit with the Lidar data or the lengths of the logs traced in Google Earth. Since a decision was made to implement the actual log paths, new log coordinates were estimated from a combination of Lidar images, Google Earth (see section 6.4.4 for a comprehensive description). The coordinates and altitude of the top of log 1 and 5 and were quality checked

7. Discussion

in field May 2017 using a hand-held GPS, and the respective coordinates adjusted in the model.

Some inconsistencies were found in the Petrel logs, facies association descriptions and logs provided in Rimkus (2016). This was corrected by fitting the Petrel logs to the description and the original logs in his thesis. This included that the thickness of the logs, and wrong termination in the digitized facies, when relating to the project and description in the thesis. The division into facies association has therefore also been modified.

The transition from Curtis to Summerville in log 3 is associated with great uncertainty as this transition is not observed in the other logs that are positioned stratigraphically higher, and the location of the boundary is supposed to be covered by scree. Figure 7.1.1 displays the logged stratigraphic thickness above the J-3 unconformity for each logs, these represent the minimum thickness of Curtis at these locations. The apparent variation in stratigraphic thickness of the Curtis Formation (only 40 m thick in log 3, if this is taken at face value) could be a result of the topography of the boundary between the Curtis and overlying Summerville Formation. However, this boundary appears to be conform with no observations suggesting incisions on the scale suggest by the Figure 7.1.1. This could indicate that the Curtis/Summerville contact in log 3 is likely to be wrong. The thickness of the Curtis formation is most likely larger than 40 m, which is supported by the results of Gilluly and Reeside (1928). The log/well pick of top Curtis in log 3 is therefore not used in the model.

Three of the sedimentary logs collected by Sleveland (2016) coincide with the three first logs to Rimkus (2016). Slevelands logs are not implemented as these were collected at the same time and place as those by Rimkus.
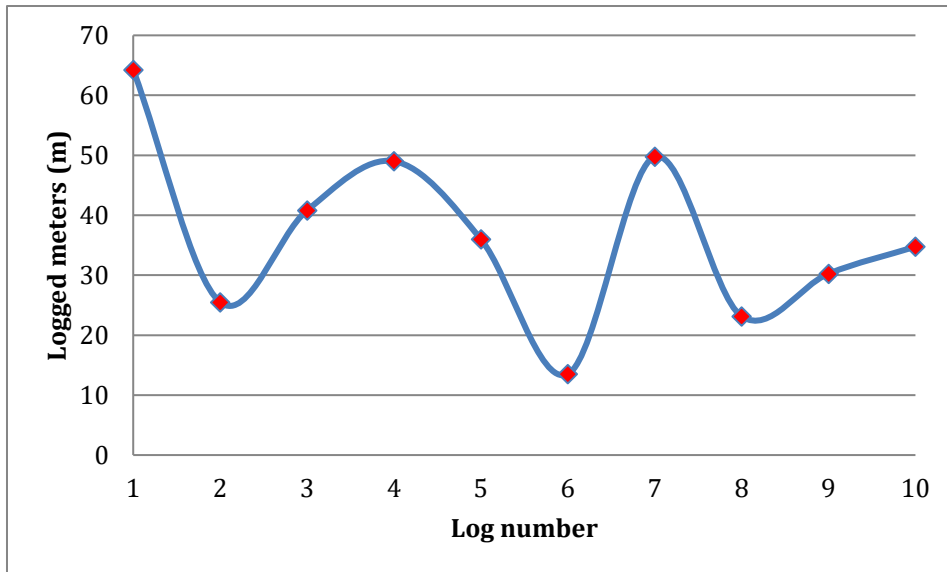
7. Discussion

Figure 7.1.1: The red dots represent the top of the logs collected by Rimkus (2016) measured from J-3 unconformity. The blue line represents the variation in logging height. Note that the logs are not represented in a spatial correct sense.

Merging data from different sources into one database is time consuming. Quality control of the data collected by different groups at different time presents a challenge (Howell et al. 2014). The master theses attached to the COPASS project group have used different sedimentary descriptions of the facies and facies associations for the Entrada sandstone and Curtis Formation. A great amount of time was spent on comparing and extracting the information and trying to harmonize the various descriptions. This is not unusual for a project in progress and involving numerous groups and worker, but it would ease subsequent modelling efforts significantly if workers used a common stratigraphic template as well as common scheme for definition of facies and facies associations, and workers were instructed to record GPS coordinates and altitudes precisely while logging and sampling.

The resolution of the digital elevation model (DEM), 9x9 meter, was locally enhanced using the interpreted points from Lime. Even with these improvements, the resolution of the DEM is considered low compared to Google Earth Pro. Problems occurred when digitizing log paths along the DEM. The low resolution resulted in several meters offset compared to Lidar due to smoothing of the topography, in particular along steep slope. The logs were therefore digitized in Google Earth Pro and the coordinates and altitudes manually copied to RMS for representation of the log paths. A more precise DEM would have been preferred for this purpose, ideally in combination with log paths traced by GPS.

7. Discussion

The Lidar segments from the study area mostly "connect" laterally and represent a continuous image of a large part of the outcrops in the area. As described, the Lidar images do not cover the lower slopes and valley bottoms, or the hill-crests. Bleached fractures located on flat lying areas are of particular interest to the project, are therefore not always imaged. Lack of Lidar data makes it difficult to map the uppermost part of the Curtis formation that is poorly exposed. The pinching out of Curtis facies association 2 (c_FA2) would not have been detected through well correlation, but with the available Lidar data it was possible to map the thickness variations (Rimkus, 2016). Artifacts, such as for example shadow effects and too much lighting makes it difficult to interpret and determine the lateral extent of some facies and facies associations.

Lack of Lidar data especially in areas of interest of this study, could have been avoided by carefully planning the aim of the Lidar scans and their placement. The area is characterized by a high topographic relief over short distances which make it difficult to position the Lidar scans in order to obtain coverage in Stove Gulch (Figure 7.1.2). An alternative to using ground based Lidar acquisition would have been to use a drone. With a drone it is possible to obtain a better vertical coverage of the area of interest which would have provided images of the flat-lying areas and a more detailed DEM. A disadvantage of using a drone is that the images may have lower resolution. However, this could be considered a minor drawback when compared with the potential benefits.

Figure 7.1.2 illustrates the distribution of available data in the field area for the J-3 unconformity between the Entrada sandstone and the Curtis Formation. Areas with dense data coverage have better quality (i.e. less uncertainty in the model) than areas, which are far from the nearest data point. In the innermost part of Sulphure Canyon, where log 3, 9 and 10 are located, there is no Lidar coverage. This is unfortunate as the logs are located on the hanging wall and the Lidar coverage in scan 1-3 is located on the footwall, making no correlation points before Stove Gulch, scan 4 and 9. The altitudes of these logs should have been checked in the field, but due to time constraints during the visit to the area in May 2017 this was unfortunately not possible.

7. Discussion
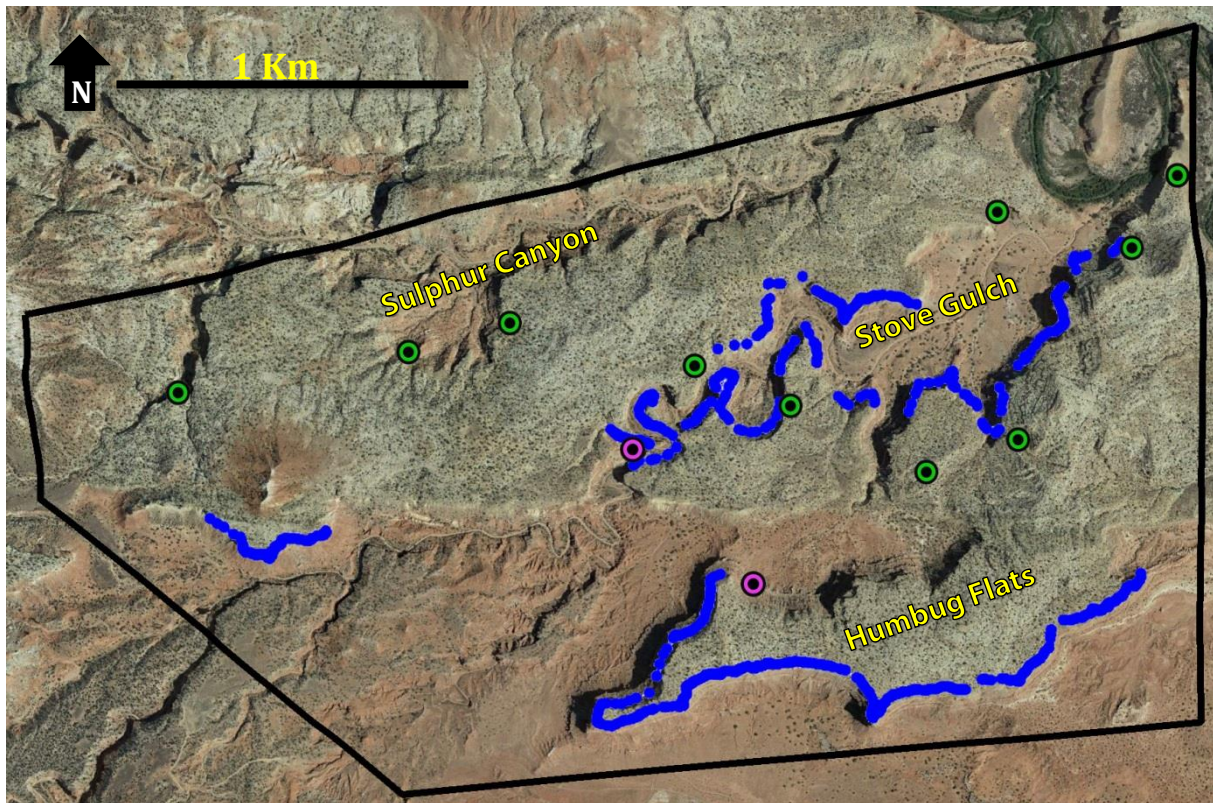
Figure 7.1.2: The blue points on the map shows the interpretation of J-3 unconformity located between the Entrada sandstone and the Curtis Formation. The points have been interpreted in Lime and imported into RMS. A picture of the study area has been overlain.

RMS is designed for modelling subsurface reservoirs, generally below sea level. In practice this entails that the scale is positive downwards from sea level, and negative upwards from sea level. When implementing data from outcrops above sea level, care must be taken to adjust the altitudes accordingly and transform altitudes to negative numbers by multiplying them by -1.

7. Discussion

7.2 Modelling

It is important to understand the limitations to modelling and that models are simplifications of the reality. The quality of models is not only limited by the type and quality of the input, but also by limitations posed by the software algorithms and conventions, which do not always facilitate realistic or optimal rendering of the geological features. It should also be kept in mind that uncertainty occurs at all stages in the modelling process. Models employ stochastic methods to handle uncertainty. In essence a model is a complex function with input variable values sampled from likely ranges. As there are a number of variables in a reservoir model, the model (or function) yields non-unique solutions called realizations. Reducing the number of variables or constraining the ranges of likely property values will constrain the range of outcomes (i.e. reduce uncertainty). The realizations all represent likely spatial distributions of properties, which fill in the space between the hard data (Deutsch, 2002). By applying facies distribution, size, shape and directional trends of the geological features, fewer possible outcomes are created. Subjective modelling decisions have been made due to limited data or to compensate for missing information. In most cases a geostatistical tool has been used to quantify and visualize the uncertainty and calculate risk regarding the model.

7.2.1 Framework and grid construction

Errors in the extrapolation and interpolation of surface maps and isochores from the observations were introduced due to the limited dataset of sedimentary logs or Lidar data. The resulting isochores and horizons depend on the use of an algorithm. As the algorithm uses approximates values where data is missing, there are some interaction between surface maps (maps representing the facies association transitions) and they intersected each other in areas with few data points. This occurs as the algorithm does not utilize information about positions of the overlying or underlying surfaces. If not corrected, this may cause serious problems when trying to build grids. The correction of intersecting surfaces was carried out using isochores, essentially allowing the algorithm to see neighbouring surfaces, and manually adding control points to guide the surface gridding algorithm. This is required to satisfy the conceptual model of the area (Enge et al, 2007). Even though these points are based on thickness information from the logs and Lidar images, these guiding points are just estimates and should be handled with some caution.

7. Discussion

The gridded horizons show an overall dip towards the northeast. The dip of the layers is most likely related to regional tectonics, associated with the San Rafael Swell monocline (Zuluaga, Fossen, & Rotevatn, 2014).

The fault intersecting the study area was first traced using Google Earth and subsequently traced in field using a GPS in May 2017. The steep slopes and hilly terrain in some areas made it impossible to trace it the whole way, but hiking along the fault across the study area made it possible to identify the fault in the terrain. The observations were also mapped on a printed copy of Google Earth image of the area on which the fault had been previously traced. By using the information from the GPS and Google Earth, a good representation of where the main fault intersects the surface was obtained. The fault intersects the Lidar scan 2-4 and can be observed in scan 2, but not traced in scan 3, as the area is mostly covered by scree (Figure 4.5.1).The main reason for tracing the fault is its impact on the fluid flow simulation, but also the complex bleaching patterns indicating that there could be several fault segments and not only one fault. If this is the case, the fault terminates close to scan 4 (Figure 4.5.1). This needs to be evaluated further, but such evaluation is beyond the scope of this thesis. For the modelling, the fault is considered as one continuous segment.

Grid construction
Grid size and resolution as well as the relations to faults, have a significant impact on modelling and simulation results. The resolution should be high enough to capture heterogeneities that are likely to influence flow, while the total numbers of cells in the model should be kept low in order to cut CPU cost. Grid adaption to fault may cause distortion of cells, which in turn may affect the fluid flow simulation outcomes. It is important to remember that the 3D grid model is a significant simplification in terms of geometries and properties. Grid quality control using tools built into the software was performed during modelling to identify and estimate the number of inadequate grid cells such as collapsed, disturbed, inclined, etc. Particular attention is given to the cells near the fault zone. If inadequate cells were identified, the grid setup was adjusted and the gridding procedure repeated until a satisfactory result was achieved. Grid type affects the modelling connectivity of the facies and may have a huge impact on the fluid flow modelling (Zakrevsky, 2011).

As described in section 6.7, proportional grids have been used throughout the model. The presence of erosional unconformities in the stratigraphy (J-3 unconformity and the boundary

7. Discussion

between c_FA1 and c_FA2) could be an argument for employing base conform gridding of the zones truncated by these unconformities. It should, however, be kept in mind that the cells in the transition between differently gridded zones commonly deviate from over- and underlying cells in terms of volume. This issue is avoided when using proportional gridding. Furthermore, the topographic relief of the two unconformities is small (on a meter scale), which makes the choice between proportional gridding and base conform less critical.

The c_FA1 zone located between the two unconformities fills in the topography of the J-3 unconformity, and is truncated and locally removed along the base of the overlying c_FA2. Choosing a suitable grid for this zone could therefore be difficult. However, c_FA1 consists largely of non-reservoir rocks. As no flow will pass through this unit, the choice of grid is not critical, and we chose a proportional grid in order to capture the pinchout geometry of c_FA1 in more correct manner (i.e. non-stair stepping).

Well path adaption to logged trace on surface

The input data for facies and facies associations were supplied as vertical logs, despite these having been logged along traces where start- and end- point are separated by up to 150+ m. Repositioning the log observations along their original log trace improves the accuracy of the model. Placing the observations correctly in the model implies an improved rendering of facies distribution, quantification of heterogeneities and facies connectivity (Lerat et al., 2002). This effect is especially pronounced in laterally heterogeneous areas. This has a significant affect when conditioning the model on the well information and therefore also later fluid flow simulation. Figure 7.2.1 illustrates the projected log trajectory for log 1, showing a 158 m horizontal difference between the start and end point of logging.

7. Discussion
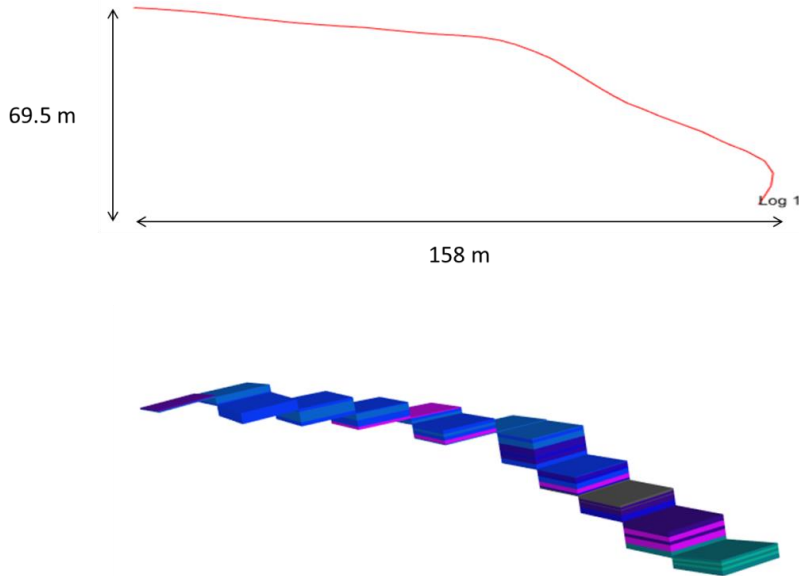
Figure 7.2.1: Illustration of the effect of a log path and the distribution of the blocked cells. The blocked cells have a 20 x 20 m horizontal resolution. The vertical resolution is dependent on the associated zones in the model (see section 6.7).

Facies modelling

RMS lacks a dedicated module that manages tidal channels. It is therefore not possible to model channels that die out in the model area or meandering channels that rapidly decrease in width and branch 90 degree angles. Facies c_I, interpreted as tidal channel point bar, and was only observed in log 8. This could indicate that it has a limited lateral extent, representing isolated channels filled in by point bar.

It is difficult to determine the variogram in modelling of the Entrada sandstone. This is especially related to the floodplain deposits, where the lateral extent and level of heterogeneity is unknown. The models should be considered "estimates" and should be improved on by conducting a survey of lateral variability of these units.

7. Discussion

7.3 Petrophysical database

Porosity and permeability values have been compiled from several sources. Table 2 in section 4.2 gives an overview of the available data and sources. The porosity and permeability values are located in Appendix D.

It is beneficial to use a facies-based approach in RMS, where individual facies are populated with porosity and permeability values. Available data for petrophysical properties determine if the facies are either assigned a constant value or determined with stochastical methods. A stochastic petrophysical modelling approach is preferred. This tool uses input data, trends and distributions of the petrophysical parameters to assign values to cells in the model (RMS). It is important to keep in mind that the petrophysical properties also vary on different scales, from full field scale to lamina scale. How detailed the model should implement these properties, depends on the aim for the model. For reservoir modelling the amount of data that can be implemented depends highly on the CPU costs.

Curtis Formation

There is little information regarding reservoir quality of the Curtis Formation in previous research. On-going studies of Curtis include Swindell (2015) purposing it a poor reservoir quality. Porosity values were collected by Rimkus (2016), and vertical and horizontal permeability was collected by the author in the field area May 2017 using a TinyPerm II instrument (Appendix D). Heterolithic tidal deposits represent particularly challenging reservoir systems to describe petrophsically, because they are highly anisotropic with generally marginal reservoir quality and variable net-to-gross ratios. Variation in width, length, orientation and thickness of the tidal sand banks are affecting factors (Wood, 2004). Heterogeneities can occur at different scales, but fine scale heterogeneities are not considered in conventional reservoir modelling tool (Ringrose and Bentley, 2015).

The porosity data set compiled by Rimkus (2016) lacks porosity measurements from facies c_F (wavy bedded mudstone) and c_G (lenticular bedded mudstone). Facies c_G (lenticular bedded mudstone) is located in the lowermost Curtis formation where it is considered to be a low permeable layer, appearing as a seal for the underlying Entrada reservoir (Monn, 2006). The overlying sandstone in c_FA2 shows little to no porosity (0.25%) and is pervasively

7. Discussion

cemented. In its present state, it is considered a non- reservoir, but could potentially have exhibited very good reservoir properties prior to diagenesis.

Facies c_F is interpreted as tidal sand flat. The layering of sand and mud in a tidal mud flat will result in large vertical anisotropy. Porosity measurements for tidal sand flat deposits are measured to be 1% and the tidal mud flat deposits are expected to be lower. The lenticular and wavy bedding may conceivably link up laterally and facilitate flow, even for low net-to-gross values (Jackson, Yoshida, Muggeridge, & Johnson, 2005). If such networks are present, the horizontal effective permeability is higher, and potential volumes and flow properties underestimated (Jackson, 2013).

The overall porosity measurements show extremely low to non-existing porosity in most of the layers (Appendix D). Early cementation and late quartz overgrowths are likely to have caused this, as the intergranular volume decreases as a function of cement (Paxton et al., 2002). Porosity and cement measurements together may be used to estimate the initial total porosity of the deposits.

The associated permeability values were measured by the author using a TinyPerm II in field May 2017. Due to time constrain all of the permeability values are from log 1. The low permeability measures are related to the low porosity measurements. For later flow simulation purposes, it should be considered to recalculate the pre-cementation porosity and permeability of the Curtis Formation.

Entrada sandstone
Larsen (2015) and Kristensen (in prep.) compiled porosity and permeability values from the Entrada Formation. Additional permeability measurements were collected by Sundal (pers. Comm), Skurtveit (pers. Comm) and by the author in May 2017. The Entrada sandstone is more studied in regards of reservoir quality. Most of the porosity and permeability measurements are from the Fremont bed and the strata immediately above and below it (Table 4.2.1).

Fluvial and sabkha sediments as interdunes and floodplain deposits are permeability barriers within the eolian sediments. Interdunes may act as vertical barriers and compartmentalize interbedded eolian sandstone reservoirs (Kocurek, 1981). Interdune deposits have poorer

7. Discussion

reservoir quality than dunes due to the poorly sorted finely laminated sediments and a high likelihood for the presence of evaporate cements deposits (Lindquist, 1983). Digenetic cementation and silt laminations also weaken the vertical permeability. On a smaller scale, low-permeable lamina can act as permeability barriers (Ringrose & Bentley, 2015), but very thin laminae in this environment rarely have lateral extents on a scale of hundreds of meters.

Available information of the Curtis Formation and Entrada sandstone porosity, ranges from non-existing to two thin sections per facies and cannot be considered a representative sample population (Jackson et al., 2005). In order to provide a more substantial database, petrophysical property distribution from analogues can be used (Geel & Donselaar, 2007). It should however, be kept in mind that porosity and permeability are related to diagenetic history and might not be applicable to reservoir analogues (Hicks et al., 2010).

Prior to later flow simulation, the petrophysical database could be supported and the model improved by:

- Recalculating the initial porosity values derived from thin sections by subtracting the cements.
- Find representative property distribution from similar depositional settings
- Conduct further field and plug measurements
- Perform a proper calibration of plug measurements and permeability measurements, as the latter commonly yield too high values (Braathen et al., 2012)

7.4 Flow simulation aspects

The present model is built to ultimately serve as input for fluid flow simulations. The model straddles the transition between a paleo-reservoir (Entrada) and its former cap rock (Curtis Formation). The presence of reducing fluids in the Entrada sandstone is evident by laterally extensive bleached zones. Bleaching along faults and fractures could be observed in numerous places, suggesting localized seal breaches.

Although both the petrophysical model and fracture model are yet to be implemented, it is possible to make an initial evaluation of some aspects likely to influence flow in this model. Lateral and vertical connectivity is likely to play an important role.

7. Discussion

Potential communication across J-3 unconformity

The zone c_FA1 directly overlies the J-3 unconformity and consists of mainly muddy rocks with low permeability and porosity, and is likely to act as a barrier to vertical fluid flow where present. The top of c_FA1 is truncated by an erosional unconformity and overlain by c_FA2 which has a high content of sand is likely (at least prior to cementation) to have had a relatively high porosity and permeability. Locally c_FA1 is completely missing due to erosion (Figure 7.4.1). In these locations c_FA2 is in direct contact with the Entrada sandstone across the J-3 unconformity. This creates vertical connectivity for fluid flow compromising the potential c_FA1 seal. In theory the shape of these windows should match the incision pattern evident at the base of c_FA2. Figure 7.4.1 display the thickness of c_FA1, the lowermost zone in the Curtis Formation. The red areas show where communication between Entrada and c_FA2 is likely to occur. Compared to where there is available data (Figure 7.1.2) this is representative. The circled area represent where FA2 is observed incising into the Entrada sandstone on Lidar images (Figure 5.2).

Curtis facies association one (c_FA1) expressed as zone 7, directly overlying the J-3 unconformity is a low reservoir quality rock and most likely hinders any communication across the facies. Zone 8 (c_FA2) have potentially high reservoir quality. Measurements from the field area express low reservoir quality that can be related to the high degree of cements (Table D.1.5).
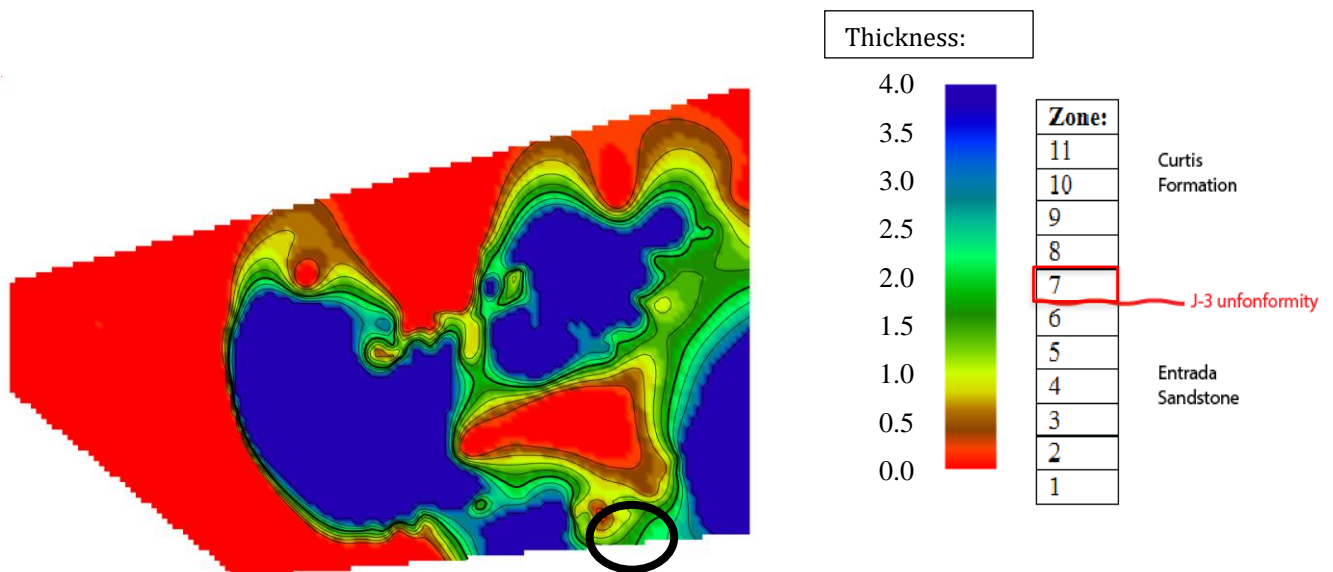
Figure 7.4.1 Thickness map with minimum and maximum values of zone 8 between the J-3 unconformity and c_Top_FA1. Where the area is zero (red) there will be a communication between top Entrada and c_FA2.

7. Discussion

This can be handled with optional gridding since properties of lower parts of c_FA2 critical. Base conform gridding, only communication in the lower part of the facies. By using a proportional gridding type a communication between along the lower part of the facies is obtained.
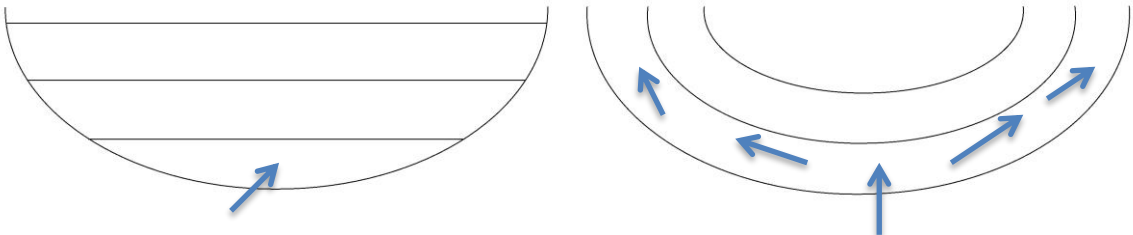
Figure 7.4.2: Communication between different gridding options. To the left a top conform grid is illustrated; here the flow communication is concentrated in the lower part of the channel. If a base conform or a proportional gridding method is used there is more communications throughout the channel.

8. CONCLUSIONS

The aims of this thesis were to compile and systematize data collected by the COPASS project in the study area as of May 2017, and implement these data into a coherent geo-model, while identifying any problems related to input data and model implementation. A modelling workflow was developed and quality assessment of the various stages was carried out. The reservoir model will be used for further work in the COPASS project, and refined as more data becomes available. The main conclusions and insight from the present study can be summed up as follows:

- Model implementation of logs was severely hampered by the lack of a common stratigraphic template and scheme for definition of the facies and facies associations. A lot of time was spent on making the input data consistent for use in the model, which could have been avoided if a common scheme had been employed.

- Positional data, in particular with respect to altitude measurements was inadequate. In many cases the altitudes had to be inferred by correlating the logs with the available Lidar images.

- Lidar data make it possible to employ 3D quantitative data such as length, width, thickness and facies associations e.g. in a highly accurate way correctly in space. It is an effective tool for building a more deterministic model. However, in hindsight it would have been better to use drone based photogrammetry of the whole area. The Lidar images covers only parts of the outcrops and some of the logs used here where acquired outside of these. Since precise altimetry of these was not extant, these logs can not be implemented without supplementary measurements. Complete photogrammetric coverage would have reduced the uncertainty of the horizon interpretations significantly.

- The model set-up provided in the present thesis is considered a robust base for further work, in particular with respect to the structural framework, although some checks and adjustments in areas with no present data coverage should be performed.

- In sum, the plan for data acquisition should have been coordinated better. The present thesis may provide some guideline as to how this can be improved for the remainder of the COPASS project.

8. Conclusion

8.1 Suggestions for further work

The purpose of this thesis was to compile a database of the available data in the study area and to describe the modelling procedure. Further work, that will be necessary for the COPASS project is to identify paths and analyze reservoir response to CO_2 pressure and migration. By predicting how CO_2 flows along sediment layers and faults and how other geological features play a role in where and how CO_2 flows through reservoirs and how it will migrate into the overlying succession one gain insight to project where possible new CO_2 injection are evaluated.

- Make a common stratigraphic template and scheme for definition of the facies and facies associations of the Entrada sandstone.
- Compile a larger dataset on petrophysical properties, for a statistical evaluation to better preform the petrophysical modelling.
- Include more logs of the Entrada Formation in the study area, and log of the Curtis Formation on the footwall is preferred.
- Include fracture network dataset and density of deformation bands.
- Implement smaller faults within the Entrada sandstone
- Evaluation of the top seal.
- Sensitivity studies on selected parameters to map out their impact on reservoir quality, integrity and responses – thus providing tool for forecasting suitability of a given site for CO_2 storage. By systematically changing individual input parameters (geometries, matrix petrophysical properties, fracture apertures, pressure etc.) the impact of these can be mapped using flow simulation.
- This allows studying the relationship between where leakages occur and geological structure, rock properties of the reservoir and cap-rock and provides a framework for conducting fluid flow simulations to map out the impact of key geological parameters on top – seal integrity.
- Include fault facies in the reservoir model as these have crucial effect on the fluid flow. Evaluation of fault seal.
- Overlay seismic on the Lidar images, to enhance the understanding of how it is expected to be expressed on the seismic.
- It should also be considered to acquire a complete photogrammetric imagery of the study site using a drone.

9. REFERENCES

Bachu, S. (2008). CO 2 storage in geological media: role, means, status and barriers to deployment. *Progress in Energy and Combustion Science, 34(2),* 254-273. doi:10.1016/j.pecs.2007.10.001

Behzadi, H., Alvarado, V., & Lynds, R. (2012). Modeling CO 2 saturation distribution in eolian systems. *International Journal of Greenhouse Gas Control, 11*, 110-116. doi:10.1016/j.ijggc.2012.08.004

Bellian, J. A., Kerans, C., & Jennette, D. C. (2005). Digital outcrop models: applications of terrestrial scanning lidar technology in stratigraphic modeling. *Journal of sedimentary research, 75*(2), 166-176.

Blakey, R. C. (2008). Pennsylvanian–Jurassic sedimentary basins of the Colorado Plateau and southern Rocky Mountains. *Sedimentary Basins of the World, 5*, 245-296 doi:10.1016/S1874-5997(08)00007-5

Braathen, A., Bælum, K., Christiansen, H.H., Dahl, T., Eiken, O., Elvebakk, H., Hansen, F., Hanssen, T.H., Jochmann, M., Johansen, T.A., Johnsen, H., Larsen, L., Lie, T., Mertes, J., Mørk, A., Mørk, M.B., Nemec, W., Olaussen, S., Oye, V., Rød, K., Titlestad, G.O., Tveranger, J. & Vagle, K.: The Longyearbyen CO2 Lab of Svalbard, Norway—initial assessment of the geological conditions for CO2 sequestration. Norwegian Journal of Geology, Vol 92, pp. 353–376. Trondheim 2012, ISSN 029-196X.

Buckley, S. J., Howell, J.A., Enge, H.D., & Kurz, T.H. (2008). Terrestrial laser scanning in geology: data acquisition, processing and accuracy considerations. *Journal of the Geological Society, 165*(3), 625-638.

Caers, J. (2005). *Petroleum geostatistics*: Richardson, TX: Society of Petroleum Engineers.

Chan, M. A., Parry, W.T., & Bowman, J.R. (2000). Diagenetic hematite and manganese oxides and fault-related fluid flow in Jurassic sandstones, southeastern Utah. *AAPG bulletin, 84*(9), 1281-1310.

Dalrymple, R. W., Mackay, D. A., Ichaso, A. A., & Choi, K. S. (2012). Processes, morphodynamics, and facies of tide-dominated estuaries *Principles of tidal sedimentology* (pp. 79-107): Springer. https://link.springer.com/chapter/10.1007/978-94-007-0123-6_5#page-1

DeCelles, P. G. (2004). Late Jurassic to Eocene evolution of the Cordilleran thrust belt and foreland basin system, western USA. *American Journal of Science, 304*(2), 105-168. doi:10.2475/ajs.304.2.105

Desjardins, P. R., Buatois, L. A., & Mangano, M. G. (2012). Tidal flats and subtidal sand bodies. *Trace fossils as indicators of sedimentary environments, Developments in Sedimentology, 64*, 529-561. doi:10.1016/B978-0-444-53813-0.00018-6

Deutsch, C. V. (2002). *Geostatistical reservoir modeling. Applied geostatistics series*. New York: Oxford University Press

Dickinson, W. R., & Gehrels, G. E. (2003). U–Pb ages of detrital zircons from Permian and Jurassic eolian sandstones of the Colorado Plateau, USA: paleogeographic implications. *Sedimentary Geology, 163*(1), 29-66. doi:10.1016/S0037-0738(03)00158-1

Enge, H. D., Buckley, S. J., Rotevatn, A., & Howell, J. A. (2007). From outcrop to reservoir simulation model: Workflow and procedures. *Geosphere*, *3*(6), 469-490.

Appendix A

Filomena, C.M., Hornung, J., & Stollhofen, H. (2014). Assessing accuracy of gas-driven permeability measurements: a comparative study of diverse Hassler-cell and probe permeameter devices. *Solid Earth, 5*(1), 1-11. doi:10.5194/se_5_1_2014

Geel, C.R., & Donselaar, M.E. (2007). Reservoir modelling of heterolithic tidal deposits: sensitivity analysis of an object-based stochastic model. *Netherlands Journal of Geosciences-Geologie en Mijnbouw, 86*(4), 403-411.

Gilluly, J., & Reeside Jr, J. B. (1928). *Sedimentary rocks of the San Rafael Swell and some adjacent areas in eastern Utah. Shorter contributions to general geology.* Professional paper 150-D.

Gurrik, O. R. (2016). *Damage Zone Characteristics of an Exhumed Reservoir-Caprock Succession - An Example of Fluid Flow in Upper Jurassic Sandstones, Central Utah.*

Hicks, T. C., Morris, T. H., & Fairbanks, M. D. (2010). Facies Analysis of the Transitions Between Subtidal, Intertidal, and Supratidal Zones of the Entrada Sandstone, South-Central Utah: A Provisional Sequence Stratigraphic Analysis. *Geology of South Central Utah,2010,317-337*

Hintze, L., & Kowallis, B. (2009). Geologic history of Utah: Brigham Young University Geology Studies Special Publication 9: Tech. rept. Brigham Young University, Salt Lake City, UT.

Hope, I. (2015). *Deformation bands in Collapsed sandstone reservoirs - An example from Upper Jurassic Entrada Formation, Utah, USA.* (Master Thesis, University of Oslo, Department of Geosciences). I. Hope, Oslo

Howell, J. A., Martinius, A. W., & Good, T. R. (2014). The application of outcrop analogues in geological modelling: A review, present status and future outlook. *Geological Society, London, Special Publications, 387*(1), 1-25. doi:10.1144/SP387.12

Jackson, M. D., Yoshida, S., Muggeridge, A. H., & Johnson, H. D. (2005). Three-dimensional reservoir characterization and flow simulation of heterolithic tidal sandstones. *AAPG bulletin, 89*(4), 507-528.

Jones, L. S., & Blakey, R. C. (1997). Eolian-fluvial interaction in the Page Sandstone (Middle Jurassic) in south-central Utah, USA—a case study of erg-margin processes. *Sedimentary Geology, 109*(1), 181-198. doi:10.1016/S0037-0738(96)00044-9

Kocurek, G. (1981). Erg reconstruction: the Entrada sandstone (Jurassic) of northern Utah and Colorado. *Palaeogeography, Palaeoclimatology, Palaeoecology, 36*(1), 125-153. doi:10.1016/0031-0182(81)90054-7

Larsen, E. B. (2015). *Geomechanical and Structural characteristics of a paleoreservoir-caprock sucsession; sandstones of Humbugflats, Central Utah.* (Master Thesis, University of Oslo, Department of Geosciences) E.B. Larsen, Oslo.

Lerat, O., Doligez, B., Desaubliaux, G., Daniel, J. M., Eschard, R., Garcia, F., Chauvin. H., Coureaud, B., Nussbaumer, C. & Rouvroy, P. (2002). Integration of Horizontal Wells In Reservoir Models: Input from an Outcrop Study. In *SPE Annual Technical Conference and Exhibition*. Society of Petroleum Engineers. doi:10.2118/77672-MS

Leuven, J., Kleinhans, M.G., Weisscher, S.A.H., & van der Vegt, M. (2016). Tidal sand bar dimensions and shapes in estuaries. *Earth-Science Reviews, 161*, 204-223. doi:10.1016/j.earscirev.2016.08.004

Lindquist, S. J. (1983). Nugget Formation reservoir characteristics affecting production in the overthrust belt of southwestern Wyoming. *Journal of Petroleum Technology, 35*(07), 1,355-351,365. doi:10.2118/10993-PA

Liu, S., & Currie, C. A. (2016). Farallon plate dynamics prior to the Laramide orogeny: Numerical models of flat subduction. *Tectonophysics, 666*, 33-47. doi:10.1016/j.tecto.2015.10.010

Appendix A

Loope, D. B., Steiner, M. B., Rowe, C. M., & Lancaster, N. (2004). Tropical westerlies over Pangaean sand seas. *Sedimentology, 51*(2), 315-322. doi:10.1046/j.1365-3091.2003.00623.

Martinius, A. W., & Næss, A. (2005). Uncertainty analysis of fluvial outcrop data for stochastic reservoir modelling. *Petroleum Geoscience*, *11*(3), 203-214. doi: 10.1144/1354-079303615

Murphy, M. A., & Salvador, A. (1999). International Subcommission on Stratigraphic Classification of IUGS International Commission on Stratigraphy-International Stratigraphic Guide-An Abridged Version. *Episodes, 22*(4), 255-271.

O'Sullivan, R. B. (1981). *Stratigraphic sections of Middle Jurassic Entrade sandstone and related rocks from Salt Valley to Dewey Bridge in East-Central Utah.* Washington D.C: Geological Survey

Ogata, K., Senger, K., Braathen, A., & Tveranger, J. (2014). Fracture corridors as seal-bypass systems in siliciclastic reservoir-cap rock successions: Field-based insights from the Jurassic Entrada Formation (SE Utah, USA). *Journal of Structural Geology, 66*, 162-187. doi:10.1016/j.jsg.2014.05.005

Paxton, S. T., Szabo, J. O., Ajdukiewicz, J. M., & Klimentidis, R. E. (2002). Construction of an intergranular volume compaction curve for evaluating and predicting compaction and porosity loss in rigid-grain sandstone reservoirs. *AAPG bulletin, 86(12),* 2047-2067. doi : 10.1306/61EEDDFA-173E-11D7-8645000102C1865D

Peterson, F. (1994). *Sand dunes, sabkhas, streams, and shallow seas: Jurassic paleogeography in the southern part of the Western Interior Basin.* Rocky Mountain Section (SEPM) ?

Raza, A., Rezaee, R., Gholami, R., Bing, C. H., Nagarajan, R., & Hamid, M. A. (2016). A screening criterion for selection of suitable CO 2 storage sites. *Journal of Natural Gas Science and Engineering, 28,* 317-327. doi: 10.1016/j.jngse.2015.11.053

Reynolds, A. D. (2016). Paralic reservoirs. *Geological Society, London, Special Publications, 444*, SP444. 410. 20, 2016, doi:10.1144/SP444.10

Rimkus, A. (2016). *A high-resolution depositional model of the tidally-influenced Middle Jurassic Curtis Formation, Humbug Flats, Utah, USA.* (Master Thesis, University of Oslo, department of Geosciences) A. Rimkurs, Oslo.

Ringrose, P., & Bentley, M. (2015). *Reservoir model design. A practitioner's guide*: Springer.

Ringrose, P., Nordahl, K., & Wen, R. (2005). Vertical permeability estimation in heterolithic tidal deltaic sandstones. *Petroleum Geoscience, 11*(1), 29-36. doi:10.1144/1354-079303-614

Ringrose, P. S., Skjetne, E., & Elfenbein, C. (2003). *Permeability estimation functions based on forward modeling of sedimentary heterogeneity.* Paper presented at the SPE Annual Technical Conference and Exhibition. doi:10.2118/84275-MS

Romain, H. G., & Mountney, N. P. (2014). Reconstruction of three-dimensional eolian dune architecture from one-dimensional core data through adoption of analog data from outcrop. *AAPG bulletin, 98*(1), 1-22. doi:10.1306/05201312109

Rotevatn, A., Buckley, S. J., Howell, J. A., & Fossen, H. (2009). Overlapping faults and their effect on fluid flow in different reservoir types: A LIDAR-based outcrop modeling and flow simulation study. *AAPG bulletin, 93(3),* 407-427. doi:10.1306/09300807092

ROXAR, (2017a). Creating the Grid.

ROXAR. (2017b). Appendix F - Facies Modelling Theory.

Sleveland, A. R. N. (2016). *The sedimentology and sequence stratigraphy of the Curtis Formation along the eastern San Rafael Swell, Utah.*(Master Thesis, University of Oslo) A.R.N. Sleveland, Oslo.

Appendix A

Swindell,T. (2015). A Reservoir Model for Exploration in an Estuarine Embayment: The Curtis Formation of the Western San Rafael Swell, Emery County, Utah. *AAPG Search and Discovery [Online], Article #90249.*

Taylor, W. J., Bartley, J. M., Martin, M. W., Geissman, J. W., Walker, J. D., Armstrong, P. A., & Fryxell, J. E. (2000). Relations between hinterland and foreland shortening: Sevier orogeny, central North American Cordillera. *Tectonics, 19*(6), 1124-1143. doi: 10.1029/1999TC001141

Thorman, C. H., & Peterson, F. (2003). *The Middle Jurassic Elko Orogeny-A Major Tectonic Event in Nevada-Utah.* Paper presented at the Annual Meeting Expanded Abstracts, Salt Lake City, Utah, 11-14 may, 2003.

Wilcox, W. T. (2007). *Sequence stratigraphy of the Curtis, Summerville and Stump Formations, Utah and Northwest Colorado.* (Master of science, Miami University) Hentet fra : http://rave.ohiolink.edu/etdc/view?acc_num=miami1177422597

Wood, L. J. (2004). Predicting tidal sand reservoir architecture using data from modern and ancient depositional systems.

Wright, J. C., Shawe, D. R., & Lohman, S. W. (1962). Definition of members of Jurassic Entrada Sandstone in east-central Utah and west-central Colorado. *AAPG bulletin, 46*(11), 2057-2070.

Zakrevsky, K. E. (2011). *Geological 3D modelling*: EAGE Publ.

Zuluaga, L. F., Fossen, H., & Rotevatn, A. (2014). Progressive evolution of deformation band populations during Laramide fault-propagation folding: Navajo Sandstone, San Rafael monocline, Utah, USA. *Journal of Structural Geology, 68*, 66-81. doi:10.

APPENDIX A – LOG INFORMATION

A.1 Coordinate and altitude of the logs

Table A.1.1: Rimkus (2016) collected ten logs within the study area spring 2015. The coordinates are from Rimkus (2016). These positions were estimated using Google Earth, and can be considered approximate and only include the start position of the logs. The altitude is found from Google Earth and correlation with Lidar images.

Locality	Zone (UTM)	Easting (m E)	Northing (m N)
Log 1	12S	541134.40	4354670.11
Log 2	12S	540394.54	4354701.39
Log 3	12S	538582.89	4354799.48
Log 4	12S	541644.04	4355521.83
Log 5	12S	540734.07	4354594.02
Log 6	12S	541081.88	4355369.02
Log 7	12S	541464.52	4355252.67
Log 8	12S	540134.93	4354910.91
Log 9	12S	539558.46	4355015.24
Log 10	12S	539260.17	4354926.80

Table A.1.2: Corrected coordinates used in modelling and in the map (Figure 4.1.1). Start and end point included.

Locality	Zone (UTM)	Top/Base	Easting (m E)	Northing (m N)	Altitude (meters):
Log 1	12S	Top[0]	541235.68	4354756.04	1648.00
		Base[+]	541088.33	4354694.30	1578.50
Log 2	12S	Top[*]	540282.00	4354646.00	1614.50
		Base[+]	540392.00	4354777.00	1583.00
Log 3	12S	Top[*]	538702.00	4354527.00	1684.50
		Base[*]	538580.31	4354793.22	1638.00
Log 4	12S	Top[*]	541619.00	4355221.00	1611.00
		Base[*]	541633.00	4355417.00	1559.00
Log 5	12S	Top[0]	540853.34	4354588.69	1618.00
		Base[*]	540701.00	4354544.00	1574.50
Log 6	12S	Top[*]	540909.00	4355442.00	1570.00
		Base[*]	541061.92	4355378.34	1553.00
Log 7	12S	Top[*]	541455.00	4355172.00	1613.75
		Base[+]	541442.84	4355258.96	1561.75
Log 8	12S	Top[*]	540143.89	4354898.51	1598.75
		Base[0]	540158.14	4354848.94	1567.00
Log 9	12S	Top[*]	539746.84	4354969.96	1638.00
		Base[*]	539555.00	4354995.00	1606.00
Log 10	12S	Top[*]	538935.00	4354738.00	1660.00
		Base[*]	539202.00	4354869.00	1623.50

[0] *Positions and altitudes checked using GPS*

[+] *Altitudes picked from Lime*

[*] *Altitude picked from Google Earth*

Appendix A

Table A.1.3: Sleveland (2016) collected three logs within the study area spring 2015. The coordinates are from Slevelad (2016). The locations are mapped in Figure 4.1.1.

Locality	Zone	Easting (m E)	Northing (m N)
1.Stove Gluch East	12S	541150 m E	4354677 m N
2. Stove Gulch West	12S	540412 m E	4354758 m N
3. Sulphur Canyon	12S	538598 m E	4354691 m N

Table A.1.4: Location of logs collected by Gurrik (2016) spring 2015, and used in the map (Figure 4.1.1). One log is collected on both sides of the fault. The log on the footwall is segmented into three logs with different coordinates and heights. The height represent the top of the log.

Locality		Zone	Easting (m E)	Northing (m N)	Altitude (meters)
Hanging wall:	HW	12S	539930.93 m E	4354639.80 m N	1600.00
Footwall:					
1 - 15.65 m	FW1	12S	538598.00 m E	4354691.00 m N	1600.00
15.65 – 54.35 m	FW2	12S	540044.57 m E	4354140.97 m N	1633.00
54.35 – 92.45 m	FW3	12S	540325.24 m E	4354214.56 m N	1659.10

Appendix A

A.2 Digitized Entrada log

Table A.2.1: Digitizing Entrada log. When digitizing the log a number is needed to represent a facies. The different facies are therefore assigned numbers.

e_A	e_B	e_C	e_D	e_E	e_F	e_G
20	21	22	23	24	25	26

Hanging wall:

Table A.2.2: Digitized hanging wall log from (Gurrik, 2016). MD is measured from the top of the log. Figure A.4.1 show the original log.

MD	Altitude (m)	Fascies	Number	
0	1600	A	20	
0.75	1599.25	D	23	
0.85	1599.15	A	20	
1.5	1598.50	D	23	
1.6	1598.40	A	20	e_Top_FA3_1
6.5	1593.5	G	26	
6.8	1593.2	A	20	
7.7	1592.3	G	26	
8	1592	B	21	e_Top_FA1_1
8.5	1591.5	F	25	
8.9	1591.1	D	23	
9	1591	A	20	
11.4	1588.6	D	23	
11.5	1588.5	A	20	
12.4	1587.6	B	21	e_Top_FA2_2
12.5	1587.5	A	20	
14.5	1585.5	D	23	
15	1585	A	20	e_Top_FA3_3
22.5	1577.5	D	23	
23.5	1576.5	G	26	
24.4	1575.6	D	23	e_Top_FA1_2
26	1574	A	20	
27.8	1572.2	A	20	e_Top_FA3_4
28	1572	D	23	
28.3	1571.7	A	20	
28.5	1571.5	D	23	
29	1571	G	26	e_Top_FA4
29.5	1570.5	E	24	
32	1568	A	20	

Appendix A

Footwall:

Table A.2.3: Digitized footwall log from (Gurrik, 2016). The log is divided into three segments. FW1, FW2 and FW3.

FW1

MD	Altitude (m)	Facies	Number
0	1600	C	22
2.80	1597.2	A	20
5.30	1594.7	C	22
7.30	1592.7	B	21
7.50	1592.5	C	22
11.80	1588.2	B	21
12.80	1587.2	A	20
13.55	1586.45	C	22
15.30	1584.7		

FW2

MD	Altitude (m)	Facies	Number
0	1633	F	25
3	1630	A	20
3.70	1629.3	B	21
4.20	1628.8	A	20
4.70	1628.3	B	21
5.00	1628	A	20
5.50	1627.5	B	21
6.50	1626.5	A	20
8.00	1625	B	21
8.50	1624.5	A	20
10.00	1623	D	23
10.20	1622.8	A	20
10.80	1622.2	B	21
12.20	1620.8	A	20
12.50	1620.5	B	21
13.00	1620	A	20
13.50	1619.5	B	21
15.00	1618	A	20
16.00	1617	B	21
17.50	1615.5	A	20
19.00	1614	B	21
21.50	1611.5	A	20
24.00	1609	B	21
24.20	1608.8	A	20
24.40	1608.6	B	21
24.50	1608.5	A	20
25.00	1608	B	21
26.00	1607	A	20
38.00	1595	A	20
38.50	1594.5	C	22
38.70	1594.3	A	20

Appendix A

FW3

MD	Altitude (m)	Facies	Number
0	1659.1	A	20
7.40	1651.7	A	20
7.50	1651.6	G	26
7.80	1651.3	D	23
8.10	1651	G	26
8.40	1650.7	A	20
8.60	1650.5	G	26
9.10	1650	D	23
9.50	1649.6	G	26
9.80	1649.3	B	21
15.30	1643.8	A	20
16.30	1642.8	F	25
16.50	1642.6	B	21
19.50	1639.6	A	20
19.80	1639.3	D	23
25.50	1633.6	A	20
26.00	1633.1	G	26
27.00	1632.1	D	23
29.50	1629.6	B	21
30.10	1629	A	20
30.20	1628.9	D	23
32.00	1627.1	A	20
32.50	1626.6	D	23
33.60	1625.5	B	21
35.40	1623.7	F	25
36.00	1623.1	F	25
38.00	1621.1	A	20

e_Top_FA3_1 (at MD 0)

e_Top_FA1_1 (at MD 9.50)

e_Top_FA2_2 (at MD 16.30)

e_Top_FA3_3 (at MD 19.80)

e_Top_FA1_2 (at MD 29.50)

e_Top_FA3_4 (at MD 30.20)

e_Top_FA4 (at MD 33.60)

A.3 Curtis logs

LOG 1

LOG 2

LOG 6
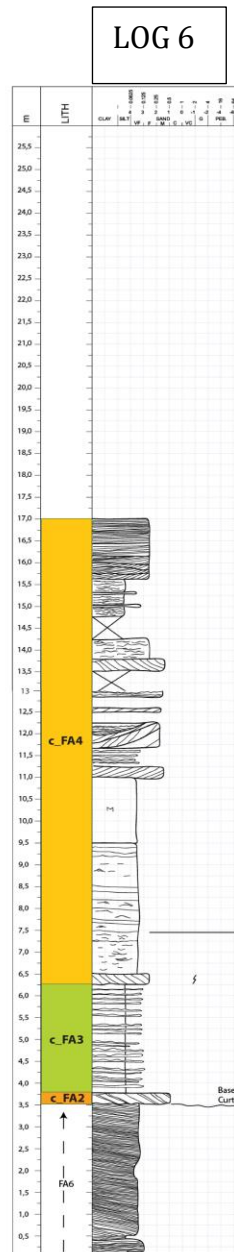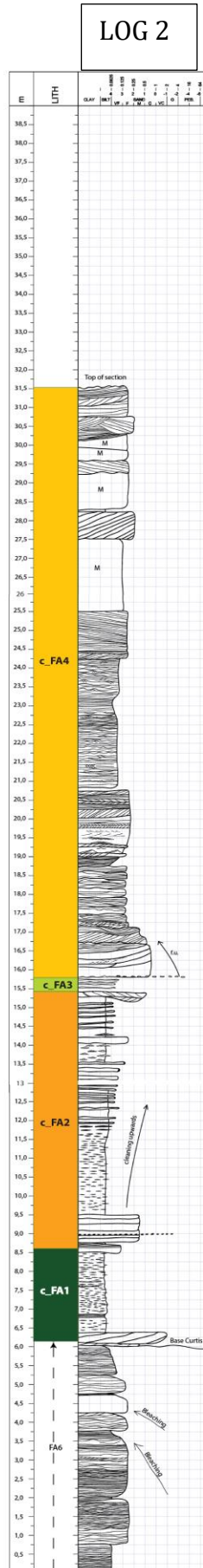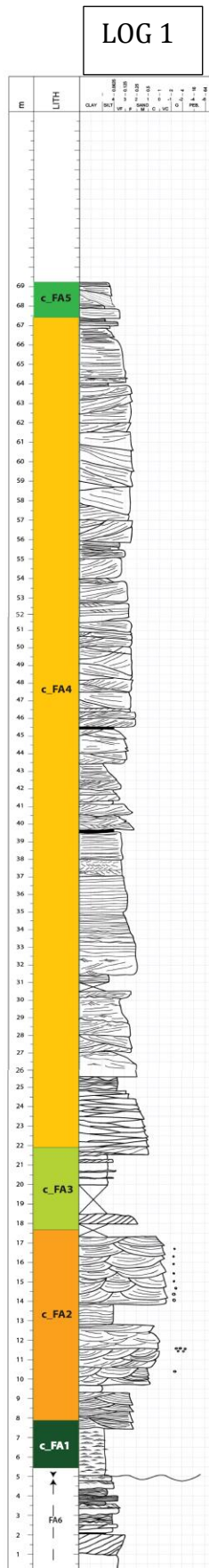
LOG 3
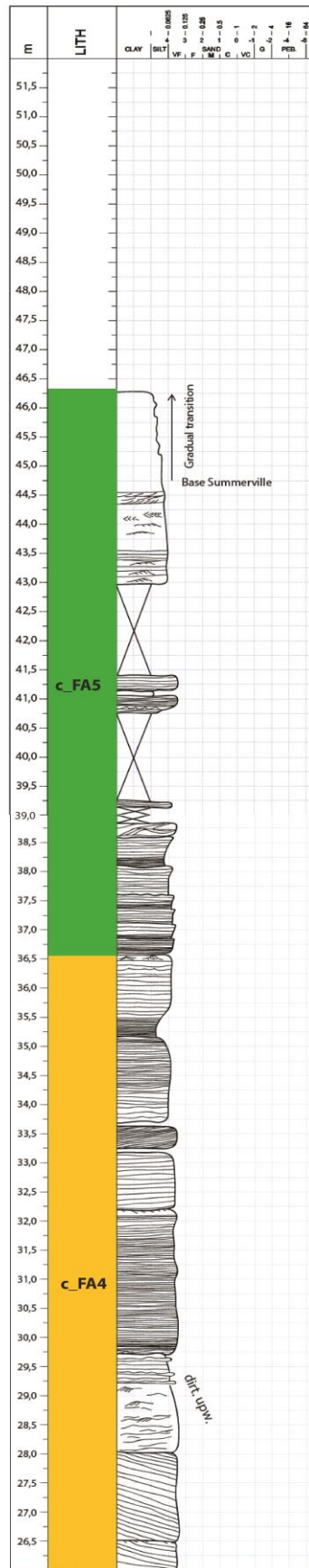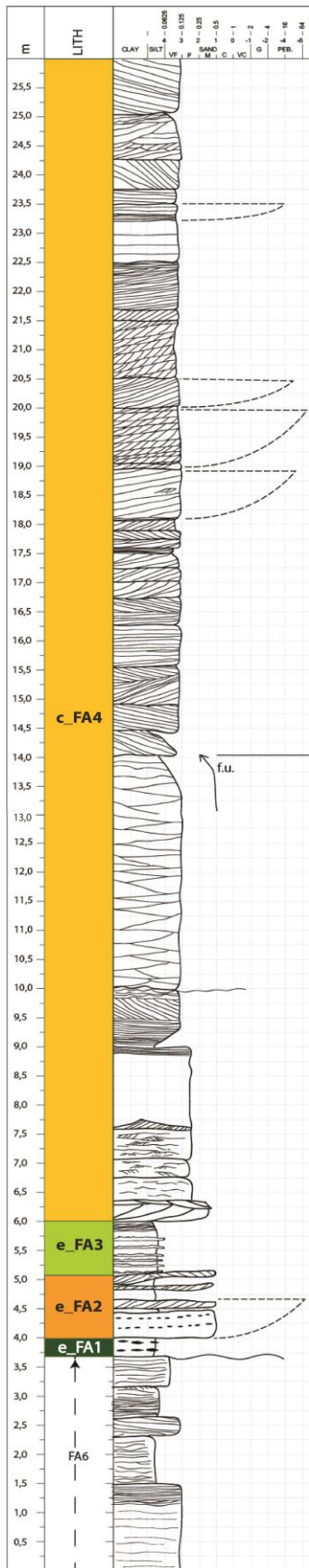
LOG 4
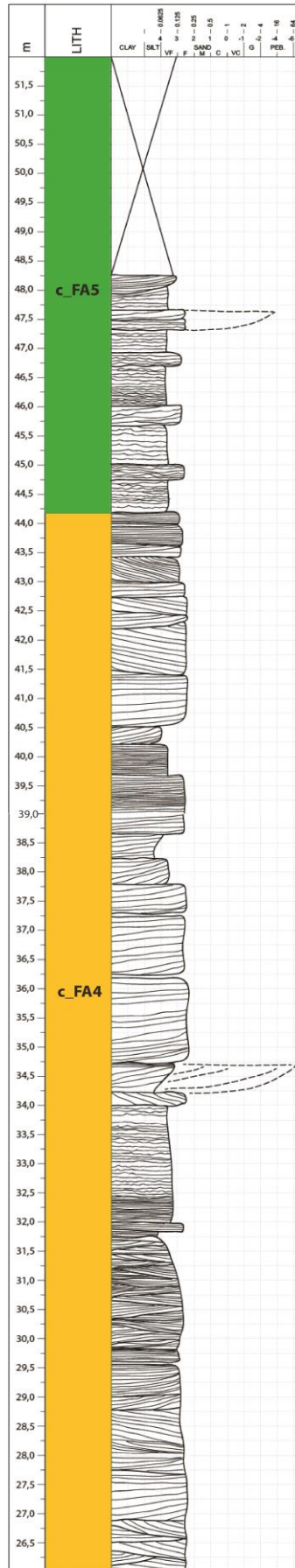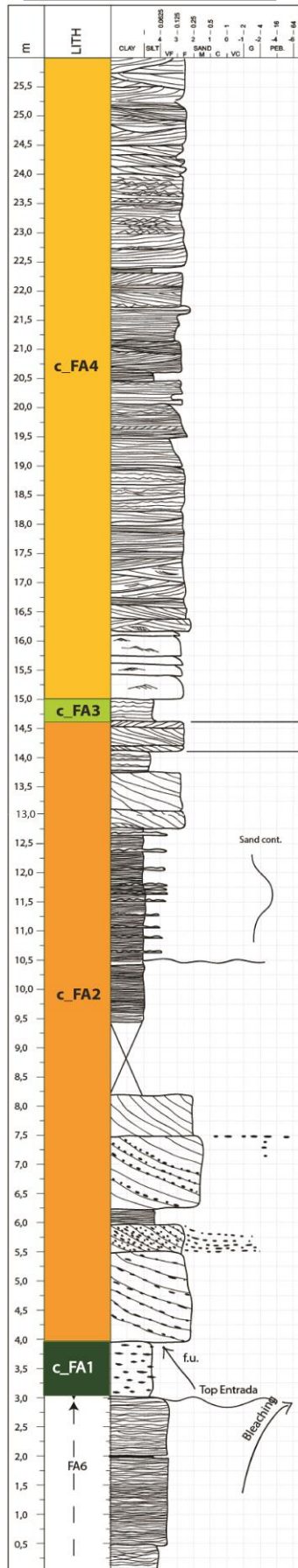
LOG 5
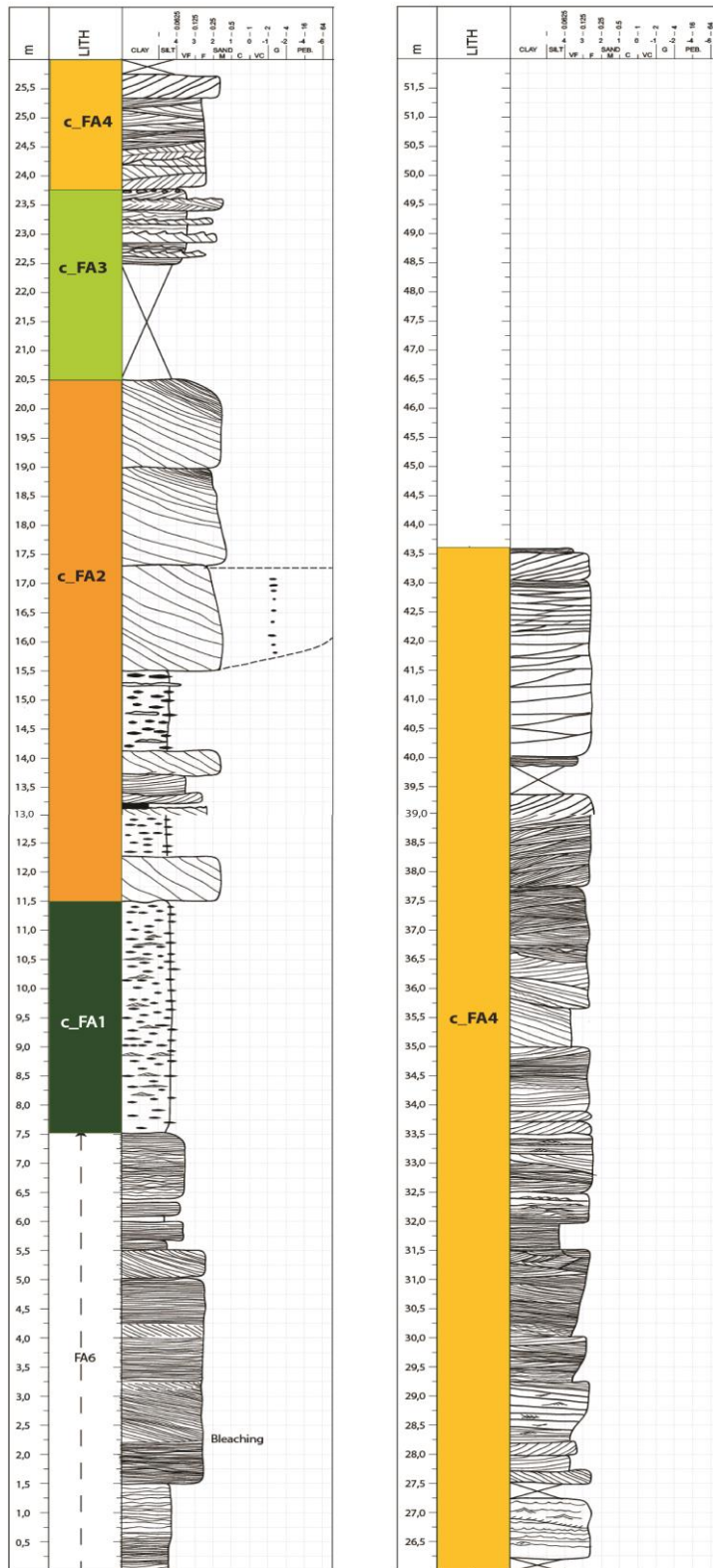
Appendix A

LOG 7
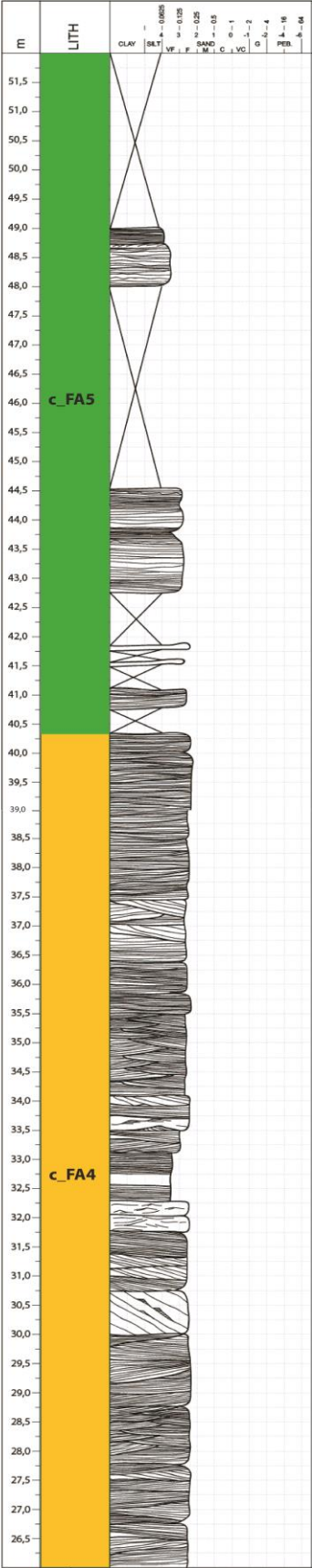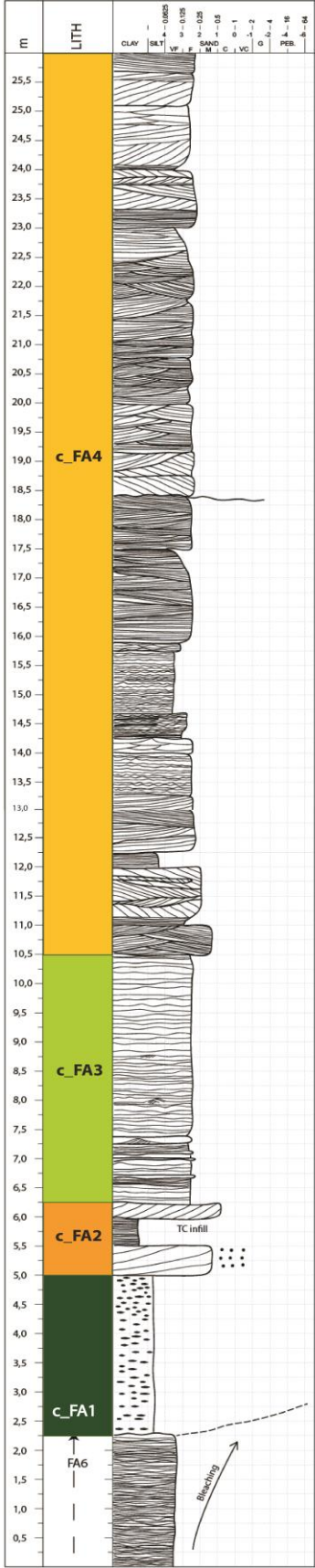
LOG 8
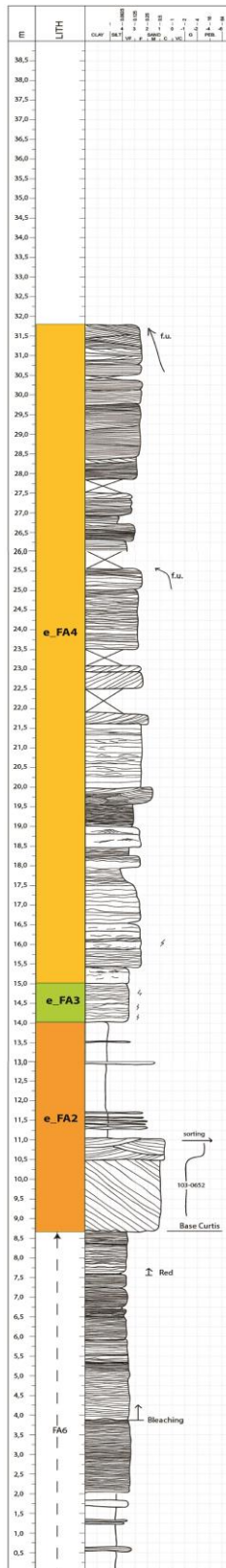
LOG 9
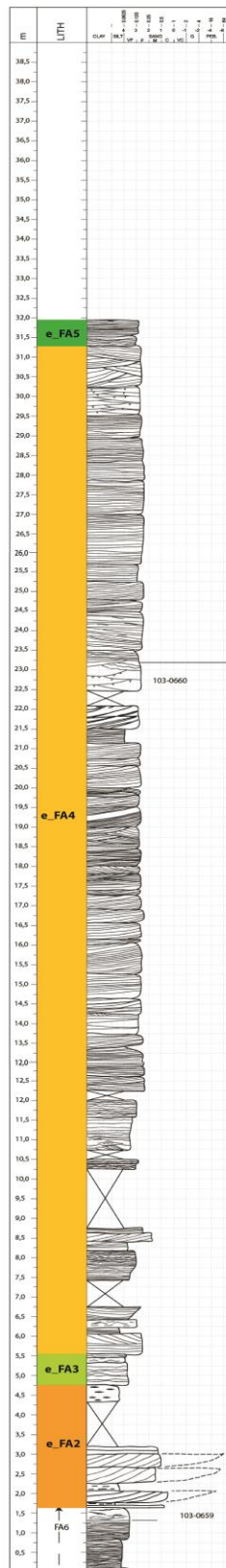
LOG 10
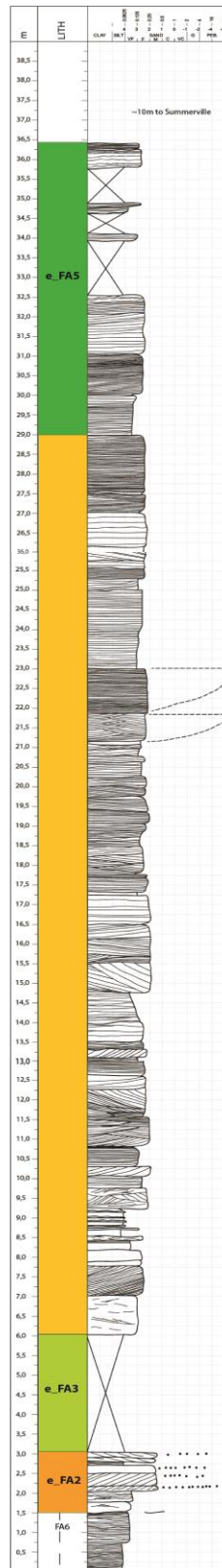
A.4 Entrada log
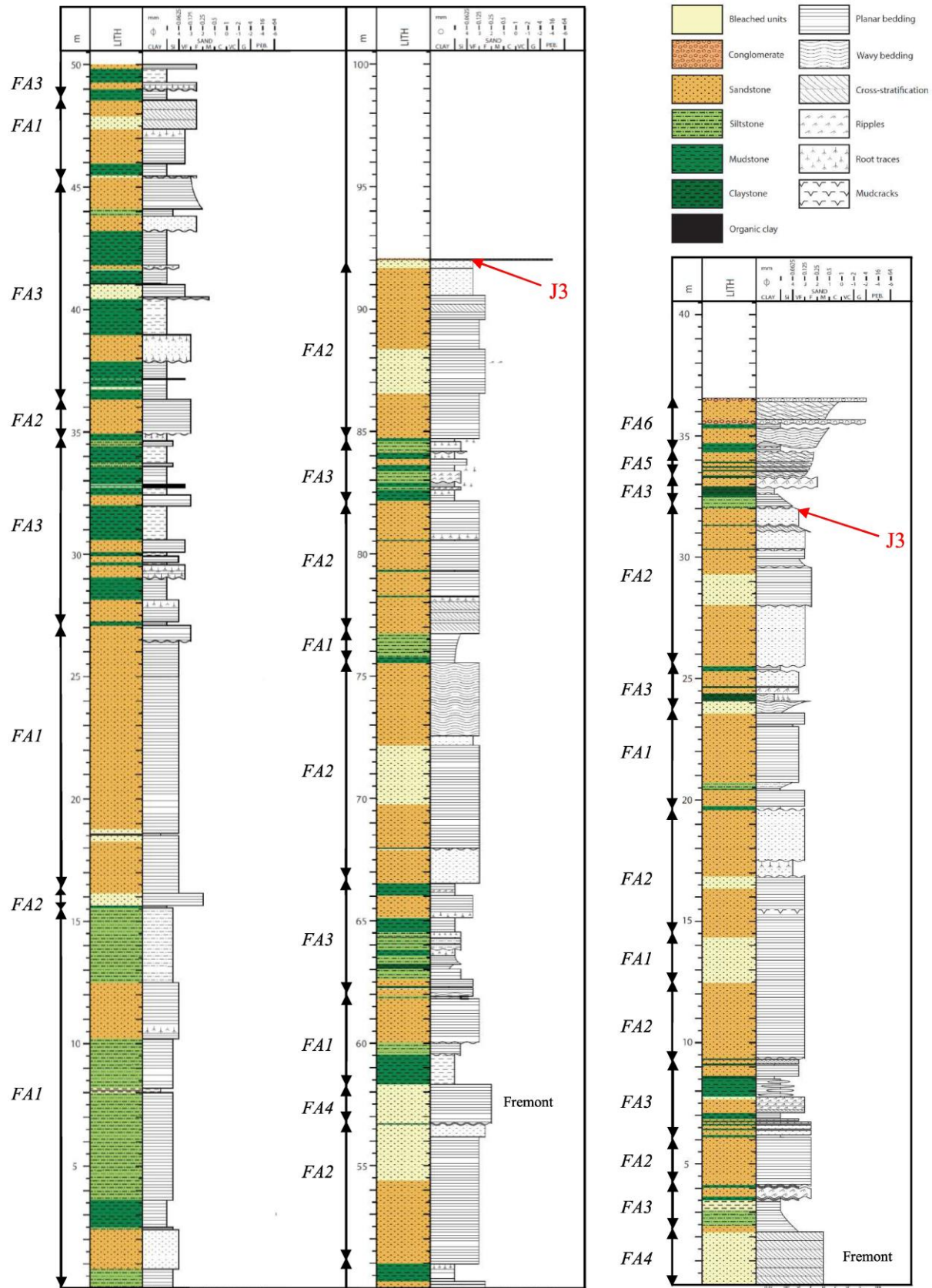
Figure A.4.1: Gurrik (2016) original logs of the hanging wall (right column) and footwall (left column).

Appendix A

A.5 Facies association transition (Well-picks)

Table A.5.1: Well picks used in the horizon model (modified from Gurrik (2016)). Note that the values are represented negative, as they are digitized in RMS.

Well pick:	HW		FW3	
	Altitude (m)	MD	Altitude (m)	MD
Top Entrada	-1600.00	0	-1659.10	0
e_Top_FA3_1	-1593.50	6.25	-1651.85	7.5
e_Top_FA1_1	-1591.50	8.25	-1649.10	10
e_Top_FA2_2	-1587.50	12.25	-1642.60	16.50
e_Top_FA3_3	-1577.50		-1633.60	25
E_Top_FA4	-1570.25	29.50	-1625.35	
e_Top_FA2_3	-1568.00	32	-1623.85	

Appendix A

Table A.5.2: Original well picks from Petrel of the Curtis Formation (Rimkus, 2016). Note that the well picks have a negative altitude as they are represented in RMS with negative values.

Log:	Top_Entrada	FA2_Base	FA2_Base_2	Top_FA2	c_Top_FA3	c_Top_FA5
1	-1584.50	-1587.05	-1593.22	-1592.29	-1601.05	-1652.75
2	-1581.31	-1583.86	-1589.42	-1584.81	-1594.48	-1619.59
3	-1640.17	-1640.50	-1642.55	-1641.69	-1646.54	-1681.40
4	-1554.54	-1555.55	-1566.61	-1559.73	-1572.20	-1605.12
5	-1583.91	-1587.94	-1591.99	-1590.56	-1600.33	-1627.61
6	-1556.55	-1556.55	-1564.69	-1559.48	-1568.63	-1556.55
7	-1564.17	-1567.09	-1574.77	-1568.36	-1581.28	-1618.99
8	-1575.32	-1575.36	-1582.08	-1577.70	-1586.29	-1614.26
9	-1607.63	-1607.66	-1611.51	-1609.10	-1616.30	-1649.55
10	-1625.07	-1625.07	-1629.56	-1626.67	-1632.82	-1667.00

Table A.5.3: Well picks used in the horizon modelling. The well picks are modified from the logs conducted by Rimkus (2016). Note that the values are represented with negative as in RMS

Log:	Top_Entrada	c_Top_FA1	c_Top_FA2	c_Top_FA3	c_Top_FA4
1	-1583.50	-1586.10	-1597.10	-1600.00	-1645.00
2	-1589.00	-1591.50	-1598.75	-1599.75	-
3	-1641.70	-1642.00	-1643.10	-1644.00	-1674.50
4	-1562.70	-1563.00	-1564.00	-1565.00	-1603.00
5	-1582.00	-1586.00	-1595.00	-1598.25	-
6	-1555.83	-1555.83	-1556.15	-1559.25	-
7	-1564.03	-1566.75	-1568.25	-1572.25	-1602.25
8	-1575.79	-1575.79	-1581.00	-1582.00	-
9	-1607.75	-1607.75	-1610.75	-1611.50	-1637.25
10	-1625.00	-1625.00	-1626.70	-1629.50	-1652.50

APPENDIX B - Facies

B.1 Facies association thickness

Entrada sandstone

Table B.1.1: The Tabell display the thickness measurements of the facies associations from the Entrada sandstone. These thickness measurements are found in by using measurement tool in Lime. They are therefore not precise. For best fit there are three measurements from each scan.

Layer:	Min (m)	Max (m)	Mean (m)
e_FA2_1	5.91	8.46	7.38
e_FA3_1	2.54	2.96	2.64
e_FA1_1	3.08	5.62	5.11
e_FA2_2	9	10	9.5
e_FA3_3	5.92	9.64	7.84
e_FA4	1.76	3.34	2.67
e_FA2_3	3.00	2.50	2.75

Curtis Formation

Table B.1.2: The Tabell show the thickness of the facies association within the Curtis Formation. The facies association thickness is found in Rimkus logs as well as by the well-picks.

Layer	Min (m)	Max (m)	Mean (m)
c_FA1	0.00*	4.00	1.69
c_FA2	0.24	11.00	4.10
c_FA3	0.75	4.00	2.01
c_FA4	13	45.00	30.38
c_FA5	7.75	24.5	11.94

The layer is eroded

Appendix B

B.2 Bed statistics of Curtis Formation

Table B.2.1: The distribution of facies and facies associations within the Curtis Formation

Formation Fm.	Facies association:	Depositional environment:	Facies:
Summerville Fm.		Marginal marine	
Curtis Fm.	c_FA5	Upper intertidal	c_A. c_B
	c_FA4b	Beach with tidal inlets	c_C. c_D
	c_FA4a	Sub-intertidal	c_E. c_F
	c_FA3	Subtidal	c_E. c_G
	c_FA2	Tidal transition	c_G. c_ H. c_ E
	c_FA1	Sub-tidal shelf	c_G. c_I
Entrada sandstone		Coastal eolian	

Table B.2.2: Thickness of facies within the facies associations from the Curtis Formation. The data is compiled from the digitized logs.

Facies	Number of beds	Min thickness (m)	Max thickness (m)	Mean bed thickness
Curtis facies association 1 (c_FA1)				
c_G	6	0.0	4.00	2.07 ± 1.30
c_I	1	1.50	1.50	1.50
Curtis facies association 2 (c_FA2)				
c_G	18	0.30	3.02	0.89±.85
c_H	20	0.20	4.31	1.14±1.19
c_E	3	0.95	1.65	1.20± 0.3
Curtis facies association 3 (c_FA3)				
c_E	12	0.38	4.80	1.63±.1.53
c_G	4	0.21	1.19	0.87±0.37
Curtis facies association 4a (c_FA4a)				
c_E	10	0.12	1.43	0.50±.0.35
c_F	15	0.20	3.00	1.00±0.80
Curtis facies association 4b (c_FA4b)				
c_C	64	0.20	10.08	2.42±.2.45
c_D	58	0.21	7.55	1.29±1.22
Curtis facies association 5 (c_FA5)				
c_A and B	11	0.22	4.09	1.23±.1.23

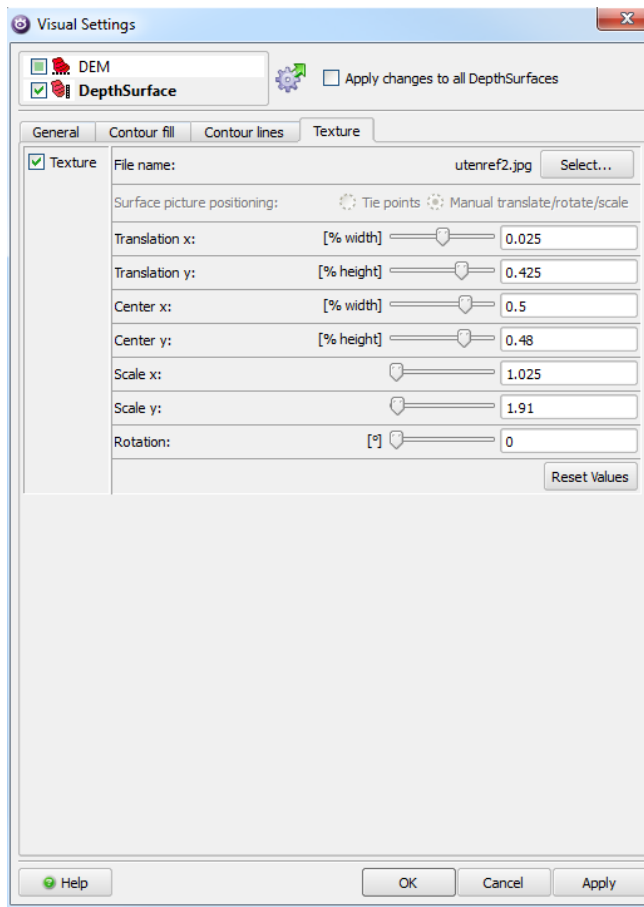# APPENDIX C – Modelling

Figure C.1: Texturing setting of DEM.

APPENDIX D – Petrophysics

Table D.1.1: Corresponding facies definition and facies associations for Larsen (2015), Kristensen (in prep.) and Gurrik (2016).

Layer:	Facies association:
Layer 10	e_FA2_1
Layer 9	e_FA2_1
Layer 8	e_FA1_1
Layer 7	e_FA2_2
Layer 6	e_FA2_2
Layer 5	e_FA2_2, e_FA3_3
Layer 4	e_FA1_2
Layer 3	e_FA4 (Fremont)
Layer 2	e_FA2_3
Layer 1	e_FA2_3

Table D.1.2: Permeability measurements in the Entrada sandstone. using a TinyPerm2

Layer	Layer 2		Layer 3	
	Horizontal:	Vertical:	Horizontal:	Vertical:
Measurements (TinyPerm II value)	12.02	11.84	10.56	10.60
	11.87	12.04	10.31	10.31
			10.05	10.18
			9.80	10.24
Mean	11.95	11.94	10.18	10.28
Permeability (mD)	13.35	13.73	1916.89	1447.89

Appendix D

Table D.1.3: Permeability values for the Entrada sandstone. Porosity and vertical permeability have not been compiled from layer 8-10.

Layer:	Porosity (%)	Permeability Kh (mD)	Permeability Kv (mD)
Layer 1	11.41'	16.72*	
Layer 2	11.74'	38.39*	
Layer 2 (upper)	18.22'	41.24*	18.57*
Layer 3		2498.89*	827.60*
Layer 3 (upper)		1158.87*	38.51*
Layer 4	9.47'	10.77*	19.65*
Layer 5	15.19'	36.35*	4.23*
Layer 6 (lower)	22.35'		5*
Layer 6 (upper)		49.61*	Low*
Layer 7 (bleached)	19.70'	171.95*	110.62*
Layer 7	-	23.72*	Low*
Layer 8	-	-	-
Layer 9	-	75.03*	-
Layer 10	-	545.23*	-

' Collected by Kristensen (in prep.)
*Sundal (pers. Comm.) and Skurtveit (pers. Comm.)

Appendix D

Table D.1.4: Permeability measurements in the Curtis Formation. using a TinyPerm2

Layer	TSF_1 (Facies c_C)		TCD (Facies c_D)	
	Horizontal:	Vertical:	Horizontal:	Vertical:
Measurements (TinyPerm II value)	11.63	11.73	11.25	11.69
	11.54	11.33	11.14	11.17
	11.11	11.34	11.88	12.04
Median	11.54	11.34	11.25	11.69
Permeability (mD)	42.20	73.96	95.21	27.70

Table D.1.5: Porosity and permeability input. The percentage of calcite cement is shown as a result of the low porosity values. Porosity values for facies c_F and c_G have been estimated from other layers. Permeability measurements was collected in field (see table D.1.4) and the remaining permeability values exceeded the 5 minute limit and therefore estimated low values. Permeability and porosity values have been estimated for Tidal mudflat deposits (c_A and c_B).

Facies:	Porosity (%) Petrographic analysis (n)	Calcite cement:	Permeability h (mD)	Permeability h (mD)	Permeability v (mD)
c_A and c_B: TMF	6.50 % (n = 400)	18.00 %	0.01	0.01	0.01
c_C: TSF_1	1.00 % (n = 400)	38.50 %	42.20	42.20	73.96
c_D: TCD	4.00 % (n= 800)	(10.50 %. 14.00 %)	95.21	95.21	27.70
c_E: SSB	0.75 % (n = 400)	21.75 %	0.001	0.001	0.001
c_F: TSF_2	0.50 %	-	0.001	0.01	0.001
c_G: OLE	0.05 %	-	0.001	0.001	0.001
c_H: MTCD	0.25 % (n = 400)	26.50 %	0.001	0.001	0.001
c_I: SER	(no measurements)	-	0.001	0.001	0.001